creative commons

COMMONS DEED

저작자표시-비영리-변경금지 2.0 대한민국

이용자는 아래의 조건을 따르는 경우에 한하여 자유롭게

- 이 저작물을 복제, 배포, 전송, 전시, 공연 및 방송할 수 있습니다.

다음과 같은 조건을 따라야 합니다:

저작자표시. 귀하는 원저작자를 표시하여야 합니다.

비영리. 귀하는 이 저작물을 영리 목적으로 이용할 수 없습니다.

변경금지. 귀하는 이 저작물을 개작, 변형 또는 가공할 수 없습니다.

- 귀하는, 이 저작물의 재이용이나 배포의 경우, 이 저작물에 적용된 이용허락조건을 명확하게 나타내어야 합니다.
- 저작권자로부터 별도의 허가를 받으면 이러한 조건들은 적용되지 않습니다.

저작권법에 따른 이용자의 권리는 위의 내용에 의하여 영향을 받지 않습니다.

이것은 이용허락규약(Legal Code)을 이해하기 쉽게 요약한 것입니다.

Disclaimer

dCollection

Ph.D. DISSERTATION

Spatial-type and Plasma Enhanced-type Atomic Layer Deposition of Al_2O_3 and Si_3N_4 Thin Films

by

Sungin Suh

August 2014

Department of Materials Science and Engineering
College of Engineering
Seoul National University

Spatial-type and Plasma Enhanced-type Atomic Layer Deposition of Al_2O_3 and Si_3N_4 Thin Films

Advisor : Prof. Hyeong Joon Kim

By
Sungin Suh

A thesis submitted to the Graduate Faculty of Seoul National University in partial fulfillment of the requirements for the Degree of Doctor of Philosophy

Department of Materials Science and Engineering

August 2014

Approved
by

Chairman of Advisory Committee :Cheol Seong Hwang

Vice-chairman of Advisory Committee :Hyeong Joon Kim

Advisory Committee :Young-Chang Joo

Advisory Committee :Seok-Jun Won

Advisory Committee :Jaeyeong Heo

ABSTRACT

Recently, three-dimensional (3D) structure has been highlighted for the next–generation device. In order to implement the 3D structure, the channel layer should be changed to the films that can be easily deposited such as amorphous oxide semiconductor (AOS), which has the wide and gap of 3.0eV and the relatively high mobility of ~ 10 $cm^2/V{\cdot}s$. However, the AOS such as Zinc Tin Oxide (ZTO) can be crystallized above 450℃ and form different crystalline phases from 450℃ to 800℃. Therefore, the gate dielectric layer or the trap layer should be processed under 400℃ in order to apply to the AOS channel layer.

In this dissertation, modified plasma enhanced ALD (PEALD) processes for deposition of silicon nitride films at such low temperature, which activated silicon precursor by RF plasma, were presented. It was hard to deposit silicon nitride films at low temperature by conventional PEALD method due to high activation energy for adsorption of the silicon precursor on Si-N networks. By adopting new processes (SPNP, SNP and SPxNP), silicon nitride films were successfully deposited. While films deposited by SPxNP process had high oxygen contents films by SNP and SPNP processes showed that the impurities such as carbon and oxygen were as low as 10 atomic % and silicon-rich films were formed. Silicon nitride films by SPNP showed the charge trap layer properties with a hysteresis window of 3.1 V and 97% of the step coverage. This indicates that SPNP process can be one of solutions for the low temperature silicon nitride deposition.

In addition, Al_2O_3 thin films were deposited using tri-methyl aluminum and ozone by spatial atomic layer deposition (SALD) with a large gap between the reactor and substrates. According to deposition

results and simulation data, strong edge pumping for the dominantly lateral flow improved the gas isolation and deposition was very effective, with a resulting gap height of 5 mm. To compare this SALD process with conventional atomic layer deposition (ALD), it was examined how the amount of source supplied, the deposition temperature, and the number of rotations affected the growth rate. The growth rate per rotation was saturated at ~0.12 nm/rotation at a deposition temperature of 250 ^{o}C, which is comparable to the saturated growth rate of the same film using conventional ALD. The dielectric constant of the films deposited by fast SALD process was ~8 and the film with a capacitance equivalent thickness of 3.2nm had a leakage level of 9.8×10^{-8} A/cm^2 (at -1V). X-ray photoelectron spectroscopy peak analysis indicates that the films deposited by SALD consist of Al_2O_3. This indicates that SALD is a viable option for several mass-production applications that require high throughput.

Keywords: PEALD, silicon nitride, modified PEALD using source plasma, Spatial ALD, aluminum oxide, ozone
Student Number: 2008-22850
Sungin Suh

CONTENTS

Abstract i

Contents iii

List of Tables vi

List of Figures vii

1 Introduction 1

1.1 Overview 1

1.2 Background of Atomic Layer Deposition 5

1.2.1 General Principle of Atomic Layer Deposition 5

1.2.3 Adsorption and Desorption in ALD 7

1.2.4 ALD Process Window 20

1.2.5 Reactive Site Density in ALD 22

1.2.6 Effect of Temperature on the Growth Rate in ALD 24

1.2.7 Steric Hindrance 27

2 Literature Review 30

2.1 Plasma Enhanced Atomic Layer deposition 30

2.1.1 Basic Concept of PEALD 30

2.1.2 Merit of PEALD 32

2.1.3 Modeling of PEALD 35

2.2 Atomic Layer Deposition of Silicon Nitride 38

2.3 Spatial Atomic Layer Deposition 40

2.3.1 General Concept of Spatial Atomic Layer Deposition 40

2.3.2 Characteristics of Spatial ALD 42

2.3.3 Trends of Spatial ALD 46

2.4 Atomic Layer Deposition of Al_2O_3 with Tri-methyl-aluminum..... 52

2.5 Simulation with CFD-ACE+ 58

3 Experiments and Analyses 62

3.1 Modified PEALD of Silicon Nitride..... 62

3.1.1 Modified PEALD of Silicon Nitride.....62

3.2 Sptial-type Atomic Layer Deposition of Al_2O_3 66

3.2.1 Sptial-type Atomic Layer Deposition of Al_2O_3.....66

3.2.2 Gas Flow Simulation with CFD-ACE+ 72

3.2.3 Analyses of the Deposited Films 74

4 Results and Discussions 75

4.1 Plasma Enhanced Atomic Layer Deposition of Silicon Nitride films..... 75

4.1.1 Introduction 75

4.1.2 Conventional PEALD of Silicon Nitride Films.....78

4.1.3 Modified PEALD Processes with Silicon Source Plasma...80

4.1.4 Deposition Properties of Modified PEALD Processes 84

4.1.5 Electrical and Chemical Analysis of Silicon Nitride Films with Different Deposition Processes.....94

4.1.6 Charge Trap Layer Properties of SNP and SPNP Silicon Nitride Films 103

4.1.7 Step Coverage of the Silicon Nitride Film Deposited by SPNP Process 106

4.1.8 Summary 108

4.2 Spatial-Type Atomic Layer Deposition of Al_2O_3 109

4.2.1 Introduction 109

4.2.2 Deposition Behavior of Spatial Atomic Layer Deposition 112

4.2.3 Gas Flow Simulation of Spatial Atomic Layer Deposition 116

4.2.4 Deposition Properties of Al_2O_3 Deposited by SALD 121

4.2.5 Electrical Properties of SALD Al_2O_3 124

4.2.6 XPS Analysis of SALD Al_2O_3 127

4.2.7 Summary 129

5 Conclusions 130

6 Reference 133

List of publications 140

Abstract (in Korean) 146

LIST OF TABLES

Table 2.1 Physical and Chemical Properties of tri-methy-aluminum precursor. 55

Table 2.2 Aluminum part from Overview of ALD processes based on two reactants[9] 56

Table 3.1 Physical and Chemical Properties of tri-methy-aluminum precursor. 70

Table 3.2 Process conditions of SALD of Al_2O_3 71

Table 4.1 The deposition properties of the optimized processes 93

Table 4.2 XPS silicon 2p peaks decomposition. 102

LIST OF FIGURES

Figure 1.1 The number of scientific publications on ALD published per year during 1980 to 2010.[5] 4

Figure 1.2 Schematic illustration of one ALD reaction cycle..... 6

Figure 1.3 Graphical illustration of Eq. 1.8. 12

Figure 1.4 Effect of the reactant partial pressure p on the amount of material chemisorbed in a gas–solid reaction: (a) the equilibrium chemisorption coverage Q_{eq} in reversible adsorption and (b) the chemisorption coverage Q after saturation in irreversible adsorption.[9] 17

Figure 1.5 Time variation of adsorption amount: (a) irreversible self-limited adsorption (chemisorptions) (b) reversible adsorption and (c) irreversible and reversible adsorption.[9] 18

Figure 1.6 Schematic representation of five reaction cycles, assuming irreversible adsorption: (a) chemisorption coverage Q as a function of time t, (b) the amount of atoms adsorbed as a function of time t, and (c) the deposition rate of atoms as a function of time t.[9] 19

Figure 1.7 ALD temperature window 21

Figure 1.8 Factors identified to cause saturation of irreversible chemisorption: (a) steric hindrance of the ligands and (b) number of reactive surface sites. 23

Figure 1.9 Variation of the GPC with the ALD processing temperature in the

ALD window. 26

Figure 1.10 Schematic illustration for analyzing sterically hindered chemisorption on the basis of the size of the ML_n reactant.[9]..... 29

Figure 2.1 Schematic representation of thermal ALD and plasma-assisted ALD.[18] 31

Figure 2.2 General growth characteristics of ALD as a function of growth temperature.[19] 34

Figure 2.3 Ion energy distribution remote plasma-assisted ALD measured by a retarding field energy analyzer (operating pressure: 8 mTorr; plasma power: 100 W)[18] 37

Figure 2.4 Schematic representation of the ALD process(a) Conventional ALD (b) Spatial ALD[33] 41

Figure 2.5 Principle of a close proximity spatial ALD reactor concept[33]..... 45

Figure 2.6 Schematic design of several spatial ALD systems.[38-40] 50

Figure 2.7 Schematic design of spatial ALD systems using gas baring. 51

Figure 2.8 Deposition Properties of TMA ALD process. 57

Figure 3.1 Schematic diagram of the PEALD system. 64

Figure 3.2 Schematic drawing of a direct plasma reactor..... 64

Figure 3.3 Structures and properties of silicon precursors. 65

Figure 3.4 Schematic representation of the space-divided ALD. (a) Schematic drawing of the space-divided ALD sequence. (b) Schematic drawing of top view and side view of the SALD reactor. (c) Schematic drawing of the sample location. (d) Schematic drawing of the gas distribution part..... 69

Figure 3.5 Simulation grid of SALD Chamber (a) The gird of the entire SDALD chamber. (b) The grid of a gap between a rotational gas distributor and lower plate..... 73

Figure 4.1 Conventional PEALD process of silicon nitride. (a) Process sequence of conventional PEALD (b) Growth rate of silicon nitride films deposited by conventional PEALD process with various silicon sources. 79

Figure 4.2 Simulation of activation energy in ALD SiN process (sing SiH_4 and NH_3).[31] 82

Figure 4.3 Low temperature NH_3 reaction test 82

Figure 4.4 Process sequence of modified PEALD silicon nitride (a) SPNP process (b) SPxNP process (c) SNP process 83

Figure 4.5 Dominant factor for nitridation (a) GPC vs. NH_3 Plasma Power (b) GPC vs. NH3 flow rate 85

Figure 4.6 Deposition properties of SPNP process (a) GPC vs. source purge time (b) GPC vs. source pulse time (c) GPC vs. source plasma time 86

Figure 4.7 Possible Reaction Sequence of SPNP Process..... 89

Figure 4.8 Deposition propterties of SPxNP process (a) GPC vs. silicon plasma step number (b) GPT vs. silicon plasma step number. ... 90

Figure 4.9 Deposition Behavior of SNP Process 91

Figure 4.10 The deposition properties of the optimized processes..... 93

Figure 4.11 The electrical properties of silicon nitride films deposited by three different processes. (a) C-V curves of the films with different

deposition processes. (b) CET variation of silicon nitride films as a function of their physical thickness. (c)-(e) The leakage property of the films with SNP, SPNP and SPxNP process, respectively. 95

Figure 4.12 FT-IR result of silicon nitride films of SNP, SPNP and SP3NP processes. 98

Figure 4.13 AES analysis result of silicon nitride films of (a) SNP, (b) SPNP and (c) SP3NP processes 99

Figure 4.14 XPS data of the SiN films deposited by SNP, SPNP and SP3NP: (a) silicon 2p peak, (b) nitrogen 1s peak, (c) oxygen 1s peak, (d) carbon 1s peak. 102

Figure 4.15 Schematic diagram ofthe Pt//PEALD-Al_2O_3 /SiN_x by modified process/PEALD-SiO_2/Si multilayer structure 105

Figure 4.16 C−V hysteresis after bidirectional voltage sweeping for devices of (a) only Al_2O_3, (b) oxide-nitride-oxide with SNP silicon nitride film and (c) oxide-nitride-oxide with SPNP silicon nitride film. (d) C−V hysteresis window for devices with different process. 105

Figure 4.17 SEM image of etched SPNP silicon nitride films on thermal SiO_2 pattern. (a) top (b) side at 1.25 μm and (c) bottom. 107

Figure 4.18 Effect of the gap size on gas mixing. (a) Change in GPR as a function of the rotation speed with a gap size of 10 mm. (b) Change in GPR as a function of the rotation speed with a gap size of 5 mm. 114

Figure 4.19 Effect of the lateral flow on gas mixing.Change in GPR as a

function of the throttle valve opening ratio. 115

Figure 4.20 Effect of the gap size on gas mixing.Changes in mole fractions of TMA gas and O_2 as a function of distance from the center of lower plate with gap sizes of (a)10mm and (b) 5mm..... 119

Figure 4.21 Effect of the lateral flow on gas mixing. (a) Simulated distribution of TMA mole fraction with weak edge pumping. (b) Simulated distribution of TMA mole fraction with strong edge pumping. 120

Figure 4.22 Deposition properties of Al_2O_3 deposited by SALD. (a) Change in GPR as a function of the TMA valve opening ratio. (b) Change in the GPR as a function of deposition temperature. (c) Change in the thickness of deposited thin films as a function of cycle number. Data were obtained from sample positioned at M..... 123

Figure 4.23 (a) Variation in the CET of the SALD Al_2O_3 films with their physical thickness. (b) Leakage current data of SALD Al_2O_3 films of 40, 80, 120, and 160 rotations measured by the Current density-voltage method. Data were obtained from sample positioned at M. 126

Figure 4.24 XPS spectra for (a) Al 2p and (b) O 1s in the Al_2O_3 film grown by SALD at 160 cycles. 128

1 INTRODUCTION

1.1 Overview

2010 ITRS (International Technology Roadmap for Semiconductors) showed that three-dimensional (3D) structure has been highlighted for the next–generation device. In order to implement the 3D structure, the channel layer should be changed to the films that can be easily deposited such as amorphous oxide semiconductor (AOS), which has the wide and gap of 3.0eV and the relatively high mobility of ~ 10 $cm^2/V{\cdot}s$.[1] However, the AOS such as Zinc Tin Oxide(ZTO) can be crystallized above 450℃ and form different crystalline phases from 450℃ to 800℃.[2] Therefore, the gate dielectric layer or the trap layer should be processed under 400℃in order to apply to the AOS channel layer.

Atomic layer deposition (ALD) has been highlighted as a promising thin film deposition technique for semiconductor devices because of its very excellent step coverage, precise controllability of the film thickness and relatively low process temperature than chemical vapor deposition (CVD) as shown in Figure 1.1.[3-5] Atomic layer deposition (ALD) is a thin film growth technique based on the sequential exposure of a substrate to self-limiting surface half-reactions.[6,7] The

one cycle of ALD is composed of source pulse, source purge, reactant pulse, and reactant purge. In the step of providing precursors to the substrate, the precursors are initially adsorbed chemically on the surface and the remaining precursors are adsorbed physically on the already deposited precursor molecules. Physically adsorbed precursors are desorbed during a purge step, which follows after the providing precursors step, resulting in the growth of one (or sub-one) atomic layer in a subsequent reactant pulse step. This results in a self-limited growth behavior of thin films, where the growth rate is determined solely by the number of reaction sites on the initial surface, regardless of the precursor and reactant doses. ALD also has the advantages of forming superior films in quality at relatively low temperatures compared to chemical vapor deposition.

However, conventional ALD systems have several limitations, such as a low growth rate, difficulty in selecting appropriate sources, and high cost of ownership due to the short lifetime of the switching valves and their complicated gas line configuration. These factors make their widespread use unrealistic. Also, ALD of some materials, such as silicon nitride, have still higher process temperature than requirement of the state-of-art semiconductor device such as three-dimensional NAND flash memory.

In this dissertation, the modified plasma-enhanced ALD (PEALD) will be introduced for the growth of silicon nitride films at low

temperature. Also, this dissertation will discuss the deposition of Al_2O_3 by the new type of ALD, which is spatial atomic layer deposition that can reduce thermal budget than conventional ALD due to its high process speed.

The outline of this dissertation is as follows. Chapter 1 reviews the basic concepts of ALD. Chapter 2 reviews the representative literatures showing plasma enhanced ALD of silicon nitride and spatial ALD. Chapter 3 displays experimental and analytical methods. In Chapter 4, feasibility of spatial ALD with large gap will be discussed along with newly introduced modified PEALD. Chapter 5 provides the conclusion of the thesis.

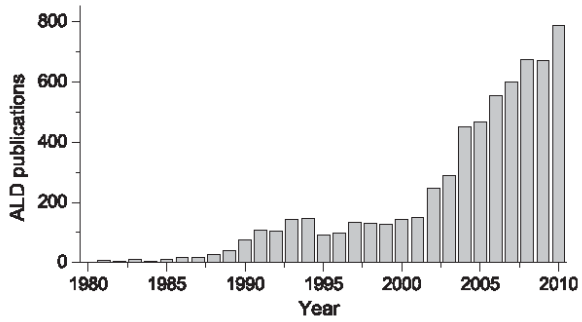

Figure 1.1 The number of scientific publications on ALD published per year during 1980 to 2010.[5]

1.2 Background of Atomic Layer Deposition

1.2.1 General Principle of Atomic Layer Deposition

Atomic layer deposition (ALD) is a thin film growth technique based on the sequential exposure of a substrate to self-limiting surface half-reactions.[6,7] In detail, it is a deposition method which is able to control a layer thickness on an atomic scale by alternating injections of sources and reactants. In the step of providing precursors to the substrate, the precursors are initially adsorbed chemically on the surface and the remaining precursors are adsorbed physically on the already deposited precursor molecules. Physically adsorbed precursors are desorbed during a purge step, which follows after the providing precursors step, resulting in the growth of one (or sub-one) atomic layer in a subsequent reactant pulse step. This results in a self-limited growth behavior of thin films, where the growth rate is determined solely by the number of reaction sites on the initial surface, regardless of the precursor and reactant doses. [8]The one cycle of ALD is composed of source pulse, source purge, reactant pulse, and reactant purge as shown in Figure 1.2.[9]

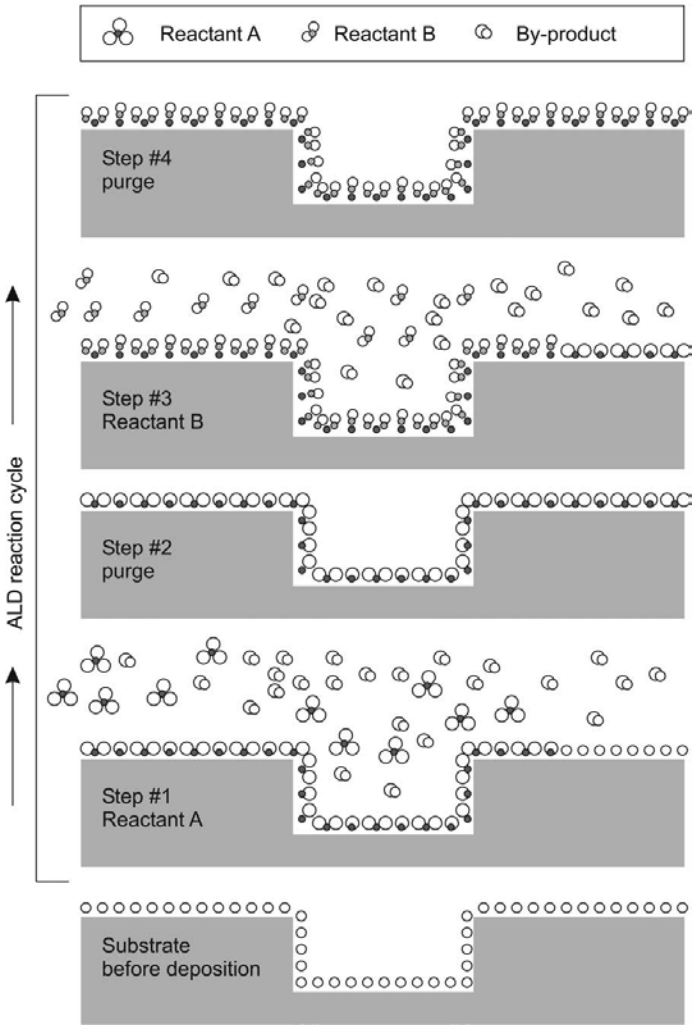

Figure 1.2 Schematic illustration of one ALD reaction cycle.

1.2.3 Adsorption and Desorption in ALD

Adsorption is the phenomenon which gas atoms or molecules are attached on a solid surface, which plays a very important role in ALD. The adsorption of gas atoms or molecules occurs because a solid surface has a high energy. According to the thermodynamic equation, $\Delta S < 0$ in $\Delta G = \Delta H - T\Delta S$[10], ΔH must be a higher negative value so that the adsorption reaction occurs spontaneously. In other words, adsorption is normally an exothermic reaction. Also, in order that adsorption takes place in, it is important that there should be enough energy to overcome the activation energy barrier for adsorptive reaction. Therefore, there is two cases that gas atoms or molecules are not adsorbed on the surface; a very high activation energy, called "a kinetic barrier", to be adsorbed due to the dissociative adsorption, for example H_2 on Cu, and a stable surface in terms of energy, such as MgO.

The fundamental concept in ALD is that precursors are initially adsorbed chemically on the surface and the additional precursors are adsorbed physically on the already deposited precursor molecules in a proper ALD condition. Physically adsorbed precursors are desorbed during the subsequent purge step resulting in the growth of an atomic monolayer in the subsequent reactant pulse step. Therefore, the concept of a physisorption and chemisorption is important need to be

understood. Physisorption means that precursors are adsorbed on the surface by van der Waals interaction and is similar to condensation. Heat of adsorption, ΔH_{ad}, is $\leq$ 200 kJ/mol, typically 20 kJ/mol, and nonspecific for adsorbents. There is no charge transfer between adsorbent and adsorbate.[11] Chemisorption originates from chemical interactions and is similar to the bond formation. ΔH_{ad} is $\geq$ 200 kJ/mol (~2 eV). Chemisorption is specific for adsorbents. There is charge transfer between adsorbent and adsorbate.[12] Heat of adsorption can be obtained by a reversible adsorption isotherm using the Clausius-Clapeyron equation (Eq. 1.1).

$$\left(\frac{\partial \ln P}{\partial T}\right)_V = -\frac{\Delta H_{ad}}{RT^2} \quad \text{----- Eq. 1.1}$$

The reaction of from two reactants of AX_x and BY_y to compound AB can be represented as follows.[12]

$$AX_x(g) + BY_y(g) \rightarrow AB(s) + XY(g) + xy(g) \quad \text{----- Eq. 1.2}$$

The reaction can be divided into two half reactions (Eq. 1.3 and 1.4) in ALD.

$$BY_y(g) + X^*(AB)_m(s) \rightarrow y^*B(AB)_m(s) + XY(g) \quad \text{----- Eq. 1.3}$$

$$AX_x(g) + y^*B(AB)_m(s) \rightarrow X^*(AB)_{m+1}(s) + xy(g) \quad \text{----- Eq. 1.4}$$

Asterisk indicates the surface-adsorbed chemical group or atom.

In ALD, adsorption kinetics complies with Langmuir model because of the layer-by-layer growth with source and reactant separated by purge gas. Langmuir model is that there is no more adsorption on the already-adsorbed adatom and a next layer is formed after a full coverage of a current layer. A model equation expressed by fractional coverage, θ, showing the formation of each layer is as follows.[12]

$$\frac{d\bar{\theta}^{AB}}{dt_A} = r_{ad}^{AB} - r_d^{AB} = k_{ad}^{AB} P_A (1 - \bar{\theta}^{AB}) - k_d^{AB} \bar{\theta}^{AB} \text{ ----- Eq. 1.5}$$

In the Eq. 1.5, "1-$\bar{\theta}^{AB}$" indicates that there is no adsorption on the already-adsorbed sites. $\bar{\theta}^{AB}$ following k_d^{AB} means that something adsorbed can be desorbed. Here, r_{ad}^{AB} and r_d^{AB} are the adsorption and desorption rates and $\bar{\theta}^{AB}$ is the coverage of adsorbate X^*A on the atomic B layer. t_A is the exposure time of AX_x, P_A is the partial pressure of AX_x, k_{ad}^{AB} and k_d^{AB} are the adsorption and desorption coefficients, respectively. Superscript AB denotes the case when AX_x adsorbs onto atomic B layer. In the opposite case, i.e., when BY_y adsorbs onto atomic A layer, superscript is BA. The solution of the Eq.

1.5 is given by

$$\bar{\theta}^{AB} = \bar{\theta}_{st}^{AB}[1-\exp(-(k_{ad}^{AB}P_A + k_d^{AB})t_A)] \quad \text{----- Eq. 1.6}$$

$$\bar{\theta}_{st}^{AB} = k_{ad}^{AB}P_A/(k_{ad}^{AB}P_A + k_d^{AB}) \quad \text{----- Eq. 1.7}$$

On the other hand, θ_{BA} should be considered in an actual growth rate of thin films. This can be obtained through a little complicate calculation.[12] The growth rate (GR) considering θ_{BA} is as follows

$$GR = \frac{\theta^{AB} \cdot \theta^{BA}}{1-(1-\theta^{BA})\cdot(1-\theta^{AB})} \quad \text{----- Eq. 1.8}$$

This equation is graphically expressed in a three-dimensional graph (Figure 1.3) where θ^{AB} and θ^{BA} are x- and y-axis, and GR is z-axis. This indicates that GR is solely determined by surface coverage at each pulse.

Adsorption is also classified by activated adsorption and non-activated adsorption according to whether activation energy exists or not. Activation energy is determined by a combined shape of a chemisorption energy curve and a physisorption energy curve. The adsorption of H_2 on a transition metal is “non-activated adsorption”. The adsorption of H_2 on noble metals is “activated adsorption”.

Precursor chemistry plays a very important role in ALD. Precursors should have a high vapor pressure and thermal stability at the same time. ALD conditions should be carefully designed to avoid the degradation of precursors. The vapor pressure of a precursor should be high to cover the surface completely within the determined time, which is normally required to be more than 0.1 torr. The precursor should not be dissociated by itself in the gas status, which results in the self-limiting behavior, excellent film uniformity, and low impurity concentration. “Langmuir (L)”, 1L = 1 x 10^{-6} torr·sec, is normally used as the degree of exposure.

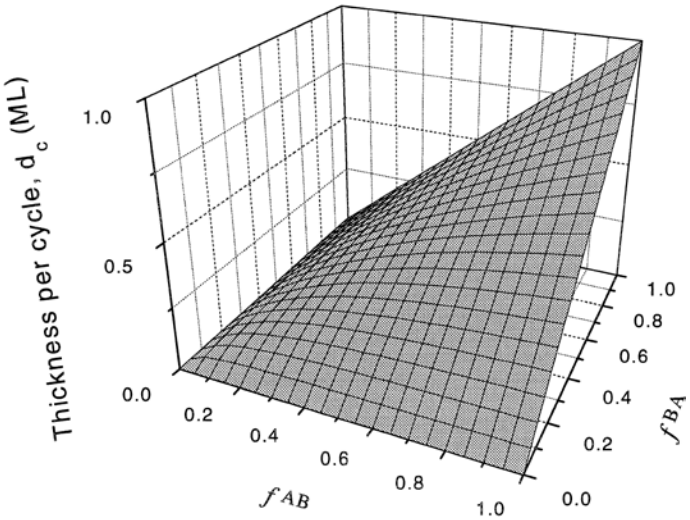

Figure 1.3 Graphical illustration of Eq. 1.8.

Similar work of obtaining the chemisorption coverage from the Langmuir isotherm was done by Puurunen.[9] For illustrating the effect of pressure, three assumptions are made that are often used in the ALD literature; the maximum amount of adsorbed species is assumed to be a monolayer (as in chemisorption), all adsorption sites on the surface are assumed equal, and neighboring adsorbed species are assumed not to interact with each other. A simple example of molecular adsorption of a gaseous compound A on a surface site S illustrates the characteristics of adsorption kinetics in ALD. In the general case, the adsorption can be considered reversible, as illustrated in reactions Eq. 1.9.

$$\mathrm{A(g)} + \mathrm{S(surface)} \rightleftarrows \mathrm{AS\ (Surface)} \quad \text{---- Eq. 1.9.}$$

Here, the coverage of adsorbed species is referred here to as chemisorption coverage and denoted as Q. The adsorption rate equals the adsorption rate constant k_a times the partial pressure p of the molecule A times the fraction (1−Q) of unoccupied surface sites, and the desorption rate equals the desorption rate constant k_d times the fraction Q of occupied surface sites. The rate of change of the chemisorption coverage, dQ/dt, is obtained by subtracting the desorption rate from the adsorption rate,

$$\frac{dQ}{dt} = k_a P(1 - Q) - k_d Q \text{---- Eq. 1.10}$$

In the equilibrium state, the chemisorption coverage is constant (Eq. 1.10 =0), and the equilibrium chemisorption coverage Q^{eq} can be obtained as a function of reactant partial pressure,

$$Q^{eq} = \frac{1}{1+(KP)^{-1}}\ ,\ K = \frac{k_a}{k_d} \text{---- Eq. 1.11}$$

where P, K, k_a and k_d denote pressure ,the equilibrium constant of the adsorption, adsorption rate and desorption rate. In the general case of reversible adsorption (ka≠0≠kd), Q_{eq1} increases with p, as illustrated in Figure 1.4(a). To achieve ALD conditions with self-terminating reactions, however, the adsorption must be irreversible. Equations 1.9 and 1.10 describe practically irreversible reactions if the equilibrium constant K is allowed to approach infinity (or k_d to approach zero). Solving Eq. 1.10 with this assumption, following equation can be considered;

$$\lim_{K\to\infty} Q^{eq} = 1 \text{ ---- Eq. 1.12}$$

In irreversible chemisorption, the chemisorption coverage Q does not increase with p, but settles to unity even at negligibly low reactant

partial pressures p (Figure 1.4 (b)).

Solving by integrating from Eq. 1.10, assuming constant pressure and temperature, the chemisorption coverage Q is obtained as a function of time t,

$$Q = Q^{eq}\left(1 - e^{-(k_a p + k_d)t}\right). \text{ ---- Eq. 1.13}$$

On the other hands, with the assumption that the physisorption is a reversible reaction, saturated physisorbed species reduces as time goes. Therefore, ALD reaction in which both chemisorption and physisorption coexist shows typical self-limiting mechanism as shown in Figure 1.5.

During the reaction of Reactant A, typically a compound reactant, the chemisorption coverage increases until it settles to one when the reaction has terminated. (The higher the p and k_a, the faster the reaction is completed.) During the following purge/evacuation, the chemisorption coverage remains constant. The reaction of Reactant B causes the chemisorption coverage of the species adsorbed from Reactant A to decrease, ideally down to zero. Reactant B brings other types of adsorbed species on the surface, the coverage of which increases from zero to one during the reaction. During the following purge/evacuation, the chemisorption coverages remain constant. During repeating reaction cycles, the chemisorption coverages

therefore switch between zero and one as shown in Figure 1.6(a). Time affects the chemisorption coverage Q in a different way than it affects the total amount of material deposited. As illustrated in Figure 1.6(b), the amount of atoms deposited increases during the first step of the reaction cycles and the deposition rate varies with time (Figure 1.6(c)).

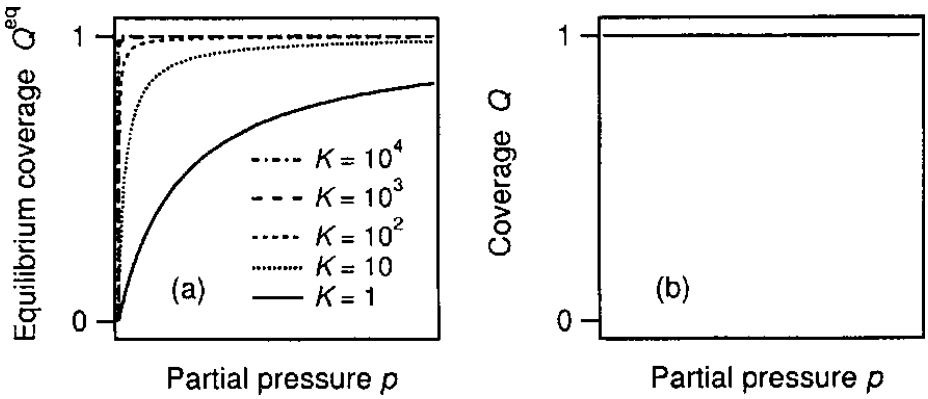

Figure 1.4 Effect of the reactant partial pressure p on the amount of material chemisorbed in a gas–solid reaction: (a) the equilibrium chemisorption coverage Q_{eq} in reversible adsorption and (b) the chemisorption coverage Q after saturation in irreversible adsorption.[9]

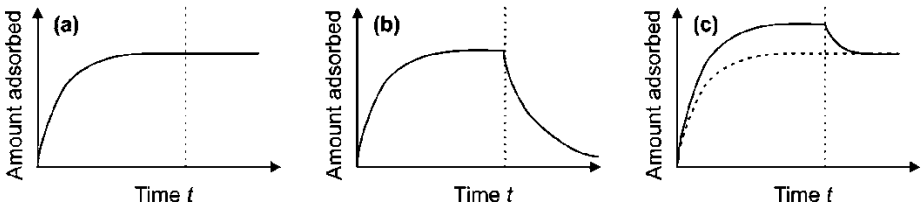

Figure 1.5 Time variation of adsorption amount: (a) irreversible self-limited adsorption (chemisorptions) (b) reversible adsorption and (c) irreversible and reversible adsorption.[9]

\

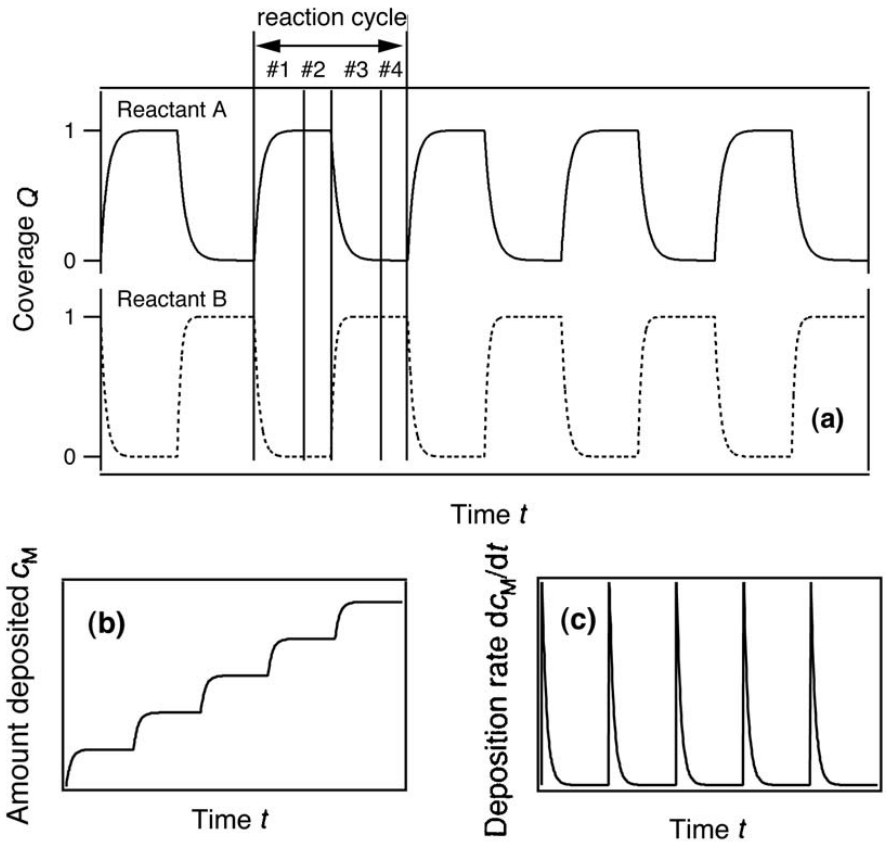

Figure 1.6 Schematic representation of five reaction cycles, assuming irreversible adsorption: (a) chemisorption coverage Q as a function of time t, (b) the amount of atoms adsorbed as a function of time t, and (c) the deposition rate of atoms as a function of time t.[9]

1.2.4 ALD Process Window

It is a very distinguishing feature that there is a temperature window at which ALD can be possible. Figure 1.7 shows how growth rates are varied by growth temperatures in a typical ALD. In Figure 1.7, it is "ALD window" where there is little (or no) variation in deposition rate. In the lower temperature range out of the ALD window, the increase in growth rate originates from the condensation of reactants and the decrease in the growth rate comes from low reactivity of reactants in the temperature range due to high activation energy barrier. The same pattern can be observed in the higher temperature range out of the ALD window. The multilayer formation due to the dissociation of precursors results in the increase in growth rate, which is called "CVD effect". The higher desorption probability and fewer reactive site density in higher temperatures brings the decrease in growth rate. The fewer reactive site density at higher growth temperatures can occur when OH sites react with each other and form "bridged oxygen" with the byproduct, H_2O, which will be gone away to the vapor. The definitive method for verifying whether the process is in an ALD window or not is to observe that thickness is not varied with exposure times of the precursor in a temperature range with an almost constant growth rate. In the case that the growth rate is not perfectly constant in the ALD window, it is probably because of the reconstruction of atoms on the surface, the variation of reactive site density, and the variation of the L/M ratio in the adsorbed ML species.

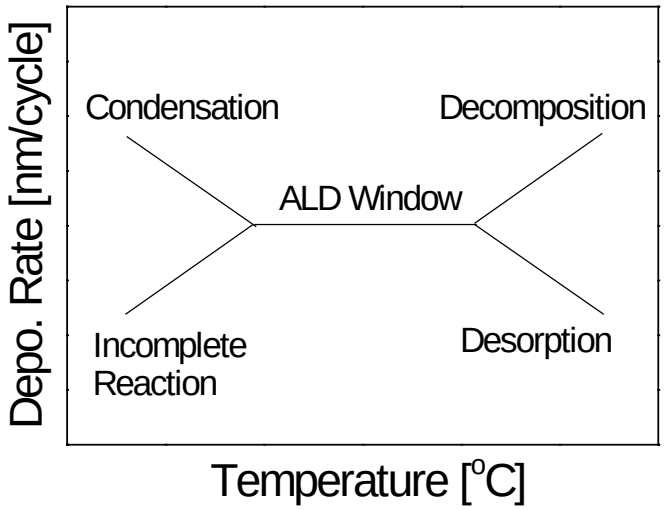

Figure 1.7 ALD temperature window

1.2.5 Reactive Site Density in ALD

There are two factors noticed to cause the saturation of the surface with adsorbed species in a self-terminating gas–solid reaction, as shown in Figure 1.8: the reactive site density and steric hindrance of the ligands.[9] Reactive site density, which is similar to OH density on the surface, in ALD is normally known to be 1~7 x $10^{14}/cm^2$.[11] Chemical oxide grown by water or ozone has the highest OH density of 7 x $10^{14}/cm^2$. Silicon oxide grown by thermal oxidation shows the reactive site density between 1 x 10^{14} and 7 x $10^{14}/cm^2$ according to the process condition. Si surface treated with HF has the lowest OH density of much less than 1 x $10^{14}/cm^2$. The L/M ratio in the adsorbed ML_x (M:metal, L:ligand) can be varied by the OH density, which results in the variation of the amount of adsorbed total M. On the other hand, the partial pressure of a precursor is normally from a few to a few hundred mTorr.

.

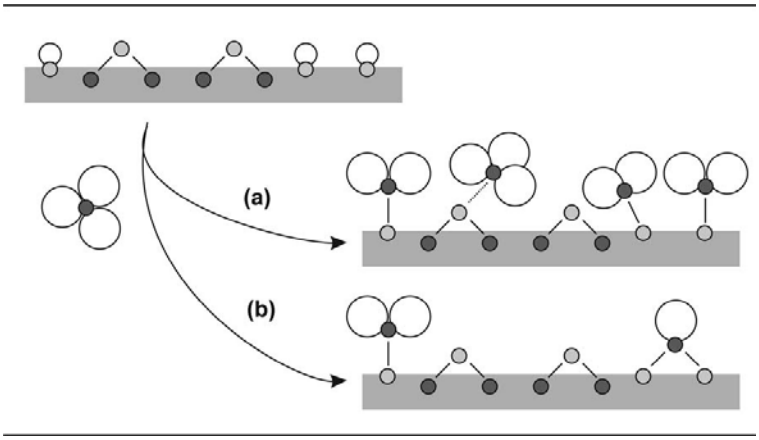

Figure 1.8 Factors identified to cause saturation of irreversible chemisorption: (a) steric hindrance of the ligands and (b) number of reactive surface sites.

1.2.6 Effect of Temperature on the Growth Rate in ALD

The growth rate per cycle (GPC) in ALD has typically the temperature dependency. It can come at least from the effect of temperature on the number and type of reactive sites present on the surface before and after the chemisorption, and from the effect of temperature on the preferred reaction mechanisms.

Four characteristic ways the GPC may depend on temperaturein the ALD windoware illustrated in Figure 1.9.[9] As shown in Figure 1.9(a), the GPC may decrease with temperature. This happens typically when increasing the temperature decreases the number of reactive surface sites and when the number of reactive surface sites affects the amount and/or the type of chemisorbed species. Increasing the reaction temperature may also change the inherent reaction mechanisms. The GPC may stay constant with temperature (Figure 1.9(b)). This can occur, for example, if steric hindrance causes saturation and the number of reactive sites does not affect the amount of adsorbed species. Sometimes, the GPC settles to different constant values at different temperature. The GPC can also increase with increasing temperature as shown in Figure 1.9(c). At higher temperatures, some energy barriers may be overcome and reactions occur, which do not occur at lower temperatures. Also, the GPC can also increase first and then decrease with temperature as shown in Figure 1.9(d). This is the

combination of the cases of Figure 1.9(a) and (c). In other words, some reactions are activated with increasing temperature, after which the decreasing number of reactive sites starts decreasing the GPC. However, this can also be an artifact caused by incomplete reactions: the GPC has been measured for a constant reactant exposure as a function of temperature, and at lower temperatures with lower reaction rates and slower mass transport, the reactions have not been completed.

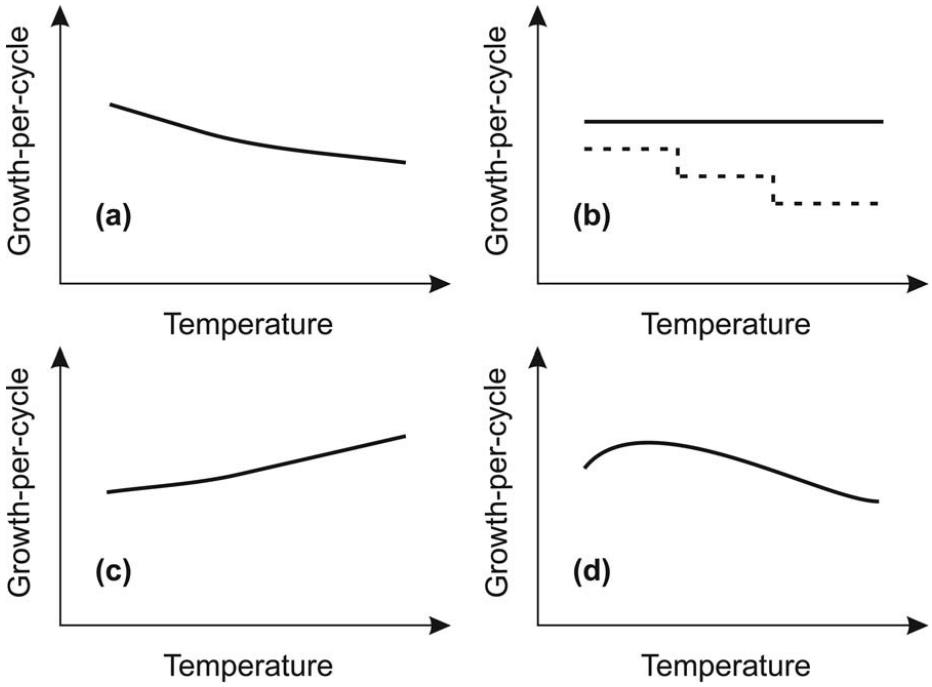

Figure 1.9 Variation of the GPC with the ALD processing temperature in the ALD window.

1.2.7 Steric Hindrance

As illustrated in Figure 1.8, the steric hindrance of the ligands effects the saturation of the surface with adsorbed species in a self-limiting gas–solid reaction along with the reactive site density. While the reactive site density influences early stage of thin film deposition, the steric hindrance of the ligands affects when certain film formation is completed. Three models have been developed for analyzing the growth rate per cycle (GPC) when steric hindrance causes saturation, as summarized in Figure 1.10.[9] Model I helps to estimate the maximum GPC from the size of the ML_n reactant (Figure 1.10(a))(M: metal L : ligands.).[131415] The size of the ML_n reactant is calculated from the density of the liquid reactant and the area covered by the reactant, assuming aclose-packed monolayer of ML. Because the chemisorbed ML_x species differs from the ML reactant, however, Model I gives at best a rough estimate of the achievable GPC.

Model II is for calculating the maximum GPC from the size and geometry of the adsorbed ML_x species (Figure 1.10(b)).[16] The sizes of the ligand Land the metal M must be known. Also the bond lengths and angles must be known or assumed for the adsorbed species. In Model II, the GPC increases in steps with decreasing size of the adsorbate ML_x.

Model III demonstrates how to calculate the maximum GPC from the

size and number of the adsorbed ligands L (Figure 1.10(c)).[17] A theoretical maximum amount of ligands adsorbed is calculated assuminga close-packed monolayer of the ligands. This theoretical arrangement corresponds to a “physisorbed monolayer” of the ligands. A theoretical maximum is calculated for theamount of metal M adsorbed by dividing the amount of ligands adsorbed by the L/M ratio in the ML_z adsorbate. As should be expected, the GPC increases with decreasing size of the adsorbate.

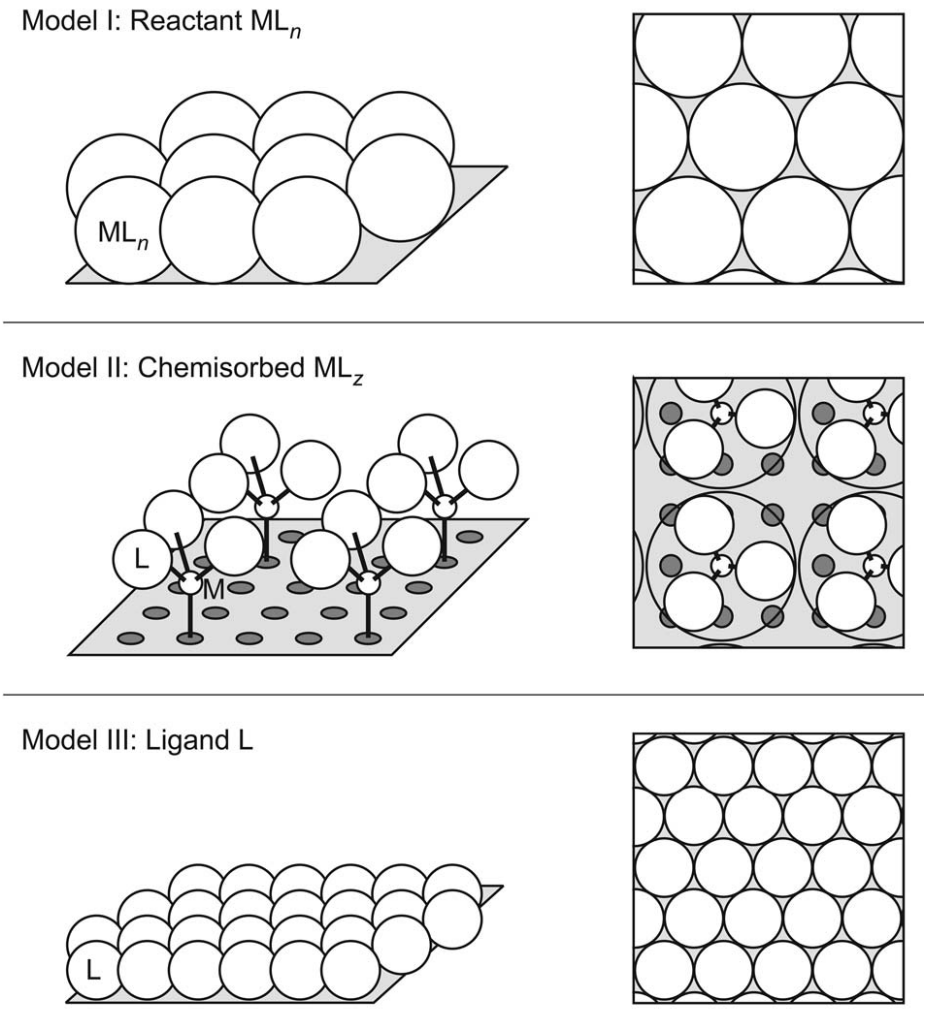

Figure 1.10 Schematic illustration for analyzing sterically hindered chemisorption on the basis of the size of the ML_n reactant.[9]

2 LITERATURE REVIEW

2.1 Plasma Enhanced Atomic Layer deposition

2.1.1 Basic Concept of PEALD

The ALD process usually consist of following four steps: a precursor exposure step, an evacuation or purging step for removing surplus precursors and any byproducts from the chamber, a reactant exposure step, and an evacuation or purging step for the reactants and byproduct molecules from the chamber. There are no fundamental differences in other process steps of thermal ALD and plasma enhanced ALD (PEALD, or plasma assisted ALD, PAALD), except that the plasma is activated for the reactant exposure step in PEALD as illustrated in Figure 2.1.[18] Through the creation of radicals and ions using plasma, the reactant molecules become highly reactive, resulting in changes in the growth characteristics and film properties.

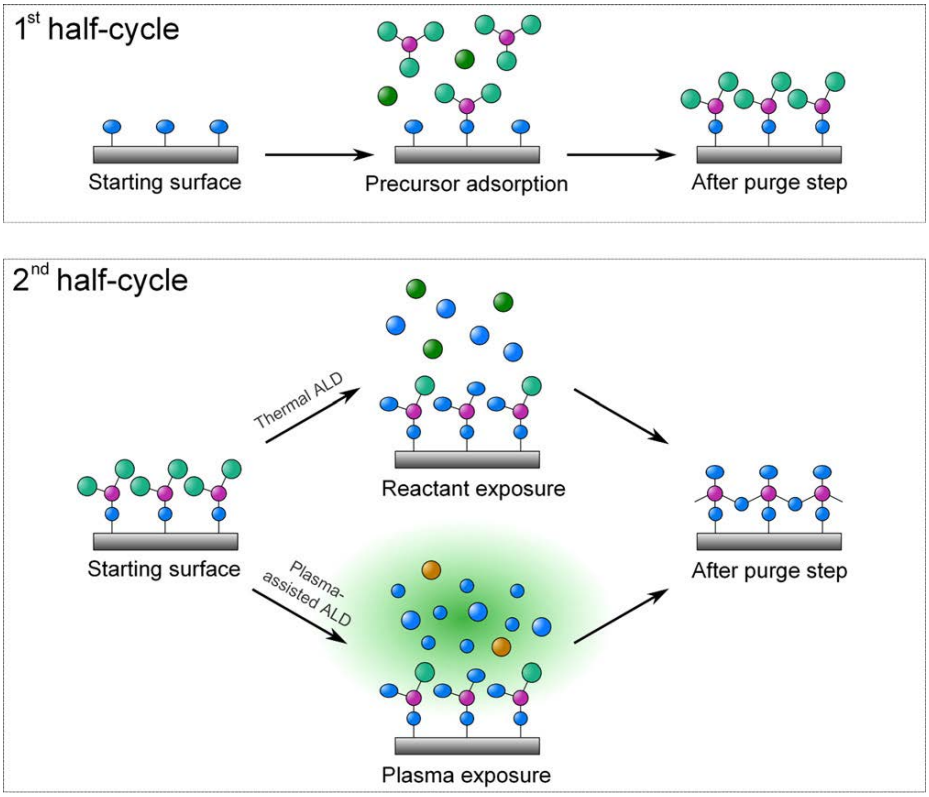

Figure 2.1 Schematic representation of thermal ALD and plasma-assisted ALD.[18]

2.1.2 Merit of PEALD

Due to the use of radicals and ions generated inside the plasma, PEALD has different growth characteristics from thermal ALD. Therefore, the use of plasma-assisted ALD for ultra-thin film synthesis has several potential advantages, in addition to the benefits provided by the ALD technique itself.

By adopting PEALD, improved properties of deposited material can be obtained. It has been reported that, for some materials and applications, plasma-assisted ALD affords better material properties than thermal ALD in terms of, for example, film density, impurity content, and electronic properties. In most cases, these improved material properties are a result of the high reactivity provided by the plasma, which will be addressed in more detail below. However, improvement can often be attributed to kinetically driven, selective ALD surface reactions, for example, the abstraction of surface halogen atoms by H radicals and several ion-assisted surface reactions.[18]

Also, the range of ALD process temperature could be widened with PEALD compared to that of thermal ALD. as shown in Figure 2.2.[19] As high reactivity is delivered to the deposition surface by the plasma species, less thermal energy is required at the substrate to drive the ALD surface chemistry. This means that it is possible to deposit films

with equivalent material properties at lower substrate temperatures than for thermal ALD. The reactivity delivered by the plasma species is not only provided by reactive plasma radicals but is also determined by the kinetic energy of the ions accelerated in the plasma sheath, the surface-recombination energy of the ions and other species, and the energy flux caused by the plasma radiation.[19]

In addition, PEALD provides wider choices of precursors or substrate material than conventional thermal ALD because of the fact that highly reactive plasma radicals are delivered to the deposition surface. Therefore, such precursors, which require more reactive co-reactants due to no or low reactivity with H_2O, for example, β-diketonate precursors can be adopted to ALD process.[20] Furthermore, plasma-assisted ALD allows for a wider choice of substrate materials to be used, particularly those which are temperature-sensitive.[21]

Better control of the ALD surface chemistry and of the species incorporated into the film can be achieved with PEALD because non-thermally-driven reactions can be induced at the deposition surface due to the nonequilibrium conditions in the plasma. Therefore, the use of plasma provides additional variables with which to tune the stoichiometry and composition of the films.

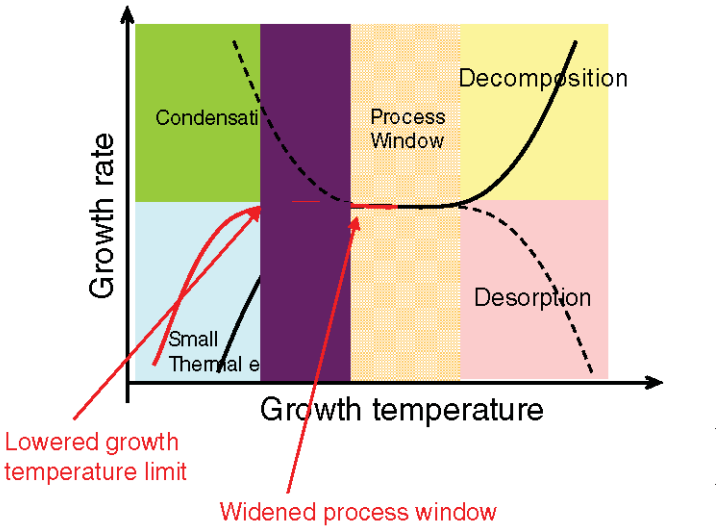

Figure 2.2 General growth characteristics of ALD as a function of growth temperature.[19]

2.1.3 Modeling of PEALD

The basic concept of PEALD is the use of plasma for increasing the reactivity of a reaction which has low reactivity. Therefore, in such process, which has low GPC at low temperature, ALD window can be expanded, as shown in Figure 2.2. The reason why GPC of PEALD could be higher than that of thermal ALD can be understood with the sense of the basic concept of plasma.

A plasma is a collection of free, charged particles, among other gas-phase species, which is, on average, electrically neutral.[22] This so-called quasi-neutrality means that at macroscopic length scales (typically>1 mm) the electron density is equal to the ion density. Plasmas are created by electrical fields which lead to acceleration and heating of the electrons. Typically, the average electron temperature is3.5×10^4 K (approximately 3 eV) while the gas temperature stays low (~300–500 K). Also, the fractional ionization or “ionization degree” of processing plasmas is very low, typically withinthe range 10^{-6}–10^{-3}. This means that the fluxes of electrons and ions to the deposition surface are much lower than the flux of the plasma radicals. Therefore, in many cases, the surface chemistry is ruled by the interaction of the plasma radicals with the surface species. However, the energy of theions, E_{ion}, arriving at the surface can be much higher than the ion or electron temperature, as ions are accelerated within a thin positive

space-charge layer, the “plasma sheath,” at the boundary between the plasma and the substrate. This plasma sheath develops because the electron thermal velocity is much higher than the ion thermal velocity. The positive ion collides to the substrate is accelerated by the potential created by the plasma sheath(Eq. 2.1). At relatively low pressures, the ion mean free path is larger than the plasma sheath thickness, such that the ions can be accelerated over the full sheath and energy of the ion can be described as Eq. 2.2. Therefore, the energy level of the ion is typically few tens of eV, as shown in Figure 2.3.[18]

$$V_p - V_f = \frac{T_e}{2e} + \frac{T_e}{2e}\ln\left(\frac{T_e}{2\pi m_e}\right) \text{ ---- Eq. 2.1}$$

$$E_{ion} = \mathrm{e}\left(V_p - V_f\right) \text{ ---- Eq.2.2}$$

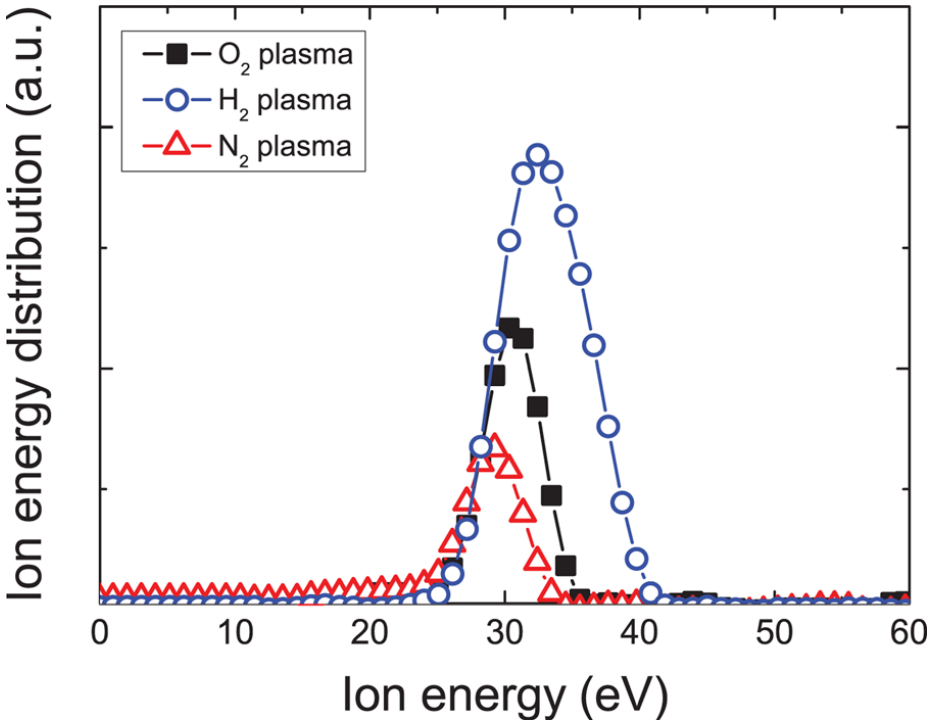

Figure 2.3 Ion energy distribution remote plasma-assisted ALD measured by a retarding field energy analyzer (operating pressure: 8 mTorr; plasma power: 100 W)[18]

2.2 Atomic Layer Deposition of Silicon Nitride

There are few reports on ALD of silicon nitride and reports of using silicon sources with organic ligands have not been published. In the most of the reports, ALD SiN was deposited using (SiH_2Cl_2) (dichlorosilane, DCS) or $SiCl_4$ (tetralchlorosilane) and NH_3.[23-25,26,27] Hong et al. reported ALD SiN layer and SiN/SiO_2/SiN multilayers as gate dielectric for flash memory.[23] Yang et al. has reported that using ALD SiO_2 and ALD SiN as spacer and silicide blocking layer resulted in improved short channel effects for 90 nm technology. [24]

However, chlorine-based silicon precursors have low reaction probability,[28] which leads that the adsorption step of silicon precursors required much exposure dosage of 10^9 Langmuir (1Langmuir = 10^{-6} torr • sec). In addition, if the chlorine ligand cannot be properly desorbed from substrate in the low-temperature, the chlorine residue can attack the key devices components such as metals contacts.[29] To obtain low temperature SiN films processed by ALD method, catalysis such as plasma or tungsten filament have been reported.[27,30] Gotoet. al. reported that ALD SiN films were deposited at the growth per cycle (GPC) of 0.1 nm/cycle at 375℃ using SiH_2Cl_2 (DCS) and ammonia plasma. However, the silicon precursor exposure time was above 60 seconds.[27] Other method introduced tungsten catalyst at the process temperature of 375℃, which tungsten filament was exposed to

activate ammonia gas.[30,31] However, the total deposition time for one cycle was about 220 to 400 seconds. Therefore, the reactive silicon precursor for ALD process should be investigated for minimizing the exposure time of silicon precursors, and catalysis should be introduced to obtain the low process temperature. Plasma-enhanced atomic layer deposition (PE-ALD) process has been developed for many electronic materials, but there were few papers about silicon nitride films, and only silicon nitride films embedded with metal was reported recently.[29,32]

2.3 Spatial Atomic Layer Deposition

2.3.1 General Concept of Spatial Atomic Layer Deposition

The difference between conventional ALD andspatial ALD is the system the precursors are delivered to the substrate (Figure 2.4).[33] In conventional ALD the precursors are dosed into a chamber sequentially, separated in time by a purge step [Figure 2.4(a)]. In spatial ALD, the precursors are supplied continuously, but in different physical locations [Figure 2.4(b)]. Thus there are multiple zones where a half-reaction can take place when a substrate is located in the one of zones. The substrate is present in such a half-reaction zone for a sufficiently long period of time in order to get a saturated monolayer will form from precursor A. After that, the substrate is moved to the second half-reaction zone, where the ALD cycle is completed to form one ALD monolayer. Also, the gas supplies could be moved while the substrate position could be fixed and, or some combination of the two. By repeating this sequence for the desired number of cycles, the thickness of films increases and the targeted thickness can be obtained.

Summarizing, the three main concepts of spatial ALD are: (1) physically separated half-reactions zone, (2) movement of the gas injector head and/or substrate, and (3) a barrier between the half-reaction zones to prevent precursor mixing.[33]

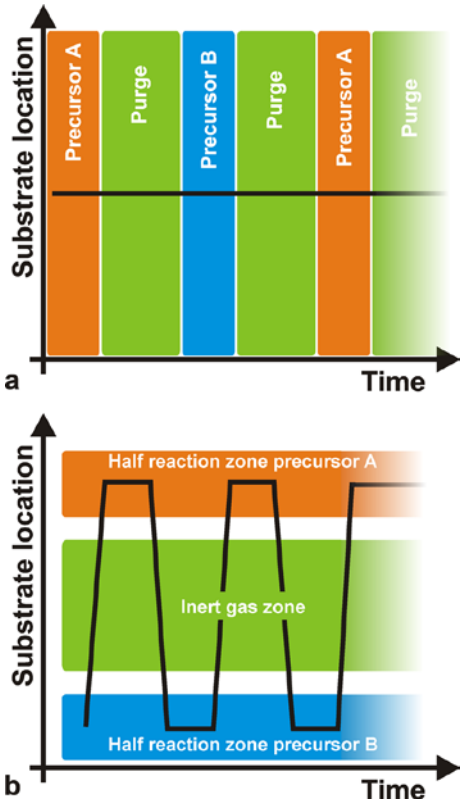

Figure 2.4 Schematic representation of the ALD process(a) Conventional ALD (b) Spatial ALD[33]

2.3.2 Characteristics of Spatial ALD

The main advantage of spatially separating the half-reactionsis that the purge steps between the precursor dosages in conventional ALD become significantly reduced. The main essence of ALD lies in decoupling the multiple independent half-reactions, which requires a complete separation of the precursors with no intermixing precursors whatsoever. In conventional ALD this is achieved through the use of purge steps in between the precursor exposure steps. Because deposition will not only take place on the substrates, but on the reactor walls as well in conventional ALD, the purge step needs to be sufficiently long enough to remove remaining precursors or reactant in the entire reactor. In spatial ALD, on the other hand, the half reactions are separated using a combination of physical barriers and continuously flowing purge streams to prevent the inter-diffusion and mixing of the precursors. Therefore, each reaction zone has only one kind of reactant or source and the longer purge step is not necessary. As a consequence, the available net deposition rate is no longer limited by the accumulated individual cycle step times, but by the time required to move between half-reaction zones.[34] Of course the ultimate limit depends on the kinetics of the specific reaction involved, but this can be of the order of a few milliseconds when using planar substrates. For substrates with more complex topographies, required

exposure times will scale dictated by transport limitations at the feature scale, similar to conventional ALD.[35]

Furthermore, a significant reduction of precursor consumption and consequently the cost of ownership can be achieved. In conventional ALD, the purge steps in between the half reactions will remove any extra precursor from the reactor, making it unavailable for incorporation into the deposited film. This results in an inherently poor precursor utilization efficiency, constraining the ability to employ costly precursors for large scale applications. In spatial ALD, the separation of the reaction zones combined with barriers to prevent mixing ensures that precursors never reside in the same reactor volume. As a consequence, the only places where deposition will take place are on the substrate and no parasitic deposition on the reactor walls will occur. Therefore, efficient precursor consumption can be achieved. In addition, unreacted precursor could be more efficiently recycled with the advanced purified technique.

Also, atmospheric ALD can be achieved with spatial ALD. By using concepts of gas baring and of a very close proximity of the substrate to the precursor injector to ensure precursor separation (Figure 2.5), the reactor can be completely independent of the environment, enabling operation under atmospheric pressure conditions.[33]

The other expected advantage of the continuous gas supply is stable pressure in each area of the chamber. When plasma-enhanced atomic

layer deposition (PEALD) is used, this can yield a major improvement compared to the conventional pulse/purge ALD equipment. In PEALD using an SALD system, plasma excitation and radicalization are applied to the reaction gases that are continuously supplied, and thus, the plasma can be more stably controlled. Consequently, formation of high-quality thin films is expected.[36]

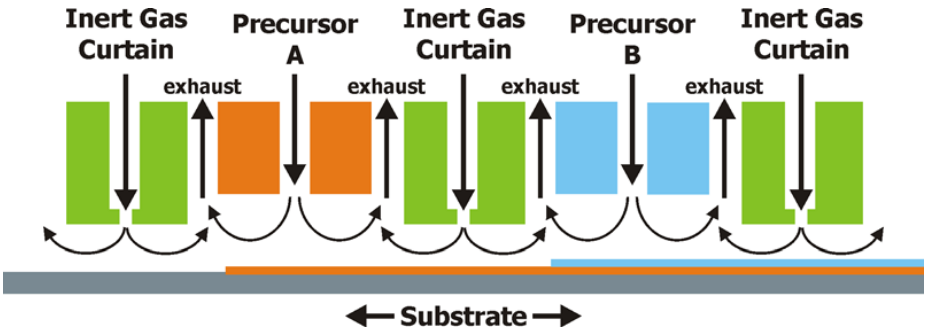

Figure 2.5 Principle of a close proximity spatial ALD reactor concept[33]

2.3.3 Trends of Spatial ALD

Although there have been several recent developments in spatial ALD, the original idea was already patented in 1977 by Suntola et al.[37,38] (Figure 2.6(a)). They described the concept of spatially separating the half-reactions, with separate precursor inlets and exhausts. In their patents, the authors describe the use of inert gas for separating the half-reaction zones, where the gas shield width should be designed wide enough to prevent any diffusion and cross-reactions between the precursors.

At the Advanced Surface Technology Research Laboratory (ASTRaL) of Lappeenranta University of Technology (Finland), another spatial ALD concept for depositing on flexible substrates has been developed. They have chosen to pass the flexible web around a large rotating drum adjacent to the various gas inlets and purge zones. A schematic of this process is shown in Figure 2.6(b). One rotation of the cylinder is equivalent to one ALD cycle. Experimental depositions with this system have shown that the process behaves as a conventional ALD process in that the deposition rate per cycle saturatesas the precursor flow rate is increased, reaching approximately 0.1 nm/cycle for the TMA/water process for Al_2O_3 at a temperature of 100 ^{o}C.[39]

Cambridge NanoTech (Cambridge, USA) is developing their own spatial ALD concept, referred to as zone separated ALD. This concept

is based on a manifold/cell design (Figure 2.6(c)) involving the operation of the cell underchoked flow conditions. Under these conditions gases are supplied via the manifold to the input side of the cell underchoked flow operation at atmospheric process pressure. Choked flow operation is beneficial in that variations in the process pressure will have no impact on the flow through the cell.[40]

Using a very close proximity of the substrate to the precursor injector (<100 lm) is widely adopted to ensure precursor separation. In such a concept, as illustrated schematically in Figure 2.5, the reactor has separate zones exposing the precursors one by one to a substrate that moves underneath the reactor. Between and around the reaction zones, there are shields of inert gas again to separate the precursor flows. When operated properly, these gas shields can act as gas bearings, facilitating virtually frictionless movement between reactor and substrate. When a gas bearing is used, the distance between the reactor and substrate can be minimized and made very accurately and controllable of the order of several tens of micrometers. These small gap heights combined with the resulting high flow rates in the gaps form excellent diffusion barriers with relatively narrow widths. An additional benefit of using gas-bearings is that they completely seal off the reaction zones, making the reactor completely independent of the environment, enabling operation under atmospheric pressure conditions. In and around 2008 several groups have independently

filed patents on gas bearing based spatial ALD concepts.[33]

Levy et. al. (Eastman Kodak) developed the spatial ALD system that the substrate is allowed to approach the head until the pressure field resulting from the gas flow hydrodynamically supportsthe substrate [Figure 2.7(a)]. Because the system operates as agas bearing and the substrate is maintained in close proximity to the coating head without the need for extremely high tolerance mechanical fixtures. The main application this group has been working on is thin film transistors where Al_2O_3 and ZnO are deposited with their setup[41].

P. Poodtet. al. (TNO) combined their gas bearing technology with atmospheric pressure gas phase deposition technology. [34,42] The half-reaction zones are incorporated in a round reactor head surrounded by exhaust zones [Figure 2.7(b)]. These zones are surrounded by gas bearing planes. The reactor head is mounted on top of a rotating substrate table. The entire construction is mounted in a convection oven. Their main focus was ALD of aluminaas surface passivation layers on crystalline silicon solarcells.[34]

L. Hennenet. al. (Levitech) developed aspatial ALD tool for the passivation of silicon solar cells with Al_2O_3 layers based on the ASM International concept as shown in Figure 2.7(c). Silicon solar cell wafers are transported in a linear track crossing areas with precursor gas curtains.The wafers are transported between two gas bearings, levitating in between a narrow track. Wafers pass such a cell ~1 s

resulting in a throughput of 3600 wafers/h. The total number of ALD cells determines the final layer thickness. For the deposition of a 10 nm layer the tool length will be ~10 ms.[43]

(a)

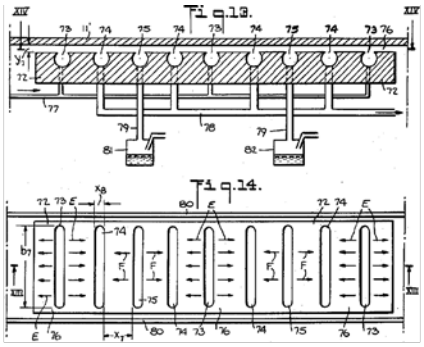

(b)

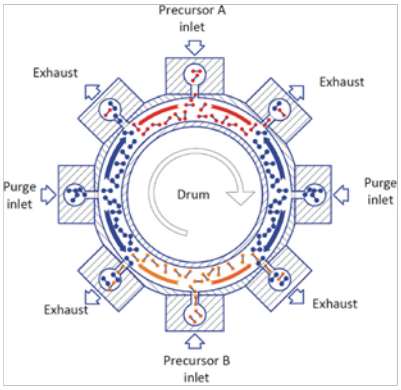

(c)

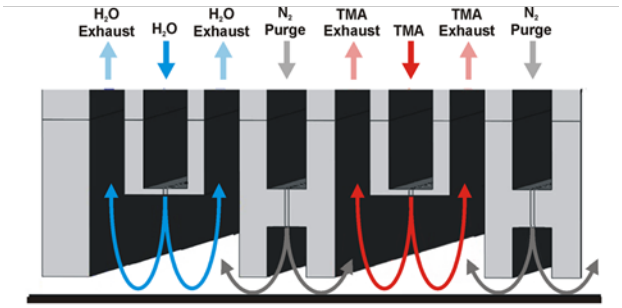

Figure 2.6 Schematic design of several spatial ALD systems.[38-40]

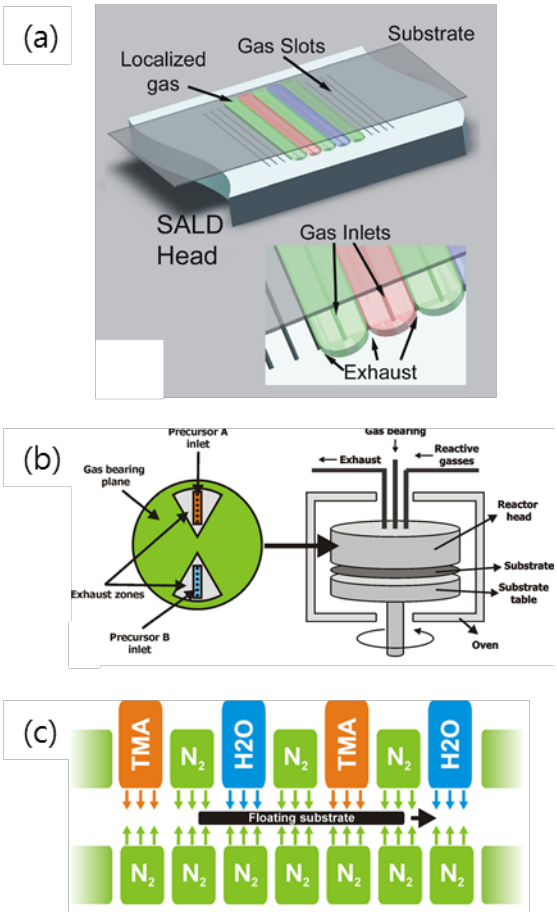

Figure 2.7 Schematic design of spatial ALD systems using gas baring.

2.4 Atomic Layer Deposition of Al_2O_3 with Tri-methyl-aluminum

Tri-methyl-aluminum (TMA), which has properties as described in Table 2.1, is the one of most commonly used aluminum precursors in ALD. Therefore, TMA is a justified choice if a choice is made to review the growth characteristics. TMA also has several advantages as an ALD sources. Further advantages of using TMA, as a general example, is that the reactions are rather ideal, the TMA reactant is highly reactive and many types of compounds have been grown from it (oxides, nitrides, arsenides, and pure Al) as shown in Table 2.2. Also, the gaseous reaction products (methane) are rather inert. Many other reactant classes, such as elements, halides, alkoxides, β-diketonates, and alkyl/silylamides would have difficulties fulfilling at least some of these criteria, whereas alkyls, cyclopentadienyls, and perhaps amidinates fulfill them better.[9]

The deposition process of Al_2O_3 films is one of the most studied ALD processes. There is therefore material to be reviewed. Most commonly used oxidant source is water but TMA/ozone process also has been well studied.[3,9,44,45,46,47,48]

TMA + H_2O is a near-ideal ALD process that has been extensively studied, and the underlying reactions are well-understood. (Eq.2.3-2.4)

For TMA+ O_3, little had not known about the chemistry underlying its process until S.D. Elliot et. al. suggested the mechanism. (Eq. 2.5-2.8)[45]

i) Half reactions in TMA+H_2O process

$$\mathrm{surf-Al-OH+Al(CH_3)_3}(g) \rightarrow \mathrm{surf-Al-O-(CH_3)_2}$$

---- Eq. 2.3

$$\mathrm{surf-Al-CH_3+H_2O}(g) \rightarrow \mathrm{surf-Al-OH}+C\mathrm{H_4}(g)$$

---- Eq. 2.4

ii) Half reactions in TMA+O_3 process[45]

TMA half reactions:

$$\mathrm{surf-OH^-+Al}(\mathrm{C}H_3)_3(g) \rightarrow \mathrm{CH_4(g)+surf-[OAl}(\mathrm{C}H_3)_2\}^- + O_3(g) \quad \text{---- Eq. 2.5}$$

$$\mathrm{surf-OH^-+surf-[AlC}H_3]^{2+} \rightarrow \mathrm{CH_4(g)+surf-AlO^+}$$

---- Eq. 2.6

O_3 half reactions:

$$\mathrm{surf-C}H_3^- + \mathrm{O(g)} \rightarrow \tfrac{1}{2}\mathrm{C_2H_4(g)+surf-OH^-} \quad \text{---- Eq. 2.7}$$

$$\mathrm{surf-OH^-+surf-OH^-} \rightarrow \mathrm{surf-O^{2-}}+\mathrm{H_2}O(\mathrm{g}) \quad \text{---- Eq. 2.8}$$

Whether which oxidant is used, the deposition properties of TMA

ALD process is almost ideal. For example, as shown in Figure 2.8, the both cases of TMA/H_2O and TMA/O_3 show good self-limiting property.

Formula	**$(CH_3)_3Al$**
Molecular Weight	**72.09**
Density at 20 ℃	**0.752 g/ml**
Vapor Pressure at 20 ℃	**8.7 mmHg**
VP Equation	**$Log_{10}P(mmHg) = 8.22 - 2134/T(K)$**
Gas Density (1.013 bar and 15 °C)	**3.049 kg/m3**
Structure formula of TMA	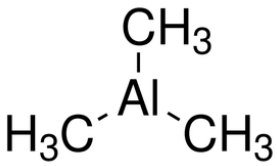

Table 2.1 Physical and Chemical Properties of tri-methy-aluminum precursor.

Z	Material	Reactant A[a]	Reactant B
5 Boron			
	B_2O_3	BBr_3	H_2O
	BN	BCl_3	NH_3
		BBr_3	NH_3
	$B_aP_yO_c$	$B(OMe)_3$	$POCl_3$
6 Carbon			
	C[b]	CF_4	H[c]
		CCl_4	H[c]
12 Magnesium			
	MgO	$MgCp_2$	H_2O
		$Mg(thd)_2$	H_2O_2
		$Mg(thd)_2$	O_3
	MgTe	Mg	Te
13 Aluminum			
	Al_2O_3	$AlCl_3$	H_2O
		$AlCl_3$	O_2
		$AlCl_3$	ROH[d]
		$AlCl_3$	$Al(OEt)_3$
		$AlCl_3$	$Al(O^iPr)_3$
		$AlBr_3$	H_2O
		$AlMe_3$	H_2O
		$AlMe_3$	H_2O_2
		$AlMe_3$	O_3
		$AlMe_3$	O_2[e]
		$AlMe_3$	N_2O
		$AlMe_3$	NO_2
		$AlMe_3$	N_2O_4
		$AlMe_3$	^iPrOH
		$AlMe_3$	$Al(O^iPr)_3$
		$AlMe_2Cl$	H_2O
		$AlMe_2O^iPr$	H_2O
		$AlEt_3$	H_2O
		$Al(OEt)_3$	H_2O
		$Al(OEt)_3$	O_2
		$Al(O^nPr)_3$	H_2O
		$Al(O^nPr)_3$	O_2
	AlN	$AlCl_3$	NH_3
		$AlCl_3$	NH_3+H_2[e]
		$AlMe_3$	NH_3
		$AlEt_3$	NH_3
		$Me_3N:AlH_3$	NH_3
		$Me_2EtN:AlH_3$	NH_3
	AlP	$AlMe_2H$	PH_3
		$Me_2EtN:AlH_3$	PH_3
	AlAs	$AlCl_3$	AsH_3
		$AlMe_3$	AsH_3
		$AlMe_2H$	AsH_3
		$AlEt_3$	AsH_3
		Al^iBu_3	AsH_3
		$Me_3N:AlH_3$	AsH_3
		$Me_3N:AlH_3$	$As(NMe_2)_3$
		$Me_2EtN:AlH_3$	AsH_3
	Al	$AlMe_3$	H_2[e]
	$Al_xSi_yO_z$	$AlCl_3$	$Si(OEt)_4$
	Al_2O_3/SiO_2[f]	$AlMe_3$	$(^tBuO)_3SiOH$
	$Al_xTi_yO_z$	$AlCl_3$	$Ti(OEt)_4$
		$AlCl_3$	$Ti(O^iPr)_4$
		$AlMe_3$	$Ti(O^iPr)_4$

Table 2.2 Aluminum part from Overview of ALD processes based on two reactants[9]

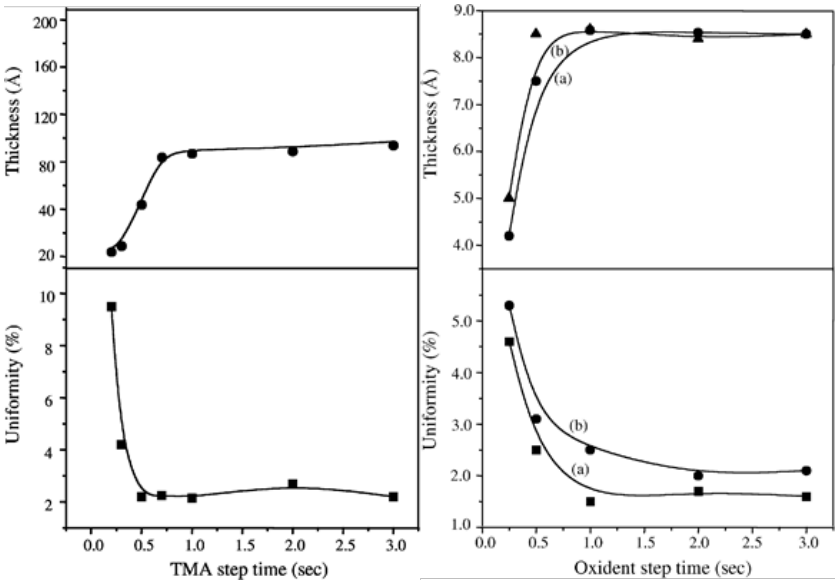

Figure 2.8 Deposition Properties of TMA ALD process.

2.5 Simulation with CFD-ACE+

CFD-ACE+ is a multi-physics module that solves the Navier-Stokes (conservation of momentum), continuity (conservation of mass), enthalpy (conservation of energy) and Stefan-Maxwell (conservation of species) equations simultaneously through a finite volume approach. These equations are listed below in vectorial form;

Momentum:

$$\frac{\partial \rho \boldsymbol{u}}{\partial t} + \nabla \cdot \rho \boldsymbol{u}\boldsymbol{u} = -\nabla \mathrm{p} + \nabla \cdot \tau + \rho \boldsymbol{g} \text{---- Eq. 2.9}$$

Mass:

$$\frac{\partial \rho}{\partial t} + \nabla \cdot \rho \boldsymbol{u} = \mathbf{0} \text{ ---- Eq. 2.10}$$

Energy:

$$\frac{\partial \rho h}{\partial t} + \nabla \cdot \rho \boldsymbol{u} h = \nabla \cdot \mathbf{q} + \tau \cdot \nabla \mathbf{u} + \frac{dp}{dt} \text{ ---- Eq. 2.11}$$

Species:

$$\frac{\partial \rho Y_i}{\partial t} + \nabla \cdot \rho \boldsymbol{u} Y_i = \nabla \cdot j_i + \omega_i \text{ ---- Eq. 2.12}$$

Where ρ, **u**, p, h and Y_i are density, velocity, pressure, enthalpy and

species mass-fractions, respectively, and ω_i is the species production rate per unit volume due to gas-phase reactions. The auxiliary quantities in the above equations may be written as:

Sheer stress:

$$\tau = \mu(\nabla \mathbf{u} + \nabla \mathbf{u}^T) - \frac{2}{3}\mu(\nabla \cdot \boldsymbol{u})\boldsymbol{I} \quad \text{---- Eq. 2.13}$$

Diffusive Energy Flux:

$$\mathbf{q} = \lambda \nabla \mathrm{T} + \sum_i h_i \boldsymbol{j}_i \quad \text{---- Eq. 2.14}$$

Diffusive Species Flux:

$$\boldsymbol{j}_i = \boldsymbol{j}_i^c + \boldsymbol{j}_i^T \quad \text{---- Eq. 2.15}$$

Stefan-Maxwell Diffusion:

$$\boldsymbol{j}_i^c = \rho D_i \nabla Y_i + \frac{\rho Y_i}{M} D_i \nabla \mathrm{M} - \mathrm{M} \sum_j D_j \nabla Y_j - \nabla \mathrm{M} \sum_j D_j \nabla Y_j \quad \text{---- Eq. 2.16}$$

Soret Diffusion:

$$\boldsymbol{j}_i^T = \frac{\rho D_i^T}{T} \nabla \mathrm{T} - \rho Y_i \sum_j \frac{\rho D_i^T}{T} \nabla T \quad \text{---- Eq. 2.17}$$

where μ is the dynamic viscosity, λ is the thermal conductivity, T is the temperature, h_i are the species enthalpies, D_i are the species diffusivities, D_i^T are the species thermal diffusivities and M is the

mixture molecular weight.

Solutions to these equations are generated through a finite volume approach which entails iteratively solving several continuous, simultaneous equations by breaking down a given model into individual three-dimensional spaces. Solutions to the relevantequations can be developed through computational methods that first approximate a set of rough solutions in each volume and then mathematically refine the solutions to minimizethe amount of variation in each iterative cycle by taking into account the properties of the adjacent cells. The addition of user-defined surface and gas-phase chemical reactions allows a deposition rate to be calculated through a multi-step reaction sequence.

CFD-ACE uses both structured and unstructured geometric meshes to break an analytical volume into finite volumes. A structured mesh is one in which all elements are trapezoidal, versus an unstructured mesh which can have triangular and irregular shapes. Unstructured meshes are computationally more expensive and are often used to subdivide geometries which are complex or have curved surfaces. The rectangular nature of the current model lent itself well to structured meshes. It was important to have sufficient density of volume elements near the surface to allow the solver to model the deposition process adequately. It was also important to have sufficient density of volume elements near large changes in physical properties, such as near the end of the injector stem. In CFD-ACE's two-dimensional modeling, the finite

volume elements had the length and width as determined by the mesh and a depth of one radian.

3 EXPERIMENTS AND ANALYSES

3.1 Modified PEALD of Silicon Nitride

3.1.1 Modified PEALD of Silicon Nitride

PEALD deposition system was made by ASM Genitech Co., equipped with a direct capacitive-coupled plasma (CCP) system which directly introduces radicals to the substrate, as shown in Figure 3.1. The showerhead is located at the top of the reactor to supply the electric field of radio frequency (RF), and the heater is located at the bottom of the reactor acting as electric ground. The direct plasma system with showerhead can evenly distribute the plasma radicals and ions to the substrate to achieve uniform film properties as shown in Figure 3.2.[32] Argon gas was used as a carrier gas, and also used as a plasma activation gas to ignite NH_3 plasma. The frequency of CCP system is 13.56MHz, and available power ranges from 0 to 500W.

Bis-diethylamino-silane (BDEAS), tetra-ethylamino-silane (TEAS), tris-isopropylamino-silane (TIPAS) and Di-isopropylamino-silane (DIPAS) were selected as silicon precursors to compare the reaction rate depending on the structure of silicon precursors, and their properties are listed in Figure 3.3. An operating pressure was 3 torr, the power of RF electric field was used in the range from 100 to 300

W, and substrate temperature was between 150 ℃ and 325 ℃. Because of the difficulty of deposition, various ways other than typical PEALD process was tested. They will be discussed in section 4.1.2.

Physical film thickness and refractive index were measured by ellipsometry. Chemical composition of the films was analyzed by the Auger electron spectroscopy (AES) and X-ray photoelectron spectroscopy (XPS). In particular, Fourier transform infrared (FTIR) spectroscopy was adopted to investigate step-by-step reactions.

.

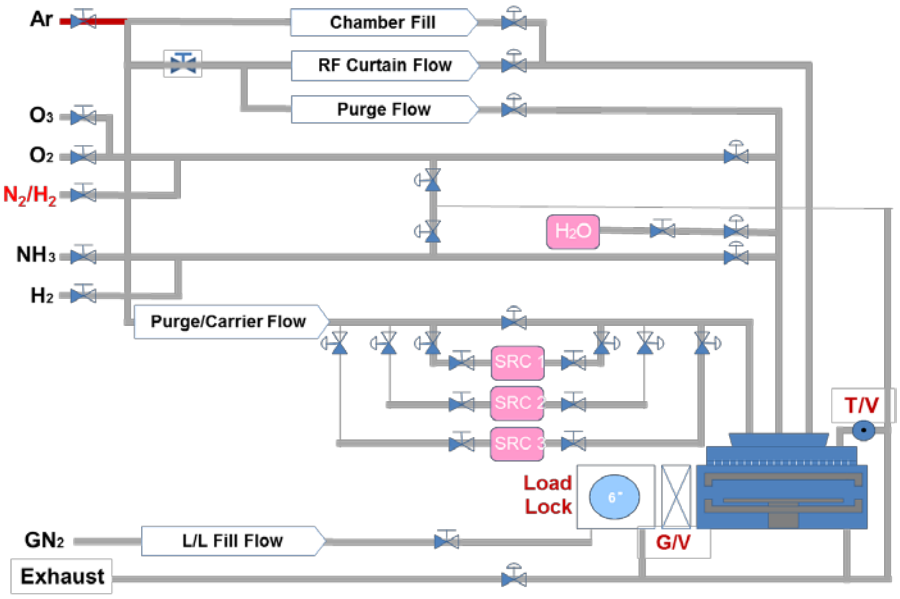

Figure 3.1 Schematic diagram of the PEALD system.

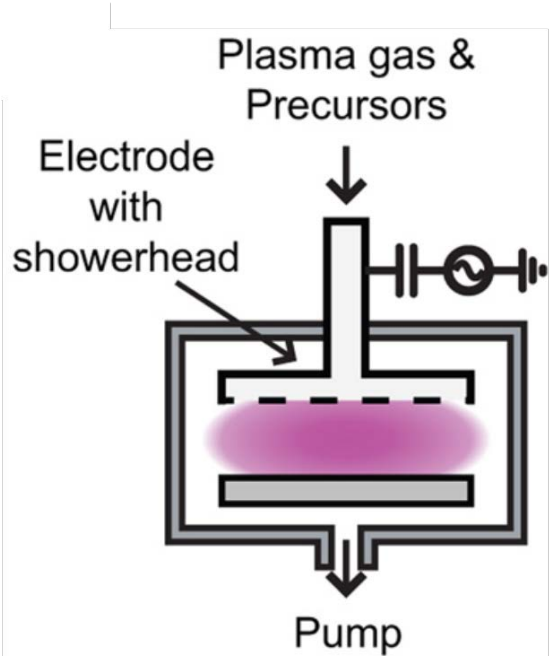

Figure 3.2 Schematic drawing of a direct plasma reactor.

Chemical name	Bis- diethyl-amino-silane (BDEAS)	Tetra-ethyl-amino-silane (TEAS)	Tris-isopropyl-amino-silane (TIPAS)	Di-isopropyl-amino-silane (DIPAS)
Chemical Formula	$H_2Si[N(C_2H_5)_2]_2$	$Si(NHC_2H_5)_4$	$HSi[NH(CH)(CH_2)_2]_3$	$H_3SiN[(CH)(CH_3)_2]_2$
Vapor pressure	1.3Torr at 20℃	1.3Torr at 25℃	6.5 Torr at 30 °C	106 Torr at 55°C
Boiling point	188℃(Melting point : -10℃)	-	165℃	117℃
Density	174.4g/mol	-	203.41g/mol	131.30g/mol
Physical state	Colorless Liquid	Liquid	Colorless Liquid	Colorless liquid
Features	Highly reactive with water	Highly reactive with water	Violently reactive with water	Violently react with water

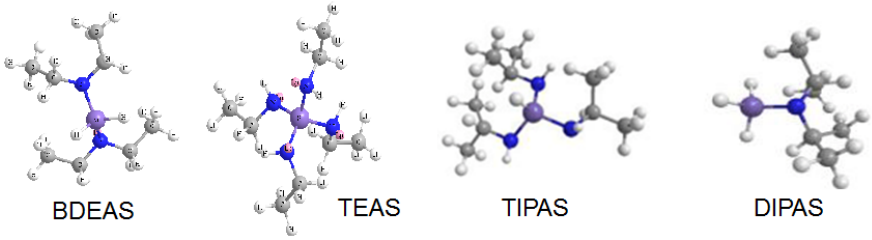

Figure 3.3 Structures and properties of silicon precursors.

3.2 Sptial-type Atomic Layer Deposition of Al_2O_3

3.2.1 Sptial-type Atomic Layer Deposition of Al_2O_3

The SALD chamber was constructed as shown schematically in Figure 3.4. The gas line assembly mounted on the chamber lid connects static gas lines and rotational gas lines as shown schematically in Figure 3.4(d).[49] Each of the static gas lines is connected to the stacked and separated gas transfer zones. The rotation axis part, which includes multiple rotational gas lines with 90-deg bends, penetrates the gas transfer zones vertically. Each rotational gas line is connected to each gas transfer zone through a hole at the side of the rotation axis parts. Magnetic seals and lip seals are inserted in the gas assembly to prevent gas mixing. Through this gas line assembly, the gases are continuously supplied to the inside of the reaction chamber. The supplied gases are retained in plural, spatially separated, rotating cells, while substrates are exposed to the retained gas in sequences. In this study, the substrates, which are Si wafers, remain stationary, while rotating cells provide the Si wafer surfaces with sequential exposure to the reaction and purge gases. As shown in Figure 3.4(b), each space is sectioned off by a partition wall and the reaction cells (the source cell and reactant cell), have the edge walls allowing higher gas pressures. In each cell, by injecting the gas from

the center and pumping it out at the edge, the excess gases are continuously exhausted.

The source gases [tri-methyl-aluminum (TMA) and O_3] are injected from the ports near the center part of the chamber, and the purge gas is injected via a longer injector as shown in Figure 3.4(b). The source and purge gas injectors are located at the top portion of the chamber. Gases are pumped through many holes in the baffle to achieve a lateral flow of gases from the center to the edge. The substrate exposure time ratios between the reaction cells and purge cells are managed by controlling the central angles of these cells. The ratio between the central angle portions of the source cell, the source purge cell, the reactant cell, and the reactant purge cell was 1:2:1:2, which means that the substrate exposure time ratio was also 1:2:1:2. The gap between the walls of the moving parts, such as the partition walls and edge walls, and the substrates on the lower plate was either 10 or 5 mm. The diameter of the lower plate was 60 cm and the height of the wall was 8 cm.

To examine the deposition behavior of SALD, the deposition of Al_2O_3 thin films was tested by using TMA and ozone as the Al-precursor and oxygen source, respectively. The TMA ALD process is chosen for two reasons. First, conventional ALD with TMA has already been intensively studied and well established.[3,44,45,47,48,50] Secondly, TMA has a high vapor pressure and high reactivity. (Table

3.1) As a result, the reactions are almost ideal for ALD.[9] Argon gas was used as a purge gas.

As shown in Table 3.2, the general deposition conditions were as follows: A deposition temperature of 250 ^{o}C, a flow rate of 1000 sccm of argon purge gas, 3 wt. % of ozone in 300 sccm oxygen, and a process pressure of 700 mTorr in the whole chamber. Ozone was produced using an ozone generation system (AX8403, MKS, USA). TMA was supplied to the chamber under its own vapor pressure at room temperature and controlled by a metering valve. The samples were located at three positions: the center, middle, and edge of the lower plate, as shown in Figure 3.4(c). The initials C, M, and E in Figure 3.4(c) and the other Figures in chapter 4 refer to the center, middle, and edge, respectively. Films were deposited on 2 X 2 cm pieces sliced from a p-type 6-in. diameter (100) Si wafer without predeposition HF cleaning so wafers might be saved, although the whole wafer was used in some cases to check the deposition uniformity. Therefore, the Al_2O_3 films are considered to be deposited on the native oxide.

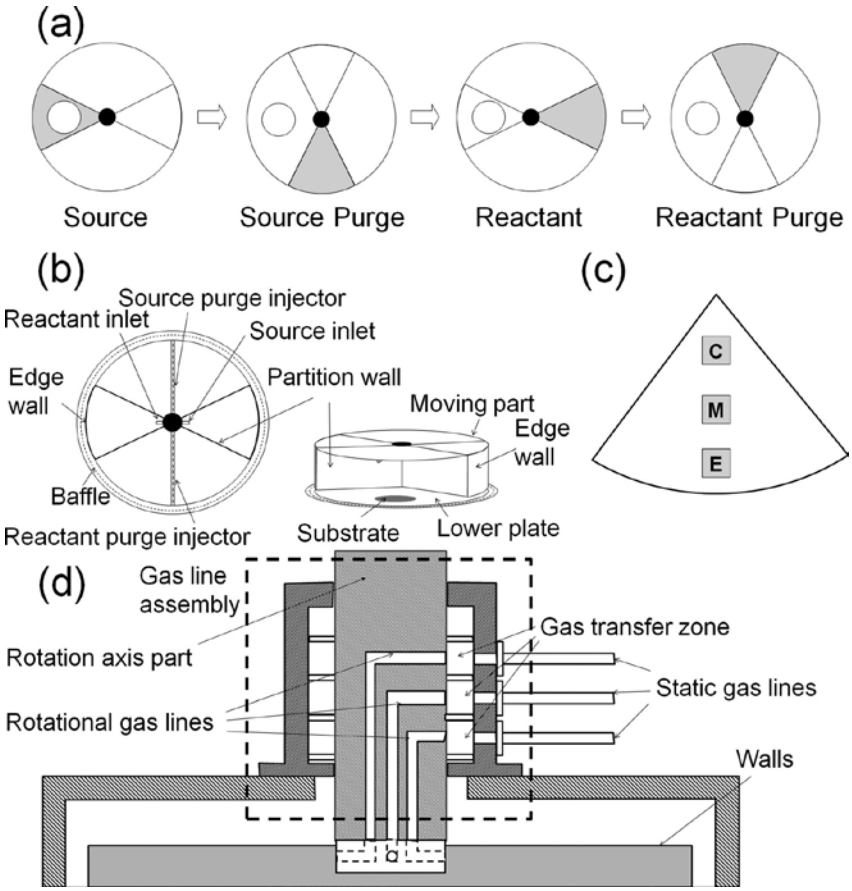

Figure 3.4 Schematic representation of the space-divided ALD. (a) Schematic drawing of the space-divided ALD sequence. (b) Schematic drawing of top view and side view of the SALD reactor. (c) Schematic drawing of the sample location. (d) Schematic drawing of the gas distribution part.

Formula	**$(CH_3)_3Al$**
Molecular Weight	**72.09**
Density at 20 ℃	**0.752 g/ml**
Vapor Pressure at 20 ℃	**8.7 mmHg**
VP Equation	**$Log_{10}P(mmHg) = 8.22 - 2134/T(K)$**
Gas Density (1.013 bar and 15 °C)	**3.049 kg/m3**
Structure formula of TMA	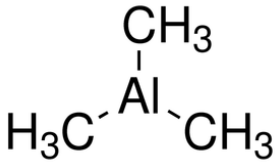

Table 3.1 Physical and Chemical Properties of tri-methy-aluminum precursor.

Substrate Temperautre	**100-300**
Substrate	**P-type Silicon**
Argon purge gas	**1000 sccm**
Ozone	**3 wt. % of ozone in 300 sccm oxygen**
process pressure	**~700 mTorr**

Table 3.2 Process conditions of SALD of Al_2O_3

3.2.2 Gas Flow Simulation with CFD-ACE+

To examine the tendency of gas mixing, gas flow simulations for the spatially separated ALD chamber were also conducted with a 3D calculation grid using the commercial program “CFD-ACE.” The 3D reaction chamber (which had rotational parts inside) was constructed for the simulation of the SALD process as shown in Figure 3.5. This chamber configuration was incorporated into the simulation program as a user-defined subroutine. For the simulations, gas mixing occurred during SALD with alternation of pumping rate, rotational speed, and the gap size between the reactor and substrates. Subsequently, the mole fraction of each gas present during the process was calculated. For simplicity, the baffles at the edge were combined into an edge ring shape space around the lower plate. Also, O_2 (instead of O_2/O_3) was used for the reaction gas and the mass flow rates of the inflow gases, viz. TMA for the source cell, O_2 for the reaction cell, and Ar for the purge cells, were fixed at the same value. The inspected simulated data was obtained from the plane which was 300 lm above the lower plate after three cycles.

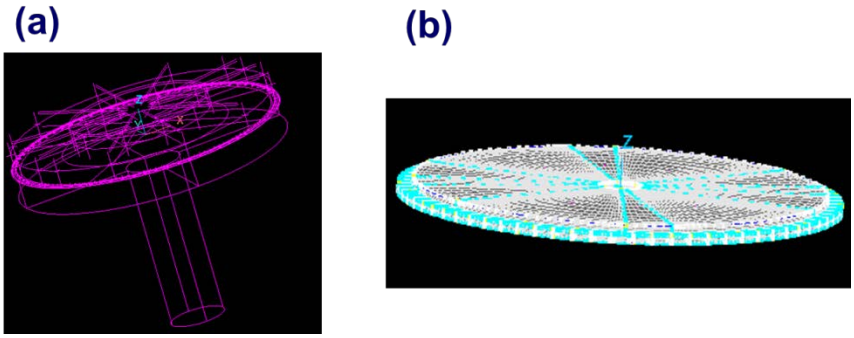

Figure 3.5 Simulation grid of SALD Chamber (a) The gird of the entire SDALD chamber. (b) The grid of a gap between a rotational gas distributor and lower plate.

3.2.3 Analyses of the Deposited Films

The thickness of the deposited thin films was confirmed using an ellipsometer (Gaertner L116 D) and x-ray reflectometry (XRR, PANalyticalX'Pert PRO MPD). To analyze the chemical properties of the films, x-ray photoemission spectroscopy (XPS, ThermoVG SIGMA PROBE) was performed.

The electrical properties were examined using metal oxide semiconductor capacitor structures with a semiconductor parameter analyzer (Hewlett Packard 4140 D). A 100-nmthick platinum layer was deposited as the top layer using a shadow mask in an e-beam evaporator. The electrode area was 60000 μm^2. Indium was coated onto the reverse of each sample for the back contact.

4 RESULTS AND DISCUSSIONS

4.1 Plasma Enhanced Atomic Layer Deposition of Silicon Nitride films

4.1.1 Introduction

Silicon nitride films have been widely used in semiconductor and display industries as capping layer, spacer, etch stopper, anti-reflection layer and gate dielectric. 2010 ITRS (International Technology Roadmap for Semiconductors) showed that three-dimensional (3D) structure has been highlighted for the next–generation device. In order to implement the 3D structure, the channel layer should be changed to the films that can be easily deposited such as amorphous oxide semiconductor (AOS), which has the wide and gap of 3.0eV and the relatively high mobility of ~ 10 $cm^2/V{\cdot}s$.[1] However, the AOS such as Zinc Tin Oxide (ZTO) can be crystallized above 450℃ and form different crystalline phases from 450℃ to 800℃.[2] So, the gate dielectric layer or the trap layer should be processed under 400℃ in order to apply to the AOS channel layer. Meanwhile, silicon nitride films mainly have been processed by Chemical Vapor Deposition (CVD), or Plasma Enhanced Chemical Vapor Deposition (PE-CVD), and the process temperature of conventional CVD process for silicon

nitride films was usually above 600℃ to decompose $SiCl_4$, SiH_2Cl_2 or SiH_4.[51] For lowering the process temperature, catalytic CVD method was introduced using tungsten wires for depositing silicon nitride films at 250℃,[52]and the silicon nitride films were also deposited by plasma enhanced CVD(PECVD) process as low as 200-400℃,[53] or can be even processed under 60℃ by the electron cyclotron resonance plasma CVD method.[54] However, the composition of PECVD films was various depending on their process temperature. In particular, the H concentration was generally high in the films deposited by PECVD process. Therefore, Plasma Enhanced Atomic Layer Deposition (PEALD) method can be one of proper deposition methods to obtain the low temperature silicon nitride films with excellent properties because it has sequential reactions based on self-controlled adsorption and desorption mechanisms of each reaction step to realize the stoichiometry of the target material.[7,9]

Silicon nitride films deposited by ALD method have been reported only a few, and the chlorine was mostly used as a ligand of silicon precursors such as SiH_2Cl_2 and $SiCl_4$.[9,26,27,30,31,55] However, chlorine-based silicon precursors have low reaction probability,[28] so the adsorption step of silicon precursors required much exposure dosage of 10^9 Langmuir (1Langmuir = 10^{-6} torr • sec). In addition, if the chlorine ligand cannot be properly desorbed from substrate in the low-temperature, the chlorine residue can attack the key devices

components such as metals contacts.[29] To obtain low temperature SiN films processed by ALD method, catalysis such as plasma or tungsten filament have been reported.[27,30] Gotoet. al.[27] reported that ALD SiN films were deposited at the growth per cycle (GPC) of 0.1nm/cycle at 375℃ using SiH_2Cl_2 (DCS) and ammonia plasma. However, the silicon precursor exposure time was above 60 seconds. Other method introduced tungsten catalyst at the process temperature of 375℃, which tungsten filament was exposed to activate ammonia gas.[30,31] However, the total depositiontime for one cycle was about 220 to 400 seconds. Therefore, the reactive silicon precursor for ALD process should be investigated for minimizing the exposure time of silicon precursors, and catalysis should be introduced to obtain the low process temperature. Plasma enhanced atomic layer deposition (PEALD) process has been developed for many electronic materials, but there were few papers about silicon nitride films, and only silicon nitride films embedded with metal was reported recently.[18,29,56]

In this chapter, several factors to hinder the deposition of ALD silicon nitride films will be discussed. Most of all, silicon nitride films could be deposited by ALD method using the plasma-activated silicon precursor will be presented.

4.1.2 Conventional PEALD of Silicon Nitride Films

As mentioned in chapter 2, the research of PEALD of silicon nitride has just been paid attention recently and the development of PEALD process of silicon nitride with silicon sources which have organic ligands also has not been investigated yet. However, the PEALD of silicon nitride films seems hard to be applied to mass production until sufficient productivity of the process is guaranteed, which can be achieved by using silicon source with organic ligands because of its high reactivity. Therefore, the development of PEALD using silicon source with organic ligand is very important.

Silicon sources with organic ligands, BDEAS (Bis- diethyl-amino-silane), Tetra-ethyl-amino-silane (TEAS), Tris-isopropyl-amino-silane (TIPAS) and Di-isopropyl-amino-silane (DIPAS) are tested for conventional PEALD SiN process. SiN films were deposited by pure PEALD method and NH_3 plasma. The sequence of pure PEALD cycle consisted of silicon source injection / Ar purge / NH_3 on / NH_3 plasma / Arpurge as shown in Figure 4.1(a). Ar gas flow rate for purge gas and for carrier gas is 200 sccm and 100 sccm, respectively. At 300 ^{o}C, all of the film thicknesses after 100 cycles were under 2nm as shown in Figure 4.1(b), which means that silicon nitride films cannot be grown by conventional PEALD at the given low temperature.

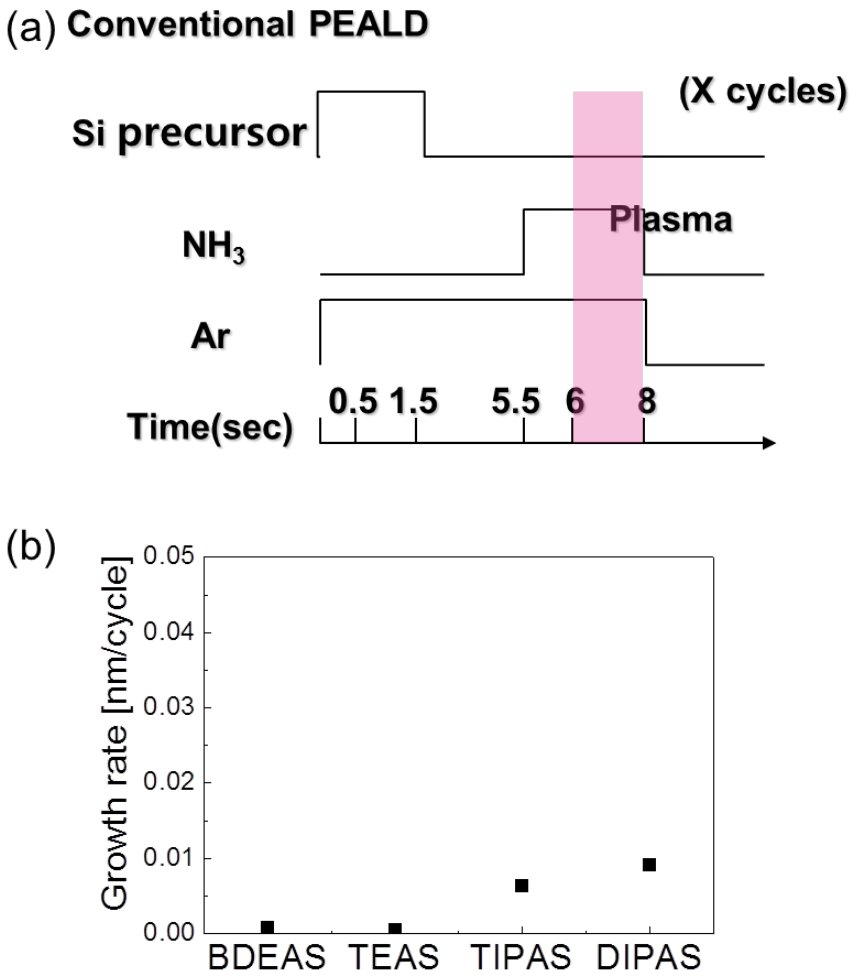

Figure 4.1 Conventional PEALD process of silicon nitride. (a) Process sequence of conventional PEALD (b) Growth rate of silicon nitride films deposited by conventional PEALD process with various silicon sources.

4.1.3 Modified PEALD Processes with Silicon Source Plasma

According to Collin Mui et al., the activation energy for silicon precursor to attack on N-H bonds are higher than that for ammonia to react with Si-H bonds by thermodynamic calculations in the case of the ALD reaction of SiH_4 and NH_3 as shown in Figure 4.2.[31] Also, NH_3 does not react with silicon surface without plasma in NH_3 reaction test at the low process temperature as shown in Figure 4.3. Given the fact that even NH_3 gas cannot react at the low temperature, it is considered that silicon precursor needs extra energy for surface reaction other than substrate heating. Therefore, we adopted the method to activate silicon precursors by plamsa power. However, plasma activation during injection of silicon precursor can cause degradation of step coverage properties. Because of that, the conventional PEALD process was modified as shown in Figure 4.4(a), which will be called as SPNP process (source plasma-NH3 plasma process). The difference between SPNP and conventional PEALD is silicon precursor step and NH_3 reaction and NH_3 purge steps are identical. The key concept of SPNP process is as follows: i) First, silicon precursor physisorbs at the substrate surface. ii) Silicon precursor species, which do not physisorb and stay in the vapor, are purged out by short source purge step with Ar gas. iii) Silicon precursor can be changed to the smaller and reactive precursor by Ar

plasma and reacts with the surface. iv) Byproducts and unreacted species are purged out. In addition of SPNP process, SPxNP and SNP process are also tested. The process sequences of SPxNP and SNP are illustrated in Figure 4.4(b) and (c), respectively. SPxNP process is presented for higher growth rate than SPNP by repetition of silicon source plasma steps. SNP is presented for reducing the chance of injection O component in the deposited films.

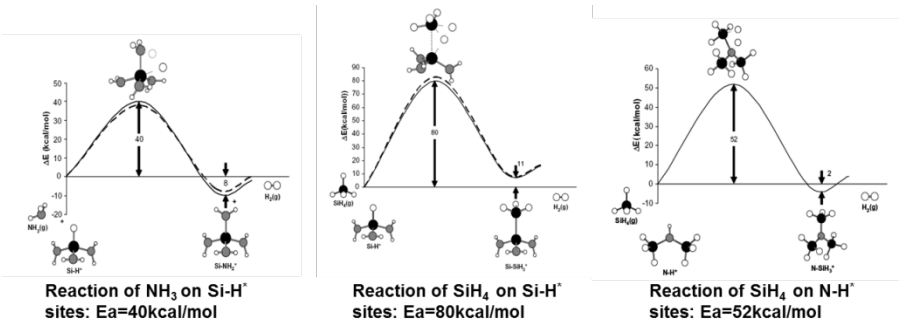

Figure 4.2 Simulation of activation energy in ALD SiN process (sing SiH_4 and NH_3).[31]

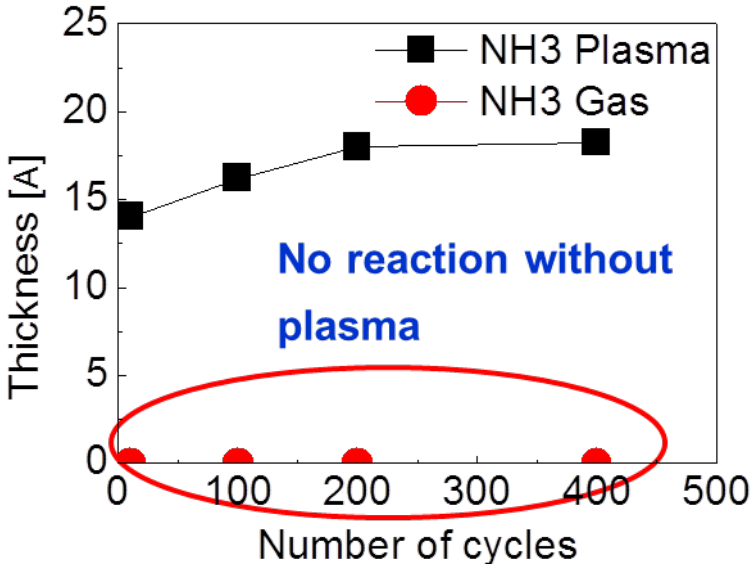

Figure 4.3 Low temperature NH_3 reaction test

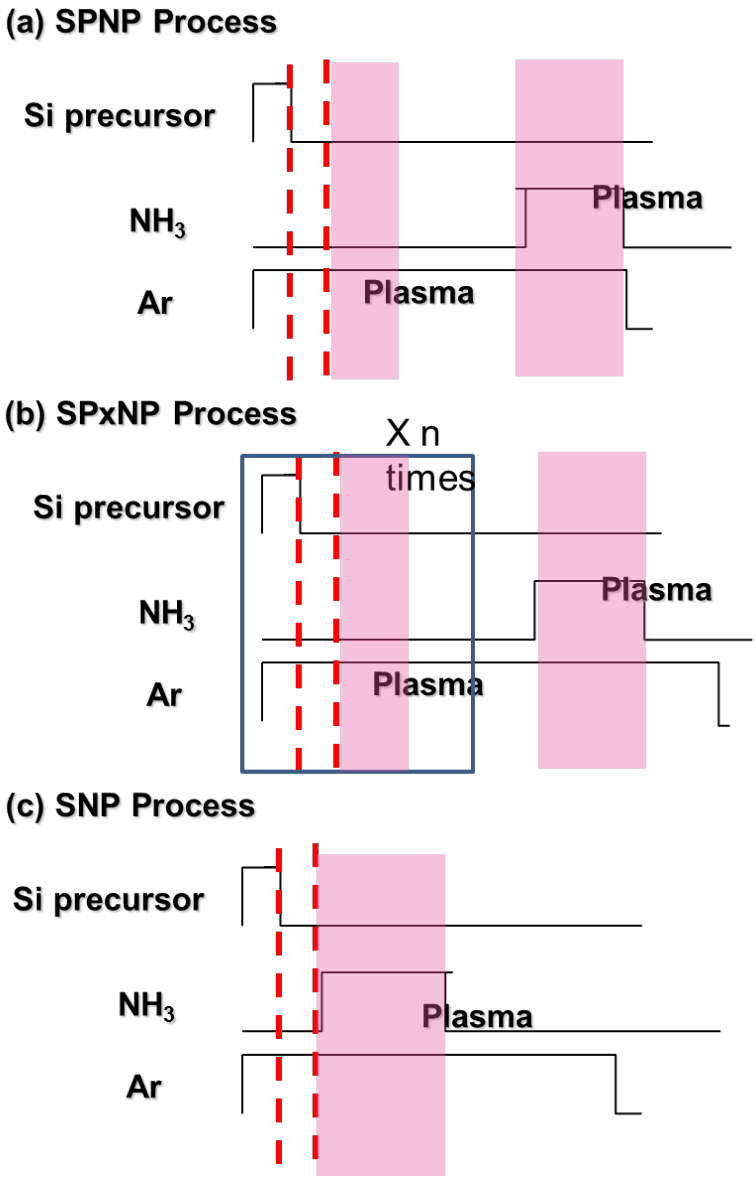

Figure 4.4 Process sequence of modified PEALD silicon nitride (a) SPNP process (b) SPxNP process (c) SNP process

4.1.4 Deposition Properties of Modified PEALD Processes

In order to find out mechanism and optimize process condition, several deposition tests were carried out for each of modified PEALD processes. First, plasma power and NH_3 flow rate split tests were performed to examine which is dominant factor for nitridation efficiency between plasma power and NH_3 flow rate. The process sequence was 0.5/ 1/ 2/ 2/5/2 in terms of souce pulse step time/ source purge step time/ source plasma step time/ source plasma purge step time/ NH_3 plasma step time/ NH_3 plasma purge step time, respectively. As shown in Figure 4.5(a), plasma power does not change refractive index and growth rate significantly. On the other hand, the growth rate and refractive index varied with NH_3 flow rate. In other words, the growth rate and refractive index have no significant differences with different plasma power but shows great dependency to NH3 flow rate. This means that NH_3 flow rate is more important factor to control film properties than plasma power.

The changes of the growth rate and refractive index as a function of silicon source pulse step time, silicon source purge step time and source plasma step time of SPNP process were examined as illustrated in Figure 4.6. The process sequence of the silicon source purge step time test in Figure 4.6 (a) was 0.5 sec/ x/ 2 sec/ 2 sec/ nitridation, which means souce pulse step time/ source purge step time/ source

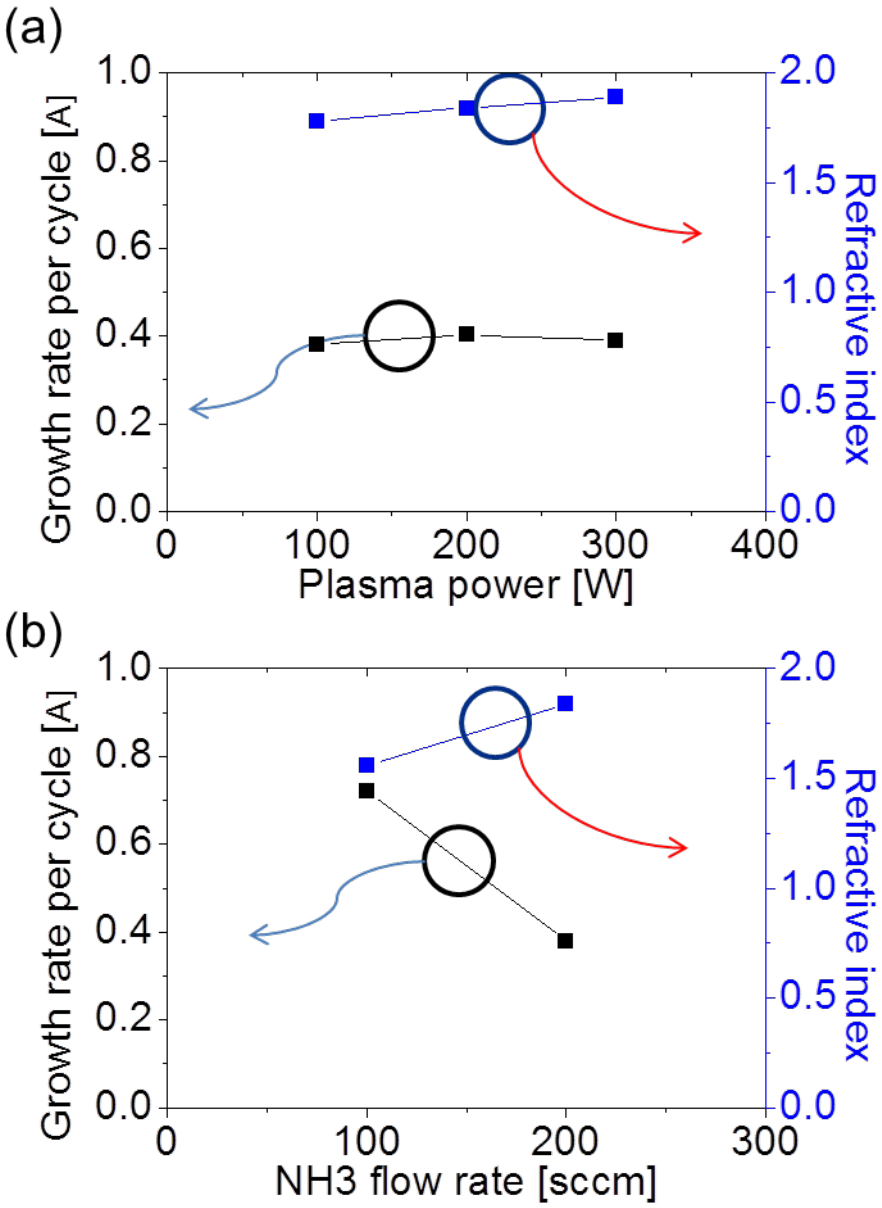

Figure 4.5 Dominant factor for nitridation (a) GPC vs. NH_3 Plasma Power (b) GPC vs. NH3 flow rate

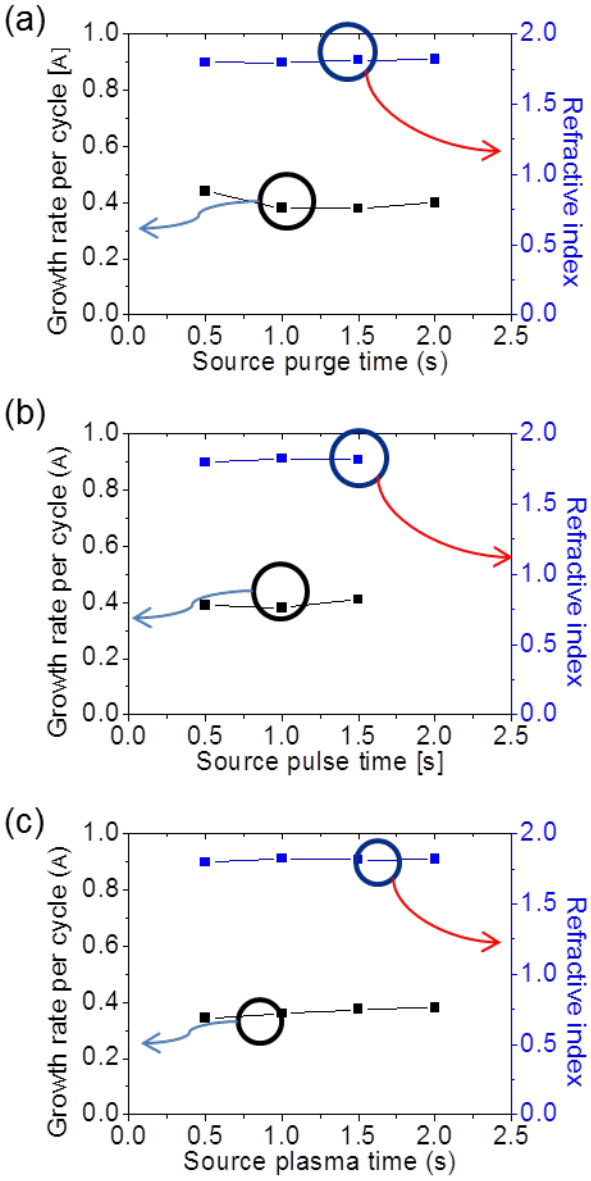

Figure 4.6 Deposition properties of SPNP process (a) GPC vs. source purge time (b) GPC vs. source pulse time (c) GPC vs. source plasma time

plasma step time/ source plasma purge step time/ nitridation, respectively. The process sequence of the silicon source pulse step time test in Figure 4.6(b) was x sec/ 1/ 2 sec/ 2 sec/ nitridation, which means souce pulse step time/ source purge step time/ source plasma step time/ source plasma purge step time/ nitridation, respectively. The process sequence of the silicon source plasma step time test in Figure 4.6(c) was 0.5 sec/ 1/ x sec/ 2 sec/ nitridation, which means souce pulse step time/ source purge step time/ source plasma step time/ source plasma purge step time/ nitridation, respectively. First noticeable point is that the growth rate of modified process is ~ 4 times higher than that of conventional PEALD. Adopting argon plasma successfully increased the growth rate of silicon nitride thin film with saturated refractive index of ~ 1.8. As shown in Figure 4.6(a), the growth rate saturated after 1 sec of purge time, which means that 1 sec seems to be enough to purge silicon sources in vapor. With longer source pulse time and source plasma time, GPC slightly increased but not significantly compared to the increasing tendency of GPC with repetition of source plasma steps in Figure 4.8(a), as shown in Figure 4.6(b) and (c). It was consided as the result of the combination of the two reasons, low adsorption rate of the precursor and existence of the purge step between the source plasma step and the source plasma step. Also, Step time does not effect on refractive index. According to the results from Figure 4.6, possible reaction

sequence of SPNP process is illustrated in Figure 4.7.

The SPxNP process is the modified SPNP process with repeated silicon plasma steps. In order to verify the amount of GPC increase, the tendency of the growth rate with silicon plasma step number was examined as shown in Figure 4.8. Growth rate per cycle (GPC) increased (~2 times) than SPNP process by repeating the silicon plasma step but the refractive index decreased. Even though SpxNP cannot be adopted for silicon nitride films because of O_2 leakage in the chamber, the possibility of control of film properties is confirmed.

Because of oxidation in silicon plasma step in SPxNP process, SNP process was also tested. Because SNP process can be considered as conventional PEALD process with a very short source purge time, step coverage can be poor. However, at very short range of the purge time and with a short and constant source pulse step time, growth rate was almost constant as shown in Figure 4.9. Therefore, Step coverage is not expected excessively badly because amount of physisorbed silicon precursor species is not much diverse in this range. Also, growth rate per cycle increased as 2 times than conventional PEALD.

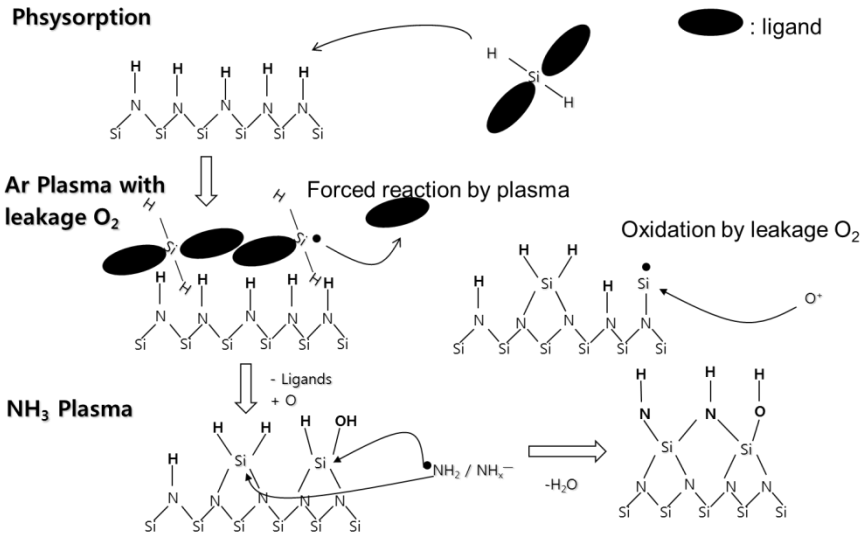

Figure 4.7 Possible Reaction Sequence of SPNP Process

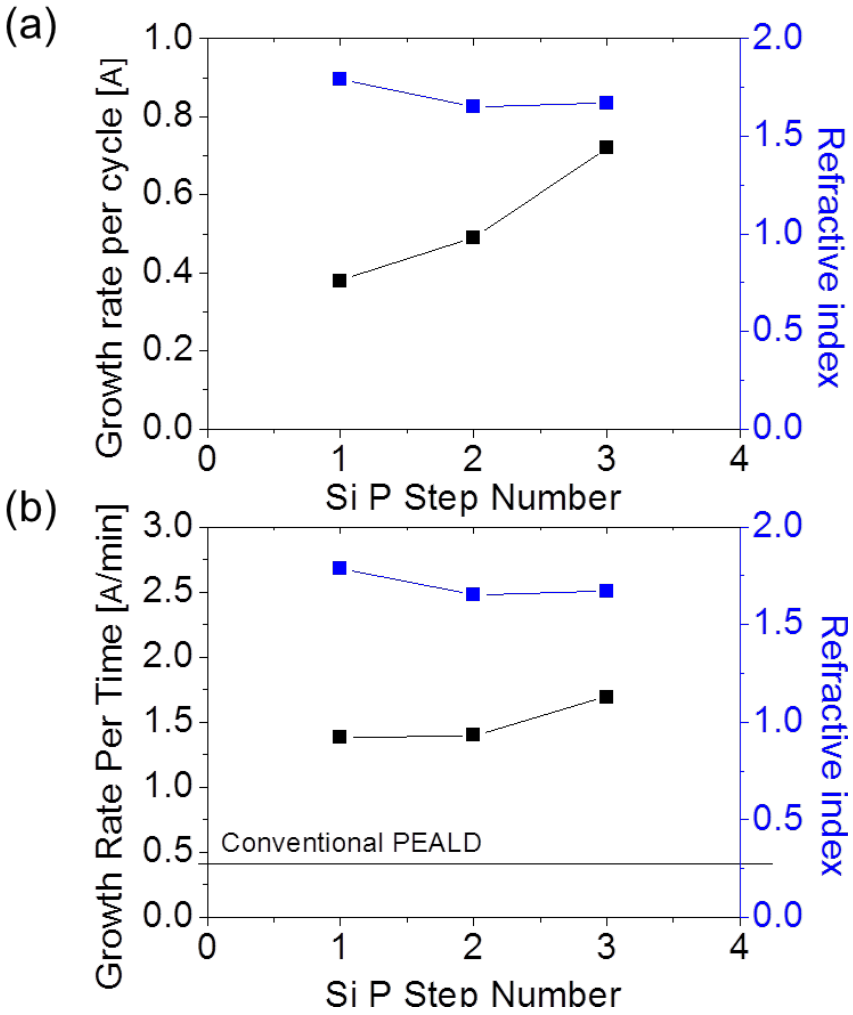

Figure 4.8 Deposition propterties of SPxNP process (a) GPC vs. silicon plasma step number (b) GPT vs. silicon plasma step number.

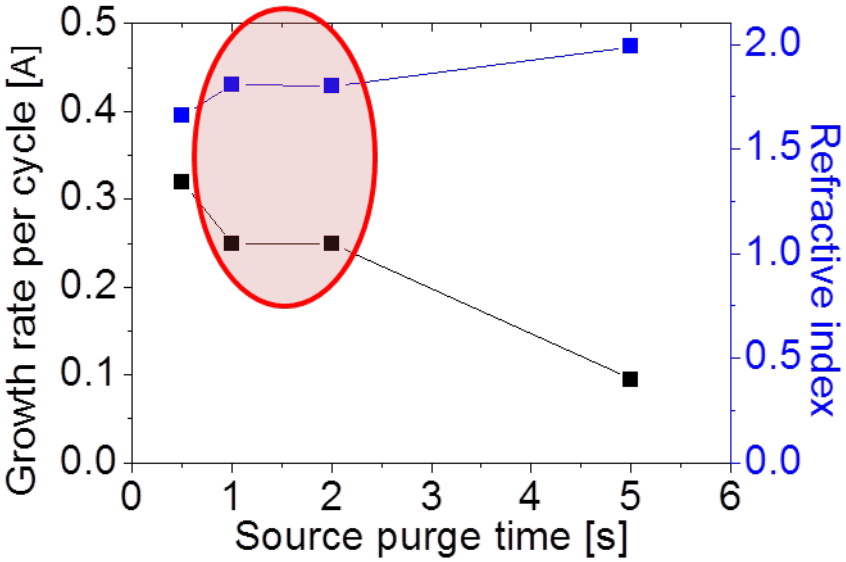

Figure 4.9 Deposition Behavior of SNP Process

With these results of deposition test of three modified processes (SPNP, SPxNP, SNP), each of the process has been optimized in terms of step time conFiguration, plasma power and gas flow rates. The deposition properties of the optimized processes are in Figure 4.10 and Table 4.1. GPC increased by modified process from that of conventional PEALD. As shown in Figure 4.10 and Table 4.1, films deposited by SPNP and SNP processes had refractive index of over 1.8, which means SiO_xN_y close to SiN films are obtained by SPNP and SNP process. On the other hands, films deposited by SP3NP process had lower refractive index close to that of SiO_2, which means that SiO_xN_y close to SiO_2 films are obtained by SP3NP process. The refractive indexes of stoichiometric SiO_2 and Si_3N_4 are 1.46 and 2.05 and that of PECVD-grown silicon nitride is usually from 1.9 to 2.05.[57] The reason of lowering refractive index is considered as an effect of leakage oxygen, which will be discussed in follow section.

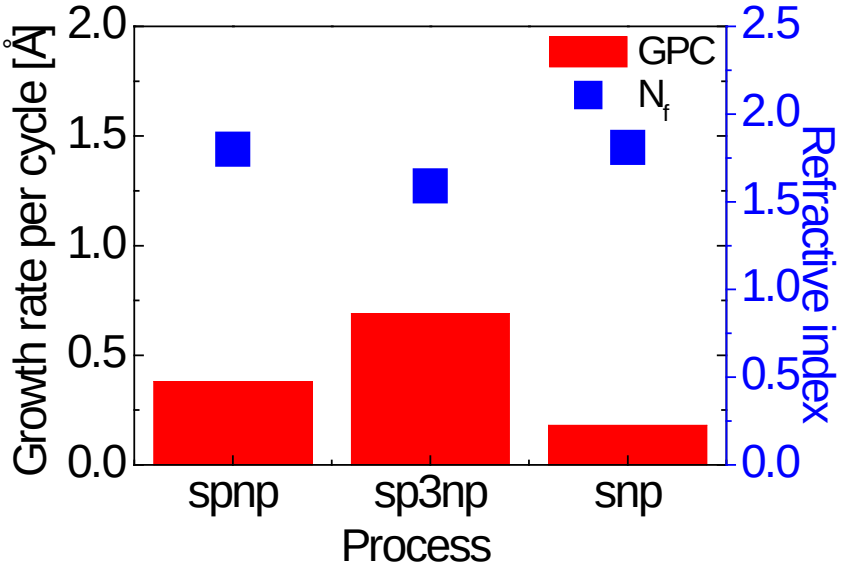

Figure 4.10 The deposition properties of the optimized processes

Process	GPC increased ratio	GPT increased ratio	N_f
SPNP	~4	~ 3.5	1.81
SP3NP	~7	~ 3.9	1.67
SNP	~2.5	~ 3	1.82

Table 4.1 The deposition properties of the optimized processes

4.1.5 Electrical and Chemical Analysis of Silicon Nitride Films with Different Deposition Processes

Figure 4.11 shows the electrical properties of silicon nitride films deposited by three different processes. Figure 4.11(a) shows the normalized capacitance-voltage (C-V) curves of the films with different deposition processes. The C-V hysterics increases as the ratio of silicon plasma over NH_3 plasma increases, which seems to be the result of the fact that that increasing the silicon content of the nitride layer increases the amount of silicon dangling bonds acting as trapping sites.The evidence of higher silicon content will be discussed later. Although this result can leads the idea of SP3NP films for better trap layer, SP3NP films is not decent because of the high interface trap which can be sensible from the slope of the curve. Therefore, SPNP can be considered to have superior C-V property. Figure 4.11(b) shows the CET variation of silicon nitride films as a function of their physical thickness. The dielectric constants of the SPNP film, the SNP film and the SP3NP film were 6.24, 6.35 and 5.70 respectively. The SP3NP film had lower dielectric constant than reported value of PECVD or ALD grown silicon nitride films.[57] It is considered of the effect of high oxygen content of the film, which is the result of the oxidation by chamber leakage oxygen during the silicon source

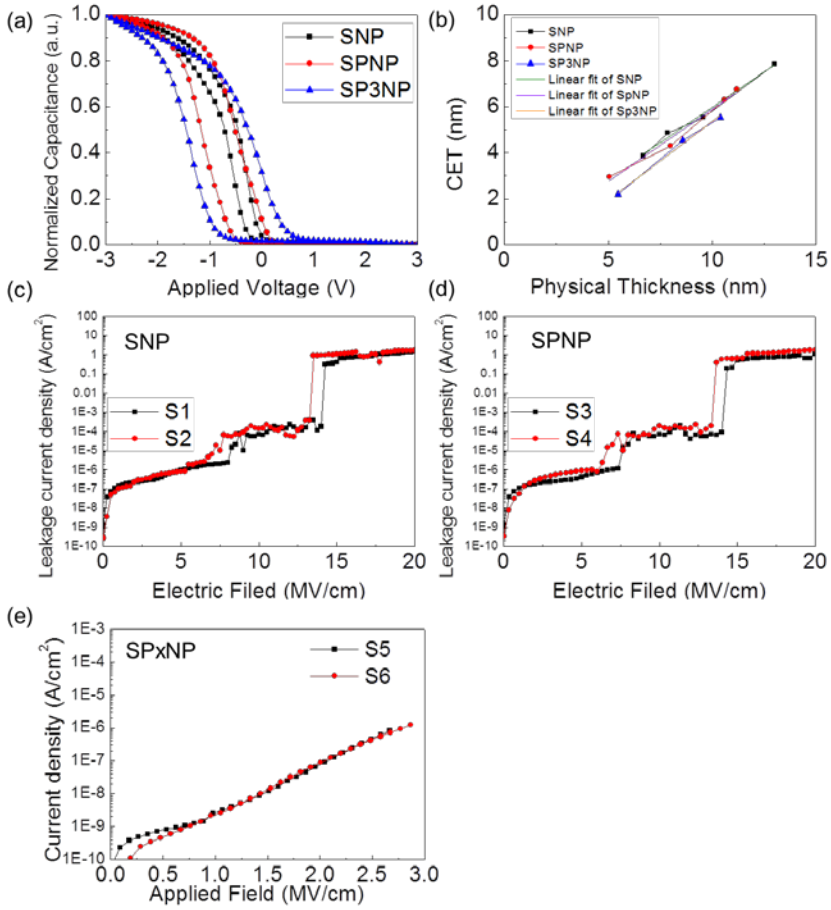

Figure 4.11 The electrical properties of silicon nitride films deposited by three different processes. (a) C-V curves of the films with different deposition processes. (b) CET variation of silicon nitride films as a function of their physical thickness. (c)-(e) The leakage property of the films with SNP, SPNP and SPxNP process, respectively.

plasma step. Figure 4.11(c)-(e) shows the leakage property of the films. SiN_x films deposited by SNP and SPNP process had ~10^{-6} A/cm^2 of leakage current density. On the other hand, the SP3NP film had rapidly increasing current density, which is considered as the effect of higher C content that can be confirmed by follow chemical analyses.

Figure 4.12 shows the Fourier transform infrared (FT-IR) spectroscopy analysis of the silicon nitride films with different deposition processes. The main vibration modes are as follows: N-H stretching at 3340cm^{-1}, N-H_2 scissors at 1550 cm^{-1}, N-H^2 stretching at around 1190 cm^{-1}, Si-O bonds at 1100-1200 cm^{-1}, N-(Si≡)$_3$ bond peak at ~800 $cm^{-1}$and Si-N stretching at around 890 cm^{-1}.[58] As shown in Figure 4.12, the position of Si-N bond peak for the SP3NP film, which represents the coupling of Si-O bonds, was shifted to the higher wavenumber compared to that of the films of SPNP and SNP. The Si-N peaks of SPNP and SNP silicon nitride films were detected at around 890 cm^{-1}, whereas that of SP3NP silicon nitride films was located at around 960 cm^{-1}. Also, the N-(Si≡)$_3$ bond peak at ~800 cm^{-1} of the SP3NP film shows the insufficient nitration, which is because of the incapability of nitridation on the relatively thick silicon layers by the repetition of silicon plasma steps.

Figure 4.13 is the results of AES analysis of the silicon nitride films deposited by SNP, SPNP and SP3NP processes. Because of the

oxidation by exposure to air in days between deposition and AES analysis, the atomic concentration of oxygen for every sample was high at the surface. Therefore, comparison between samples was carried out with the data of the average atomic % of the atoms in the region under the oxidized layers. SP3NP film had ~ 8 atomic % of the carbon content, whereas SPNP and SNP films had very low carbon content which was equal to the noise level of the equipment. Also oxygen content for SP3NP film was high as ~33.28 atomic %. This high carbon and oxygen content seemed to be due to the inability of nitridation for thick layer, deposited by repetition of silicon source plasma, which contained silicon and large amount of carbon and oxygen even with a long NH_3 plasma step of 10 second. The films deposited by SPNP and SNP also had the oxygen content of ~13 atomic %, which is slightly larger than reported value,[59] because of the limitation of the chamber, whose base pressure is high as ~30 mTorr. It would be able to decrease if the leak of the chamber maintained low.

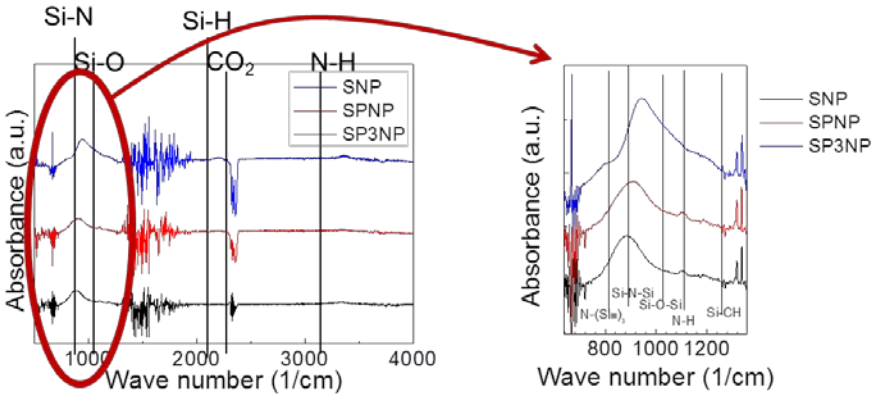

Figure 4.12 FT-IR result of silicon nitride films of SNP, SPNP and SP3NP processes.

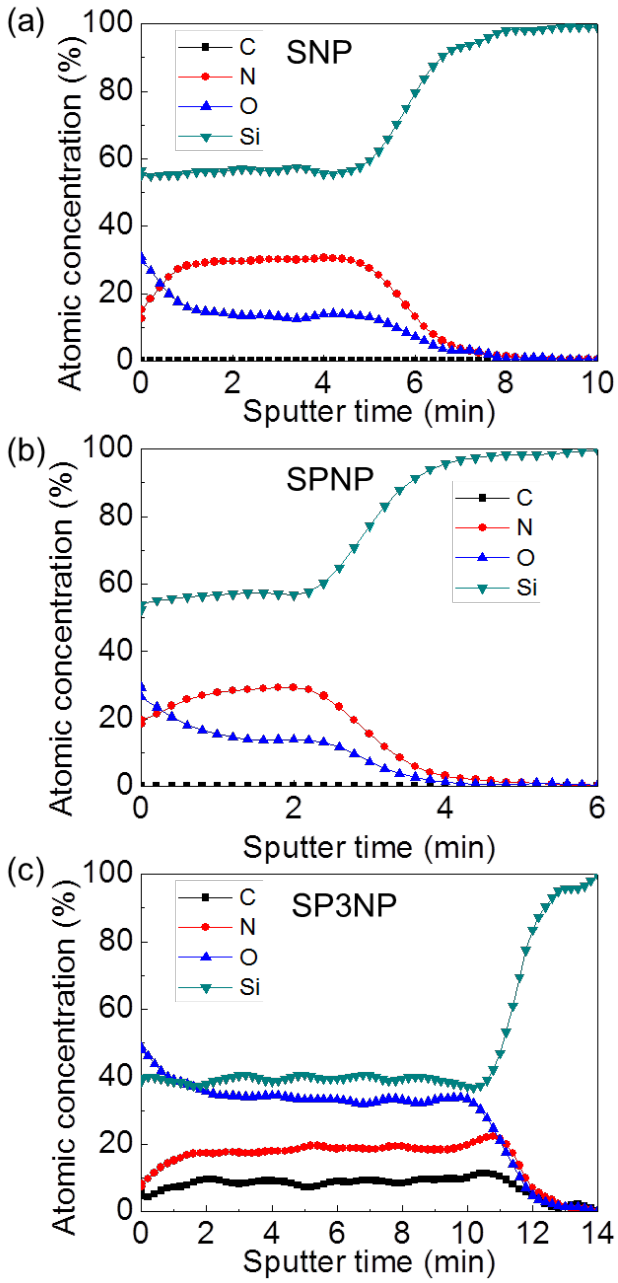

Figure 4.13 AES analysis result of silicon nitride films of (a) SNP, (b) SPNP and (c) SP3NP processes

XPS analysis was performed to obtain chemical composition ofthe films deposited by different processes. Figure 4.14 shows the XPS spectra of (a) Si 2p spectra, (b) N 1s spectra, (c) O 1s spectra and (d) C 1s spectra of the silicon nitride films deposited by SNP, SPNP and SP3NP processes. The analysis was carried out after 2 minutes of argon sputtering because oxygen was incorporated into the silicon nitride film during airexposure due to the oxidation of nonstochiometric silicon-rich nitride film as reported.[60] The position of each peak was corrected relative to the carbon peak of each sample. A Si 2p peak of Si-O bonds was reported to appear at 103.4-103.9eV, and the silicon peak of Si-N bonds is reported to locate at the around 102eV.[61] Also, the silicon peak of Si_x-Si–N_y bonds and O_x–Si–N_y bonds are reported to locate at the around 101eV and 102.8eV, respectively.[62] As shown in Fig. Figure 4.14(a), the peak of SP3NP film was shifted to the higher energy state with the main peak at 102. 6eV and the shift was considered as the results of effect of Si-O bonds. On the other hands, the SPNP and SNP films had main peak around the peak of Si-N bonds. Therefore, oxygen impurities mainly affected the shift of the Si peak position by creating Si-O and Si-N sub-peaks. The N 1s peak of SP3NP also shifted to the higher energy state [Figure 4.14(b)]. The O 1s spectra of SP3NP had Si-O bonds peak at 532.2 while those of SNP and SPNP had lower energy state. These results are understandable with AES data of Fig. 4.20. By separating

the Si 2p peak of Si-N bonds and that of Si-O bonds in Figure 4.14(a), the contribution of sub peaks was obtained as shown in Table 4.2, which showed that the silicon-rich films were formed by SNP and SPNP processes than stoichiometric silicon nitride. Silicon-rich bonds were less formed by SP3NP process because of the formation of silicon oxide films.

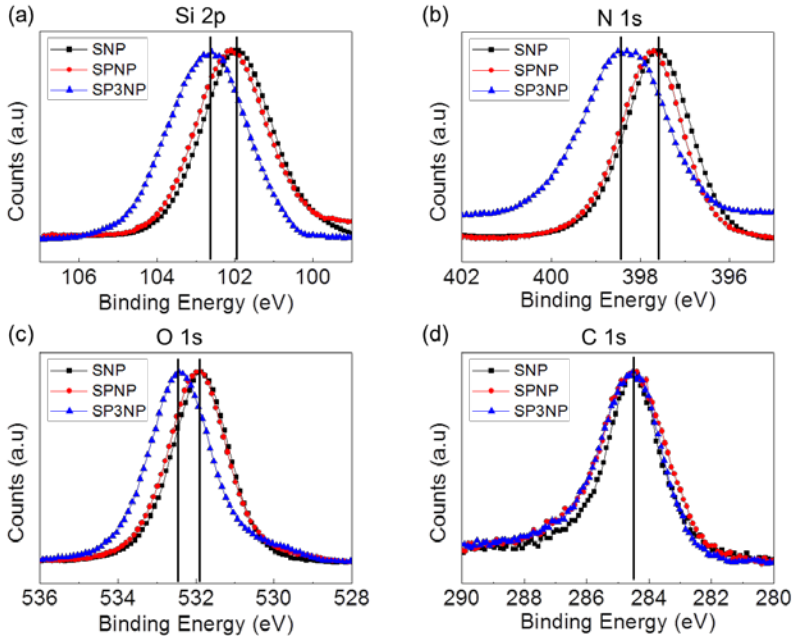

Figure 4.14 XPS data of the SiN films deposited by SNP, SPNP and SP3NP: (a) silicon 2p peak, (b) nitrogen 1s peak, (c) oxygen 1s peak, (d) carbon 1s peak.

Sampls	Peak contribution (%)				Peak energy position	
	$Si–O_4$	$O_x–Si–N_y$	$Si–N_4$	$Si_x–Si–N_y$	$Si_x–Si–N_y$	101.0 eV
SNP	-	24	62	14	$Si–N_4$	102.0 eV
SPNP	-	25	60	16	$O_x–Si–N_y$	102.8 eV
SP3NP	4	55	37	4	$Si–O_4$	103.5 eV

Table 4.2 XPS silicon 2p peaks decomposition.

4.1.6 Charge Trap Layer Properties of SNP and SPNP Silicon Nitride Films

Figure 4.15 shows the schematic diagram ofthe Pt//PEALD-Al_2O_3 /SiN_x by modified process/PEALD-SiO_2/Si multilayer structure for the analysis of the charge trap layer properties of silicon nitride films deposited by SNP and SPNP processes. Because of the high oxygen content and low nitrogen content of the silicon nitride films deposited by the SP3NP process as confirmed in previous sections, SPxNP process were excluded. Oxide and nitiride films were deposited in situ in order. First, 3 nm of silicon oxide was deposited by O_2 plasma and DIPAS. After that, the 5 nm of silicon nitride layers were deposited by the modified PEALD processes. 15 nm-thick blocking oxides were deposited by thermal ALD with TMA and O_3. Platinum were deposited in E-beam evaporator as a gate metal and indium was coated at the side of the samples.

Figure 4.16 shows the demonstrates the capacitance − volatage hysteresis after bidirectional voltage sweeping for devices of (a) only Al_2O_3, (b) oxide-nitride-oxide with SNP silicon nitride film and (c) oxide-nitride-oxide with SPNP silicon nitride film. The counterclockwise hysteresis indicates that electrons are injected into and removed from the silicon nitride film through the silicon / tunnel oxide interface.[63] As the sweeping voltage increased from ±3,±5, ±7 V,

and then to ±10 V, the hysteresis memory window increased up to 2.8 V for the SNP ONO film and 3.4 V for the SPNP ONO film, respectively. On the other hands, negligible memory window was observed for reference Al_2O_3 devices and the window increases significantly for SPNP devices as shown in Figure 4.16(d). This phenomenon suggests that the amorphous SPNP film can be served as the charge-trapping layer.

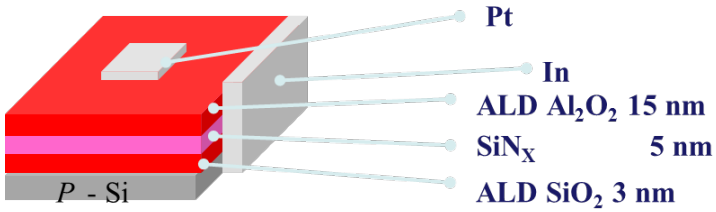

Figure 4.15 Schematic diagram ofthe Pt//PEALD-Al_2O_3 /SiN_x by modified process/PEALD-SiO_2/Si multilayer structure

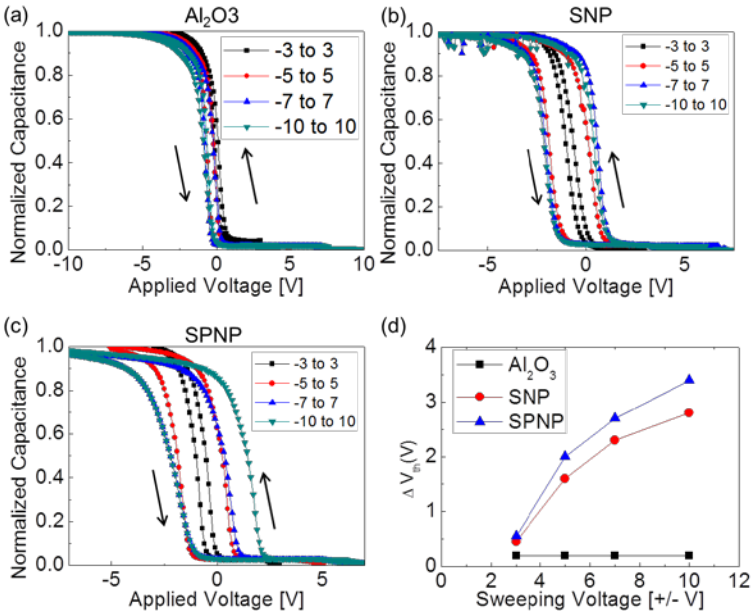

Figure 4.16 C−V hysteresis after bidirectional voltage sweeping for devices of (a) only Al_2O_3, (b) oxide-nitride-oxide with SNP silicon nitride film and (c) oxide-nitride-oxide with SPNP silicon nitride film. (d) C−V hysteresis window for devices with different process.

4.1.7 Step Coverage of the Silicon Nitride Film Deposited by SPNP Process

If step coverage of the silicon nitride films deposited by the SPNP process is not enough, it is not possible to apply the SPNP process to the complex structure. Therefore the step coverage of the silicon nitride film was investigated. Because the interface between the thermal SiO_2 patteren and silicon nitride films deposited by SPNP process due to the fact that both films are armorphours, etched thickness was measured. The silicon nitride films were deposited on the thermal oxide pattern with the depth and width of 2.5 μm and 150 nm. After that, Sb_2Te_3 was deposited by PEALD. The deposited silicon nitride films had ~ 7 times faster wet etch rate in the 1: 100 HF solution than thermal oxides. Therefore, it was possible to confirm roughly the step coverage properties of the silicon nitride film by measuring the etched thickness between the thermal oxide pattern and Sb_2Te_3 pattern. The samples were etched in the HF solution for 10 seconds. Figure 4.17 is the SEM cross section view of the etched sample. Average top thickness was ~31 nm and average side wall thickness at 1.25 μm deep was ~28. Therefore, the SPNP grown silicon nitride films had good step coverage of 90 %. The bottom to top step coverage could not be obtained because of the broken Sb2Te3 pattern at the bottom of the pattern.

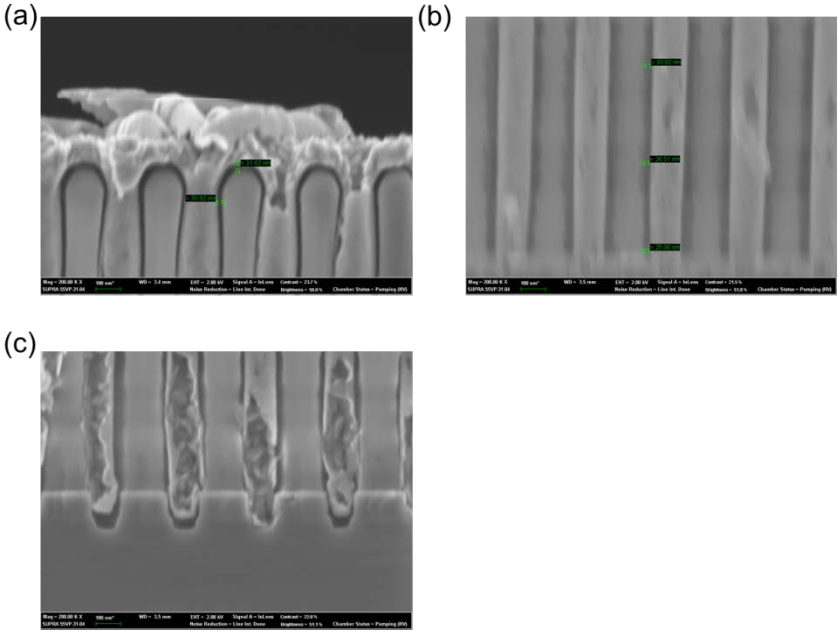

Figure 4.17 SEM image of etched SPNP silicon nitride films on thermal SiO_2 pattern. (a) top (b) side at 1.25 μm and (c) bottom.

4.1.8 Summary

It was hard to deposit silicon nitride films at low temperature by conventional PEALD method due to steric hindrance and high activation energy for adsorptoin of the silicon precursor on Si-N networks. Therefore, modified PEALD processes, which activated silicon precursor by RF plasma, were presented, which were SPNP SPxNP and SNP. By adopting new processes, silicon nitide films were successfully deposited. While films deposited SPxNP process had high oxygen contents films deposited with the optimized condition for SNP and SPNP processes showed that the impurities such as carbon and oxygen were as low as 10 atomic %, and silicon-rich films were formed. This impuritis are expected to decrease if chamber leak condition is superior. Meanwhil, silicon nitirde films by SPNP showd the charge trap layer properties with a hysteresis window of 3.4 V and 90 % of the step coverage. Therefore, SPNP process can be one of solutions for the low temperature silicon nitride deposition.

4.2 Spatial-Type Atomic Layer Deposition of Al_2O_3

4.2.1 Introduction

Atomic layer deposition (ALD) has received considerable attention for its applications to nano-scale thin films fabrication.[45,47] ALD has the inherent ability to achieve sufficient uniformity and step coverage, and enables precise control of film thickness at the atomic level because of its self-limited surface reaction, a unique feature of ALD.[3] In conventional ALD equipment, material layers are grown in a self-limited manner through sequential pulses of the precursor gases and purge out of the physi-sorbed precursors through the operation of valves and pumps in the ALD system. Consequently, conventional ALD systems have several limitations, such as a low growth rate, difficulty in selecting appropriate sources, and high cost of ownership due to the short lifetime of the switching valves and their complicated gas line configuration. These factors make their widespread use unrealistic.

Recently, spatially separated ALD (SALD) has gained interest as a promising solution to these issues.[33] In this type of ALD, various source and purge gases are continuously and simultaneously supplied to the inside of spatially separated areas of the reaction chamber, and the substrates are exposed to the retained gas in sequences by moving

either the reaction chamber or substrates. SALD has three notable advantages over conventional ALD. First, as the respective gases required for deposition are supplied and exhausted continuously and simultaneously, high speed ALD can be achieved as demonstrated by Poodt et al.[34] Second, ALD can be performed in an open system. Levy et al. described the deposition of ZnO thin films in an open system with a similar concept.[41] The other expected advantage of the continuous gas supply is stable pressure in each area of the chamber. When plasma-enhanced atomic layer deposition (PEALD) is used, this can yield a major improvement compared to the conventional pulse/purge ALD equipment. In PEALD using an SALD system, plasma excitation and radicalization are applied to the reaction gases that are continuously supplied, and thus, the plasma can be more stably controlled. Consequently, formation of high-quality thin films is expected. These features may make SALD suitable for several fields in addition to microelectronics, where conventional ALD is already being widely used. For example, SALD could be used for fabricating protective coatings for display devices or solar cells where even the roll-to-roll conFiguration of ALD is being pursued.

Despite the merits of SALD, it is not widely used for mass production due to the difficulty in preventing intermixing reactions between the reaction gases. For the purpose of preventing this intermixing, the distance between the reactor and substrates is

minimized to be on the order of several tens of micrometers. Recent works that described a feasible SALD process were also performed with an extremely narrow distance.[34,41] Maintaining this level of gap through the whole process, however, can be problematic for mass production when the substrate size is large and not flat. A wider gap would be beneficial for machine fabrication and maintenance as long as the facile SALD process could be confirmed. Therefore, in this work we studied SALD with a relatively large gap (5 mm) between the reactor and substrates, considering that this hardware configuration is highly preferred for a mass-production SALD system. In order to examine the feasibility of SALD with such a large gap, a gas flow simulation and Al_2O_3 deposition were performed. After that, the film properties of Al_2O_3 films deposited by SALD, which were faster process than conventional ALD, were compared to that of films grown by conventional ALD.

4.2.2 Deposition Behavior of Spatial Atomic Layer Deposition

In order to perform successful SALD process, reduction of gas mixing is essential. It can be easily achieved when the gap between the substrate and the gas distribution part is slight as few hundreds micrometer but gas has larger chance of mixing in SALD process with a large gap. Therefore, gas mixing and deposition behavior of SALD process should be investigated. Two important factors effecting gas mixing in the rotational type SALD are the gap size and the lateral flow.

Figure 4.18 shows the effect that the gap size between the reactor and the substrates on the lower plate had on the gas mixing for a given pumping speed. In order to estimate the effect of the gap size, changes in growth rate per rotation (GPR) as a function of the rotation speed with a gap size of 10 mm [Figure 4.18(a)] and with a gap size of 5 mm [Figure 4.18(b)] were demonstrated. The GPR for the same sample positions for a gap height of 10mm showed a slightly higher value with a small variation with the rotation speed, which corroborates the incomplete gas isolation. At position C, the GPR is still higher than the normal value, suggesting that the excessive TMA precursor molecules are not sufficiently purged, even for a gap height of 5mm. This indicates that further optimization of SALD reactor design is necessary. However, the GPR for positions M and E was 0.12

nm/rotation, irrespective of the rotation speed when the gap was 5 mm, suggesting successful ALD of Al_2O_3 under this condition.

The deposition data in Figure 4.19, which shows the change in the growth rate per rotation (GPR) as a function of the throttle valve opening ratio, show the results of the deposition test of the effect of the lateral flow on the gas mixing behavior. Deposition was performed with a gap size of 10mm between the walls of the moving parts and the substrates on the lower plate. The throttle valve, which was installed between the SALD chamber and pump, was controlled in order to change the edge pumping rate. Given the fact that the GPR decreases and the uniformity from the center to the edge is improved as the edge pumping rate increases, it is concluded that gas mixing (the leakage of source gas into the purge cell) becomes more severe as the lateral flow weakens. The general decrease in the GPR with increasing throttle valve opening suggests that the efficient purge out of the excessive precursors is achieved when the samples are located in the purge cell. The generally higher GPR near C is due to the higher dose of TMA molecules, which can be explained by the proximity of the injection port to that position for the given relatively uniform purge gas distribution.

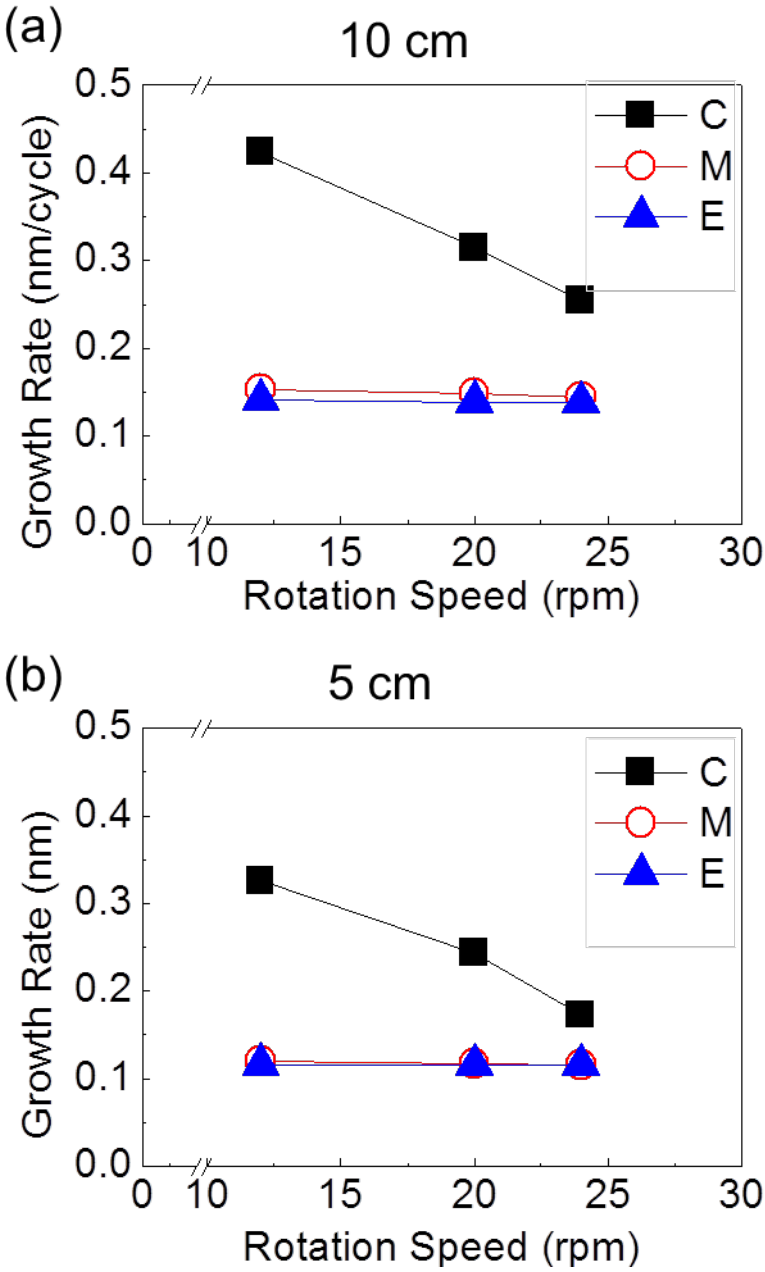

Figure 4.18 Effect of the gap size on gas mixing. (a) Change in GPR as a function of the rotation speed with a gap size of 10 mm. (b) Change in GPR as a function of the rotation speed with a gap size of 5 mm.

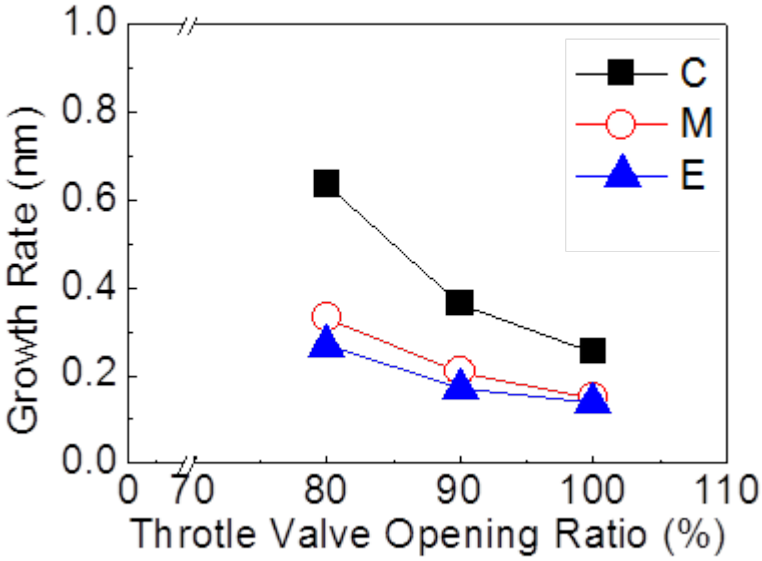

Figure 4.19 Effect of the lateral flow on gas mixing.Change in GPR as a function of the throttle valve opening ratio.

4.2.3 Gas Flow Simulation of Spatial Atomic Layer Deposition

For the interpretation of deposition behaviors of rotational SALD process with a large gap, gas flow simulations for the spatially separated ALD chamber were also conducted with a 3D calculation grid. For the simulations, gas mixing occurred during SALD with alternation of pumping rate, rotational speed, and the gap size between the reactor and substrates. Subsequently, the mole fraction of each gas present during the process was calculated. For simplicity, the baffles at the edge were combined into an edge ring shape space around the lower plate. Also, O_2 (instead of O_2/O_3) was used for the reaction gas and the mass flow rates of the inflow gases, viz. TMA for the source cell, O_2 for the reaction cell, and Ar for the purge cells, were fixed at the same value. The inspected simulated data was obtained from the plane which was 300 lm above the lower plate after three cycles.

To estimate the variation of the gas mixing behavior with the gap size, changes in mole fractions of TMA gas and O_2 as a function of distance from the center of lower plate, was conducted using 3D chamber grids with gap sizes of 10 mm [Figure 4.20(a)] and 5 mm [Figure 4.20(b)] when the rotation speed was 25 rpm. According to Figure 4.19, for the gap height of 10mm, gas mixing and diffusion at the center part becomes severe. This explains the tendency of higher GPC in the position C in Figure 4.18 and Figure 4.19. In addition,

compared to the 10 mm case, the 5 mm case has better isolation, which is the reason why the 5 mm case has better uniformity compared to the 10 mm case in the deposition experiment.

Figure 4.21 shows the results of the simulation of the effect of the lateral flow on the gas mixing behavior. In order to clearly identify variations in the gas mixing behavior related to the edge pumping rates, simulation was performed using a 3D chamber grid constructed with a gap size of 10 mm between the moving walls and the lower plate, which is larger than the usual value of 5 mm. The simulated TMA mole fraction distributions after three rotations with different pumping speeds are shown in Figure 4.21(a) and (b). The edge pumping rate of Figure 4.21(b) was 1.5 times higher than that of Figure 4.21(a). These results indicate that a higher edge pumping rate results in better isolation of the gas species with a stronger lateral flow, and thus more stable SALD. Here, the TMA gas is injected at the port indicated by an arrow in Figure 4.21(a) and (b). Although it was injected into the TMA source cell, the TMA gas diffused into the subsequent purge cell due to gas diffusion through the gap (10 mm). This effect was assisted by the viscous dragging effect from the rotation of the SALD chamber. When the edge pumping speed was high [Fig. 4.4(b)], this diffusion was limited, so the efficient purge out of the physisorbed TMA molecules can be achieved during the half rotation cycle of the purge cell. However, when the edge pumping

speed is low [Fig. 4.4(a)], the whole purge cell is filled (contaminated) with the TMA gas, so efficient purging cannot be expected.

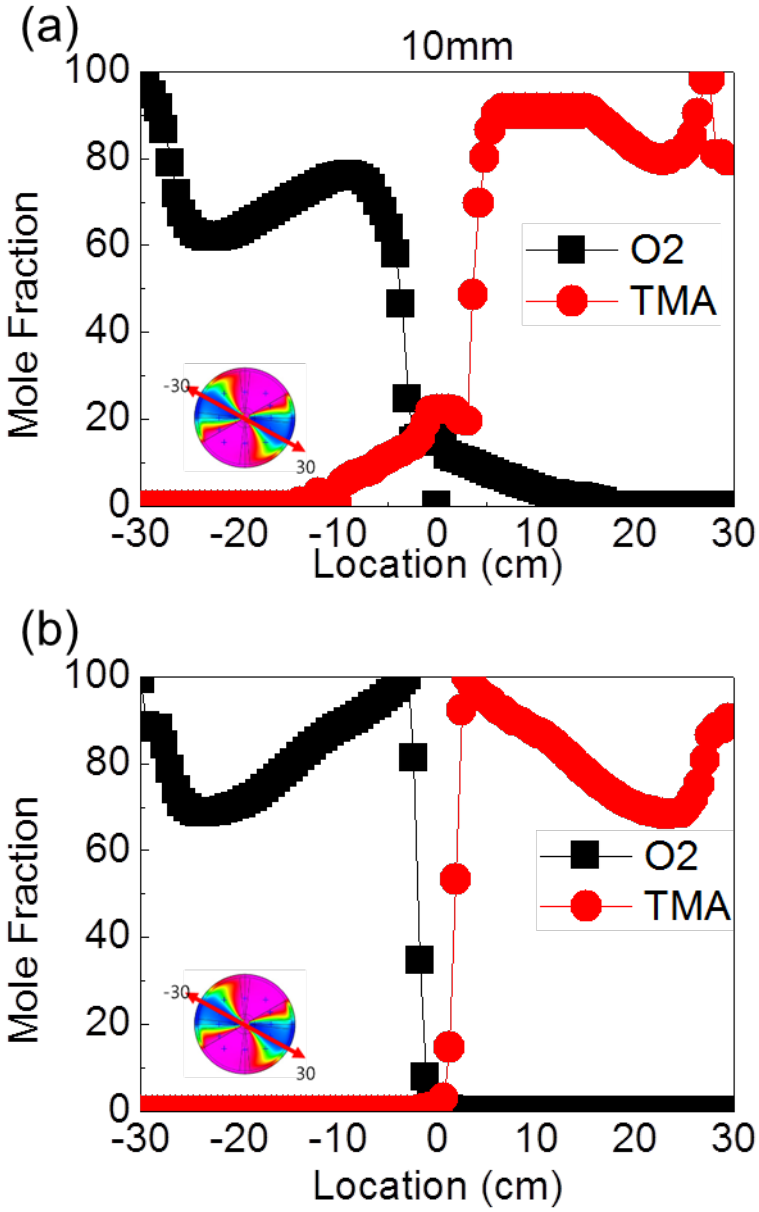

Figure 4.20 Effect of the gap size on gas mixing.Changes in mole fractions of TMA gas and O_2 as a function of distance from the center of lower plate with gap sizes of (a)10mm and (b) 5mm.

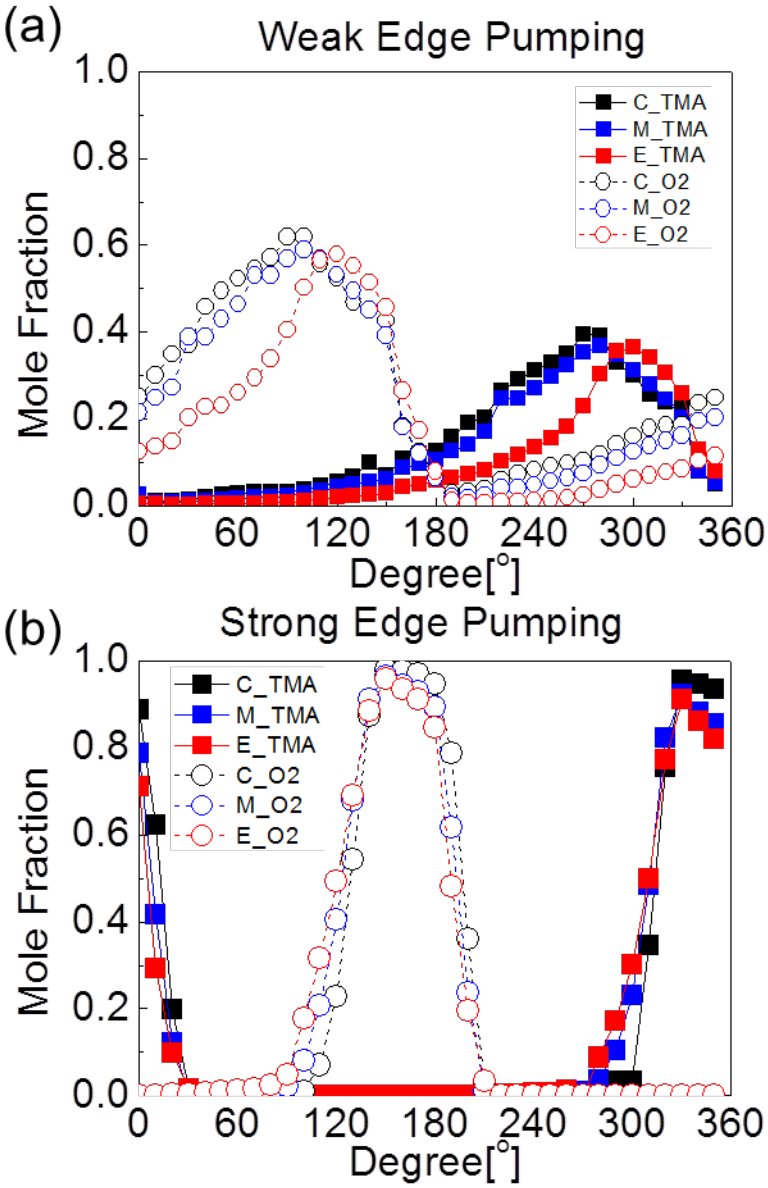

Figure 4.21 Effect of the lateral flow on gas mixing. (a) Simulated distribution of TMA mole fraction with weak edge pumping. (b) Simulated distribution of TMA mole fraction with strong edge pumping.

4.2.4 Deposition Properties of Al_2O_3 Deposited by SALD

As the GPR at positions M and E for a gap size of 5mm is comparable to that of the TMA/O_3 thermal ALD process, it was confirmed that SALD exhibited genuine ALD behavior under these conditions, as shown in Figure 4.22. Figure 4.22(a) shows the variation of the GPR with the amount of TMA injected. In conventional ALD, the saturation curve of the growth rate per cycle as a function of the reactant injection time for a sufficiently long purge time is usually obtained to ensure that the self-limiting reaction occurs. However, in this SALD system, it was not possible to modify the injection time of the TMA alone while keeping the injection times of the other gases the same because the substrate exposure time ratio of the purge gas and reactants was determined by the fixed angles between the partition walls. For this reason, the variation of the GPR with the metering value opening, which changes the amount of TMA injected, was examined to obtain the saturation curve.

In this work, TMA was supplied to the chamber under its own vapor pressure at room temperature and controlled by a metering valve, which was installed between the TMA canister and SALD chamber. As shown in Figure 4.22(a), the GPR saturated at <0.12 nm with increasing levels of TMA injection in the region where the metering valve was 0.5%–2.0% open, when the deposition temperature was 250

^{o}C. This indicates that a selflimiting reaction between the TMA and the surface occurs.

Measurements were also taken of the variations in SALD GPR with the deposition temperature, in order to confirm the ALD window, as shown in Figure 4.22(b). The GPR is 0.14 nm/rotation at 100 ^{o}C and decreases almost linearly with increasing deposition temperature, reaching 0.1 nm/rotation at 300 ^{o}C, which is comparable to conventional thermal ALD using the same source gases.[3,45,47] Puurunen et al. and Elliott et al. reported that the reduction of the reactive sites on the Si substrates with increasing temperature causes a decrease in the growth rate of ALD Al_2O_3 films.[9,45]

In addition, as shown in Figure 4.22(c), the thickness of the film deposited by SALD is linearly proportional to the number of rotations at the deposition temperature of 250 ^{o}C, suggesting that well-behaved steady-state growth is achieved under these conditions. The steady-state growth rate, estimated from the slope of the best linear fitted graph, was 0.117 nm /rotation, which coincides well with the results in Figure 4.22(a) and (b).

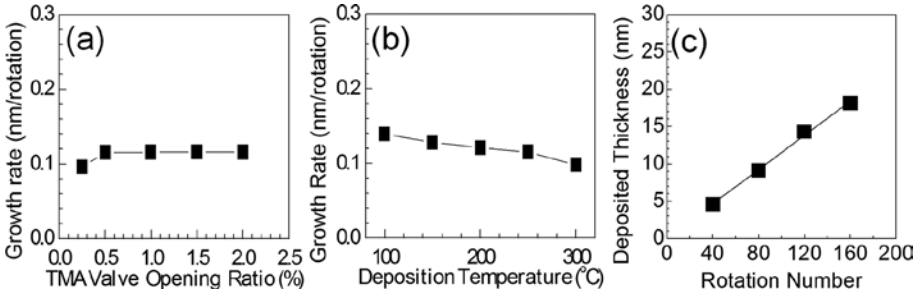

Figure 4.22 Deposition properties of Al_2O_3 deposited by SALD. (a) Change in GPR as a function of the TMA valve opening ratio. (b) Change in the GPR as a function of deposition temperature. (c) Change in the thickness of deposited thin films as a function of cycle number. Data were obtained from sample positioned at M.

4.2.5 Electrical Properties of SALD Al_2O_3

In order to confirm that the characteristics of the SALD Al_2O_3 films are comparable to those of conventional ALD films, the electrical properties of the films deposited by SALD with a gap height of 5mm were examined. Figure 4.23(a) shows the variation in the capacitance equivalent thickness (CET) of the thin films with their physical thickness. From the capacitance–voltage characteristics of the as-deposited SALD-Al_2O_3 thin films for the samples of Figure 4.22 (c) (data not shown), the CET was calculated by applying the following equation:

$$CET = (\varepsilon_0 \varepsilon_r A)/C$$

where ε_0, ε_r, A, and C are the relative dielectric permittivity, vacuum permittivity (= 8.85 × 1014 F/cm), the area of the capacitor and the accumulation capacitance, respectively.

The CET values were obtained from the samples with 40, 80, 120, and 160 rotations. Also, the dielectric constant was acquired from the relationship between the physical thickness and the CET of the films through the following equation:

$$t_{AlO} = (\varepsilon_r/3.9)\ CET$$

where t_{AlO} is the physical thickness of the film. The calculated dielectric constant of the SALD-Al_2O_3 films is 8, which is a reasonable value compared to those previously reported.[48] The

extrapolation of the graph to the y-axis shows an interfacial layer with a CET of 0.39 nm, which may correspond to the CET value of the interfacial alumino-silicate or residual native oxide. In addition, the leakage current of the as-deposited SALD-Al_2O_3 thin films at 40, 80, 120, and 160 rotations, corresponding to the samples shown in Figure 4.22(c), measured by the current density– voltage (J-V) method are plotted in Figure 4.23(b). The results show that the current density (at 1V) of the film at 40 rotations, which has a CET of 3.21 nm, was 9.8×10^{-8} A/cm^2. It is noted that this leakage level is comparable to that reported for the film deposited by conventional ALD.[48]

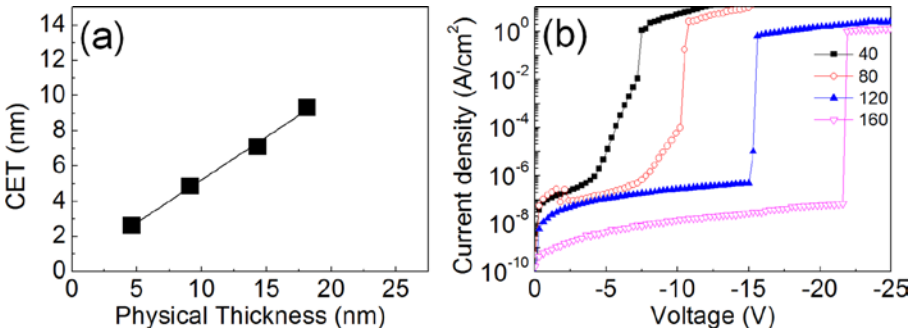

Figure 4.23 (a) Variation in the CET of the SALD Al_2O_3 films with their physical thickness. (b) Leakage current data of SALD Al_2O_3 films of 40, 80, 120, and 160 rotations measured by the Current density-voltage method. Data were obtained from sample positioned at M.

4.2.6 XPS Analysis of SALD Al_2O_3

Figure 4.24(a) and (b) show the Al 2p and O 1s XPS spectra, respectively, for the films grown by SALD at 160 rotations. The positions of both peaks are equivalent to those obtained from the samples grown by conventional ALD. Also, the Al to oxygen ratio (Al/O) of the film at 160 rotations for SALD was calculated from the results and the atomic sensitivity factor (ASF) using the following equation: (peak area of Al 2p/ASF for Al)/(peak area of O 1s/ASF for O). The ASF values for Al 2p and O 1s were 2.93 and 0.537, respectively, and the Al to O ratio obtained was 0.66. This indicates that the stoichiometry of the film deposited by SALD corresponds approximately to Al_2O_3.

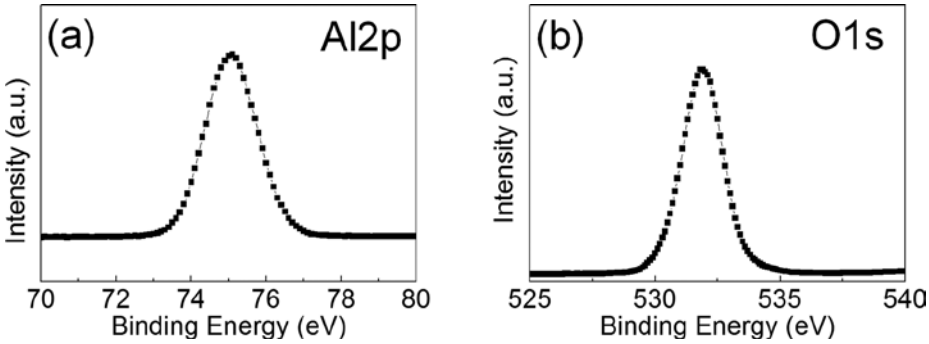

Figure 4.24 XPS spectra for (a) Al 2p and (b) O 1s in the Al_2O_3 film grown by SALD at 160 cycles.

4.2.7 Summary

SALD with a large gap between the reactor and substrates was studied in order to investigate its compatibility with mass production using large area substrates. Gas flow simulations and deposition tests of Al_2O_3 films with TMA and ozone were conducted. According to the simulation data and results of the deposition tests, SALD was successfully achieved when using the strong edge pumping (for strong lateral flows) and a gap height of 5 mm. Also, its ALD behavior was confirmed by inspecting the deposition properties of the SALD-Al_2O_3 thin films. For the comparison with conventional ALD, the effects of the source gas supplied, the deposition temperature, and the number of rotations on the GPR was examined. The GPR was saturated at0.12 nm when the source supply value opening was varied from 0.5%–2.0% at a deposition temperature of 250 ^{o}C. In the deposition temperature range of 100 ^{o}C–300 ^{o}C, the GPR decreased slightly as the temperature was increased. The GPR remained constant as the number of rotations increased. The dielectric constant of the films deposited fast SALD process was 8 and the film with a CET of 3.2 nm had a leakage level of 9.8×10^{8} A/cm^{2} (at 1 V). Also, XPS peak area analysis indicated that the films deposited by fast SALD are composed of Al_2O_3. According to these results, it is believed that fast SALD process with a large gap was successful.

5 CONCLUSIONS

Deposition of silicon nitride films at low temperature by PELAD was investigated. It was hard to deposit silicon nitride films at low temperature by conventional PEALD method due to high activation energy for adsorptoin of the silicon precursor on Si-N networks. Therefore, modified PEALD processes, which activated silicon precursor by RF plasma, were presented, which were SPNP SPxNP and SNP. By adopting new processes, silicon nitide films were successfully deposited. While films deposited SPxNP process had high oxygen contents films deposited with the optimized condition for SNP and SPNP processes showed that the impurities such as carbon and oxygen were as low as 10 atomic %, and silicon-rich films were formed. This impuritis are expected to decrease if chamber leak condition is superior. Meanwhil, silicon nitirde films by SPNP showd the charge trap layer properties with a hysteresis window of 3.4 V and 90 % of the step coverage.

In addition SALD with a large gap between the reactor and substrates was studied in order to investigate its compatibility with mass production using large area substrates. Gas flow simulations and deposition tests of Al_2O_3 films with TMA and ozone were conducted. According to the simulation data and results of the deposition tests,

SALD was successfully achieved when using the strong edge pumping (for strong lateral flows) and a gap height of 5 mm. Also, its ALD behavior was confirmed by inspecting the deposition properties of the SALD-Al_2O_3 thin films. For the comparison with conventional ALD, the effects of the source gas supplied, the deposition temperature, and the number of rotations on the GPR was examined. The GPR was saturated at0.12 nm when the source supply value opening was varied from 0.5%–2.0% at a deposition temperature of 250 ^{o}C. In the deposition temperature range of 100 ^{o}C–300 ^{o}C, the GPR decreased slightly as the temperature was increased. The GPR remained constant as the number of rotations increased. The dielectric constant of the films deposited by faster SALD process than conventional ALD process was 8 and the film with a CET of 3.2 nm had a leakage level of 9.8×10^{8} A/cm^{2} (at 1 V). Also, XPS peak area analysis indicated that the films deposited by SALD are composed of Al_2O_3.

In conclusion, SPNP process using silicon source plasma can be one of solutions for the low temperature silicon nitride deposition. According to these results, it is believed that SALD with a large gap was successfully achieved and Al_2O_3 films was successfully deposited with a fast SALD process. Therefore, the proposed deposition

processes for the charge trap layer and blocking oxide for 3D structure devices were successfully developed.

6 REFERENCE

[1] Hideo Hosono, Journal of non-crystalline solids **352** (9), 851 (2006).

[2] Madambi K Jayaraj, Kachirayil J Saji, Kenji Nomura, Toshio Kamiya, and Hideo Hosono, Journal of Vacuum Science & Technology B **26** (2), 495 (2008).

[3] Seong Keun Kim, Suk Woo Lee, Cheol Seong Hwang, Yo-Sep Min, Jeong Yeon Won, and Jaehack Jeong, Journal of the Electrochemical Society **153** (5), F69 (2006).

[4] Booyong S Lim, Antti Rahtu, and Roy G Gordon, Nature materials **2** (11), 749 (2003).

[5] Ville Miikkulainen, Markku Leskelä, Mikko Ritala, and Riikka L Puurunen, Journal of applied physics **113** (2), 021301 (2013).

[6] Steven M George, Chemical Reviews **110** (1), 111 (2009).

[7] Tuomo Suntola, Materials Science Reports **4** (5), 261 (1989).

[8] M. Leskelä and M. Ritala, Thin Solid Films **409** (1), 138 (2002).

[9] Riikka L Puurunen, Journal of applied physics **97** (12), 121301 (2005).

[10] P.W. Atkins, Physical Chemistry, 6th edition, Oxford University Press, pp 857-866 (1998)

[11] MA Alam and ML Green, Journal of applied physics **94** (5), 3403

(2003).

[12] Hyung-Sang Park, Jae-Sik Min, Jung-Wook Lim, and Sang-Won Kang, Applied Surface Science **158** (1), 81 (2000).

[13] M. Ritala, M. Leskelä, and E. Rauhala, Chem. Mater. 6, 556 (1994)

[14] M. Ritala, M. Leskelä, L. Niinistö, and P. Haussalo, Chem. Mater. 5, 1174 (1993)

[15] S. A. Morozov, A. A. Malkov, and A. A. Malygin,[Russ. J. Appl. Chem. 76, 7 (2003)].

[16] Markku Ylilammi, Thin Solid Films **279** (1), 124 (1996).

[17] Riikka L Puurunen, Chemical Vapor Deposition **9** (6), 327 (2003).

[18] H. B. Profijt, S. E. Potts, M. C. M. van de Sanden, and W. M. M. Kessels, Journal of Vacuum Science & Technology A **29** (5) (2011).

[19] Hyungjun Kim, Thin Solid Films **519** (20), 6639 (2011).

[20] Liqi Wu and Eric Eisenbraun, Journal of Vacuum Science & Technology B **25** (6), 2581 (2007); Nicole E Lay, Gregory A Ten Eyck, David J Duquette, and Toh-Ming Lu, Electrochemical and solid-state letters **10** (1), D13 (2007); Trinh T. Van and Jane P. Chang, Applied Surface Science **246** (1–3), 250 (2005).

[21] Jung Wook Lim, Jae Bon Koo, Sun Jin Yun, and Hyun-Tak Kim, Electrochemical and solid-state letters **10** (10), J136 (2007); Sun Jin Yun, Young-Wook Ko, and Jung Wook Lim, Applied Physics Letters **85** (21), 4896 (2004).

[22] M.A. Lieberman and A.J. Lichtenberg, *Principles of Plasma*

Discharges and Materials Processing. (Wiley, 2005).

[23] Sug Hun Hong, Jae Hyuck Jang, Tae Joo Park, Doo Seok Jeong, Miyoung Kim, Cheol Seong Hwang, and Jeong Yeon Won, Applied Physics Letters **87** (15), 152106 (2005).

[24] Jong-Ho Yang, Jae-Eun Park, Joo-Won Lee, Kang-Soo Chu, Ja-Hum Ku, Moon-Han Park, Nae-In Lee, Hee-Sung Kang, Myung-Hwan Oh, and Jun-Ha Lee, presented at the VLSI Technology, 2003. Digest of Technical Papers. 2003 Symposium on, 2003 (unpublished).

[25] Anri Nakajima, Quazi D. M. Khosru, Takashi Yoshimoto, and Shin Yokoyama, Microelectronics Reliability **42** (12), 1823 (2002); Anri Nakajima, Takashi Yoshimoto, Toshirou Kidera, and Shin Yokoyama, Applied Physics Letters **79** (5), 665 (2001).

[26] Shin Yokoyama, Hiroshi Goto, Takahiro Miyamoto, Norihiko Ikeda, and Kentaro Shibahara, Applied Surface Science **112**, 75 (1997).

[27] Hiroshi Goto, Kentaro Shibahara, and Shin Yokoyama, Applied Physics Letters **68** (23), 3257 (1996).

[28] HCM Knoops, E Langereis, MCM van de Sanden, and WMM Kessels, Journal of the Electrochemical Society **157** (12), G241 (2010).

[29] Tatsunori Murata, Yoshihiro Miyagawa, Yukio Nishida, Yoshiki Yamamoto, Tomohiro Yamashita, Masazumi Matsuura, Koyu Asai, and Hiroshi Miyatake, Japanese Journal of Applied Physics **49** (4S), 04DB11 (2010).

[30] Y. Nakashima and K. Ooba S. Yokoyama, Journal of Korean

Physical Society **35**, 71 (1999).

[31] Collin Mui, Yuniarto Widjaja, Jeung Ku Kang, and Charles B Musgrave, Surface Science **557** (1), 159 (2004).

[32] HB Profijt, SE Potts, MCM Van De Sanden, and WMM Kessels, Journal of Vacuum Science & Technology A **29** (5), 050801 (2011).

[33] P. Poodt, D.C. Cameron, E. Dickey, S.M. George, V. Kuznetsov, G.N. Parsons, F. Roozeboom, G. Sundaram, and A. Vermeer, Journal of Vacuum Science & Technology A: Vacuum, Surfaces, and Films **30** (1), 010802 (2012).

[34] Paul Poodt, Adriaan Lankhorst, Fred Roozeboom, Karel Spee, Diederik Maas, and Ad Vermeer, Advanced Materials **22** (32), 3564 (2010).

[35] Roy G Gordon, Dennis Hausmann, Esther Kim, and Joseph Shepard, Chemical Vapor Deposition **9** (2), 73 (2003).

[36] Sungin Suh, Sanghyun Park, Hajin Lim, Yu-Jin Choi, Cheol Seong Hwang, Hyeong Joon Kim, and Seok-Jun Won, Journal of Vacuum Science & Technology A **30** (5), 051504 (2012).

[37] Sven G Lindfors, Arto J Pakkala, and Tuomo S Suntola, (Google Patents, 1983).

[38] Jorma Antson and Tuomo Suntola, (Google Patents, 1977).

[39] Eric Dickey and William A. Barrow, Journal of Vacuum Science & Technology A **30** (2) (2012).

[40] PS Maydannik, TO Kääriäinen, and DC Cameron, Chemical Engineering Journal **171** (1), 345 (2011).

[41] David H Levy, Shelby F Nelson, and Diane Freeman, Journal of Display Technology **5** (12), 484 (2009).

[42] P Poodt, A Illiberi, and F Roozeboom, Thin Solid Films **532**, 22 (2013).

[43] L Hennen, EHA Granneman, and WMM Kessels, presented at the Photovoltaic Specialists Conference (PVSC), 2012 38th IEEE, 2012 (unpublished).

[44] AC Dillon, AW Ott, JD Way, and SM George, Surface Science **322** (1), 230 (1995); AW Ott, JW Klaus, JM Johnson, and SM George, Thin Solid Films **292** (1), 135 (1997); AW Ott, KC McCarley, JW Klaus, JD Way, and SM George, Applied Surface Science **107**, 128 (1996).

[45] SD Elliott, G Scarel, C Wiemer, M Fanciulli, and G Pavia, Chemistry of materials **18** (16), 3764 (2006).

[46] E Ghiraldelli, C Pelosi, E Gombia, G Chiavarotti, and L Vanzetti, Thin Solid Films **517** (1), 434 (2008); Elisa Ghiraldelli, Claudio Pelosi, Enos Gombia, Cesare Frigeri, Lia Vanzetti, and Sevda Abdullayeva, Japanese Journal of Applied Physics **47** (10S), 8174 (2008); David N Goldstein, Jarod A McCormick, and Steven M George, The Journal of Physical Chemistry C **112** (49), 19530 (2008); JL Van Hemmen, SBS Heil, JH Klootwijk, Fred Roozeboom, CJ Hodson, MCM Van de Sanden, and WMM Kessels, Journal of the Electrochemical Society **154** (7), G165 (2007); Xiao-Hong Zhang, Benoit Domercq, Xudong Wang, Seunghyup Yoo, Takeshi Kondo, Zhong Lin Wang, and Bernard Kippelen, Organic

Electronics **8** (6), 718 (2007).

[47] Jaebum Kim, Kuntal Chakrabarti, Jinho Lee, Ki-Young Oh, and Chongmu Lee, Materials chemistry and physics **78** (3), 733 (2003).

[48] Seong Keun Kim and Cheol Seong Hwang, Journal of applied physics **96** (4), 2323 (2004).

[49] Jusung Engineering, Korea (5 August 2008 2008).

[50] S.M. George, Polymer **1550**, 125 (2010); SBS Heil, JL Van Hemmen, MCM Van de Sanden, and WMM Kessels, Journal of applied physics **103** (10), 103302 (2008); Tai-Peng Lee, Chuck Jang, Barbara Haselden, Mark Dong, Seung Park, Lawrence Bartholomew, Hood Chatham, and Yoshihide Senzaki, Journal of Vacuum Science & Technology B **22** (5), 2295 (2004).

[51] Jacob W. Smith, Sean M. Seutter, and R. Suryanaryanan Iyer, Journal of Vacuum Science & Technology B **23** (6), 2340 (2005).

[52] B Reynes and JC Bruyère, Sensors and Actuators A: Physical **33** (1), 25 (1992).

[53] Sean King, Rosalie Chu, Guanghai Xu, and Jennifer Huening, Thin Solid Films **518** (17), 4898 (2010); WAP Claassen, Plasma chemistry and plasma processing **7** (1), 109 (1987).

[54] Y Manabe and T Mitsuyu, Journal of applied physics **66** (6), 2475 (1989).

[55] Shin Yokoyama, Norihiko Ikeda, Kouji Kajikawa, and Yoshimitsu Nakashima, Applied Surface Science **130**, 352 (1998).

[56] Tae-Kwang Eom, Soo-Hyun Kim, Kye-Sun Park, Sunjung Kim, and Hoon Kim, Electrochemical and solid-state letters **14** (1), D10 (2011).

[57] Sean W King, Journal of Vacuum Science & Technology A **29** (4), 041501 (2011).

[58] M Klanjšek Gunde and Marijan Maček, Physica status solidi (a) **183** (2), 439 (2001).

[59] Kwangchol Park, Won-Deok Yun, Byoung-Jun Choi, Heon-Do Kim, Won-Jun Lee, Sa-Kyun Rha, and Chong Ook Park, Thin Solid Films **517** (14), 3975 (2009).

[60] Shunsuke Morishita, Satoshi Sugahara, and Masakiyo Matsumura, Applied Surface Science **112**, 198 (1997).

[61] R Kärcher, L Ley, and RL Johnson, Physical Review B **30** (4), 1896 (1984); Mayumi Kazuta, Noriko So, Hideaki Kasamura, and Masahiro Kudo, Surface and interface analysis **19** (1-12), 222 (1992).

[62] J Dupuis, E Fourmond, D Ballutaud, N Bererd, and M Lemiti, Thin Solid Films **519** (4), 1325 (2010).

[63] D. N. Kouvatsos, V. Ioannou-Sougleridis, and A. G. Nassiopoulou, Applied Physics Letters **82** (3), 397 (2003); Yung-Hsien Wu, Chia-Lin Ku, and Jiun-Fang Wang, Journal of the Electrochemical Society **151** (1), F1 (2004).

LIST OF PUBLICATIONS

1. Refereed Journal Articles (SCI)

1.1. International

1. Seok-Jun Won, **SunginSuh**, Sang Woon Lee, Gyu-Jin Choi, CheolSeong Hwang and HyeongJoon Kim, "Substrate Dependent Growth Rate of Plasma-Enhanced Atomic Layer Deposition of Titanium Oxide Using N2O Gas", Electrochemical and Solid-State Letters, 13 2 G13-G16 (2010)
2. Seok-Jun Won, MyungSoo Huh, Sanghyun Park, **SunginSuh**, Tae Joo Park, Jeong Hwan Kim, CheolSeong Hwang, and HyeongJoon Kim, "Capacitance and Interface Analysis of Transparent Analog Capacitor Using Indium Tin Oxide Electrodes and High-k Dielectrics", Journal of The Electrochemical Society, 157, G170-175 (2010)
3. Seok-Jun Won, **SunginSuh**, MyungSoo Huh, and HyeongJoon Kim, "High-Quality Low-Temperature Silicon Oxide by Plasma-Enhanced Atomic Layer Deposition Using a Metal–Organic Silicon Precursor and Oxygen Radical", IEEE Electron Device Letter, Vol.31, No.8 (2010)
4. Seok-Jun Won, Joon Rae Kim, **SunginSuh**, Nae-In Lee, CheolSeong Hwang, and HyeongJoon Kim, "Effect of Catalyst Layer Density and Growth Temperature in Rapid Atomic Layer Deposition of Silica Using Tris(tert-pentoxy)silanol", ACS Appl. Mater. Interfaces, 3, 1633–1639 (2011)
5. Seok-Jun Won, Joon Rae Kim, **SunginSuh**, Yu Jin Choi and HyeongJoon Kim,

"Zirconium-assisted reaction in low temperature atomic layer deposition using Bis(ethyl-methyl-amino)silane and water", Applied Surface Science Volume 257, Issue 23 (2011)

6. Seok-Jun Won, Hyung-Suk Jung, **SunginSuh**, Yu Jin Choi, Nae-In Lee, CheolSeong Hwang, and HyeongJoon Kim "Growth and electrical properties of silicon oxide grown by atomic layerdeposition using Bis(ethyl-methyl-amino)silane and ozone", J. Vac. Sci. Technol. A, Vol 30, No. 1 (2011)
7. **SunginSuh**, Sanghyun Park, Hajin Lim, Yu-Jin Choi, CheolSeong Hwang, and HyeongJoon Kim, "Investigation on spatially separated atomic layer deposition by gas flow simulation and depositing Al_2O_3 films", J. Vac. Sci. Technol. A 30(5), (2012)
8. Joon Rae Kim, Hajin Lim, Sanghyun Park, Yu Jin Choi, **SunginSuh**, Bong Seob Yang, JaeyeongHeo, and HyeongJoon Kim, "Effects of Tris(tert-pentoxy)silanol Purge Time on SiO2 Thin-Film Growth Rate in Rapid Atomic Layer Deposition", ECS Solid State Letters, 2 (10) P91-P93 (2013)
9. Jong-Sik Choi, Bong Seob Yang, Seok-Jun Won, Jun Rae Kim, **SunginSuh**, Hui Kyung Park, JaeyeongHeo, and HyeongJoon Kim, "Low Temperature Formation of Silicon Oxide Thin Films by Atomic Layer Deposition Using NH3/O2 Plasma",ECS Solid State Letters, 2 (12) , P114-P116 (2013)

2. CONFERENCES

2.1 Domestic

1. 서성인, 원석준, 최유진, 박상현, 김형준, “Al_2O_3 박막 증착과 시뮬레이션을 통한 공간분할 방식 원자층증착법의증착 거동 연구”한국반도체디스플레이기술학회2011년춘계학술대회, 2011. 6. 2, 서울대학교엔지니어링하우스
2. 김준래, 원석준, 서성인, 김형준, "Effect of Catalyst Layer Density and Growth Temperature in Rapid Atomic Layer Deposition of Silica Using Tris(tert-pentoxy)silanol", 한국 반도체 디스플레이 기술학회 2011년 추계 심포지움, 2011년 10월 13일, 경기도 고양시 킨텍스(KINTEX)
3. 서성인, 원석준, 최유진, 박상현, and 김형준, "Investigation on spatially separated atomic layer deposition with a large gap by depositing Al_2O_3 thin films and simulation", 한국 반도체 디스플레이 기술학회 2012년 춘계 학술대회 및 제2회 반디 제주포럼, 18th may 2012, 제주대학교국제교류회관
4. 최유진, 원석준, 정형석, 서성인, 박상현, and 김형준, "Effect of oxygen source on film properties of atomic layer deposited La-silicate film", 한국반도체디스플레이기술학회 2012년 춘계 학술대회 및 제2회반 디제주포럼, 18th may 2012, 제주대학교국제교류회관
5. 김준래, 원석준, 임하진, 박상현, 서성인, 김형준, "고속 원자층증착법을 이용한 실리콘산화막 증착 속도 향상을 위한 공정연구" 한국반도체디스플레이기술학회 2012년 추계 학술대회, 10 October, 2012, 킨텍스(KINTEX), 일산

6. 서성인, 원석준, 최유진, 박상현, 김형준, "Al2O3박막증착과 기체유동 시뮬레이션을 통한 대간격 공간분할방식 원자층 증착법의 연구"한국반도체디스플레이기술학회 2012년 추계 학술대회, 10 October, 2012, 킨텍스(KINTEX), 일산
7. 최유진, 정형석, 임하진, 서성인, 김준래, 김형준, "Ge 기판을 이용한 원자층증착법을 통한 La-silicate 막의 전기적 특성" 한국반도체디스플레이기술학회 2012년추계학술대회, 10 October, 2012, 킨텍스(KINTEX), 일산
8. 김성경, 서성인, 이훈희, 박상현, 김형준, "HTCVD 기술개선을위한 SiC 증착 시뮬레이션" 한국 반도체 디스플레이 기술학회 2013년 춘계 학술대회 및 제1회 SiC 전력반도체심포지움, 31 May, 2013, 한국교원단체총연합회관 2층단재실, 서울
9. 김준래, 임하진, 박상현, 최유진, 서성인, 허재영, 김형준, "고속 원자층증착법을 이용한 실리콘 산화막 증착에서의 Tris(tert-pentoxy)silanol purge time의영향" 한국 반도체 디스플레이 기술학회 2013년 추계 학술대회 및 제4회 반도체 공정 포럼 반도체 차세대 공정장비 기술 심포지엄23 October, 2013, 한국반도체산업협회, 분당
10. 서성인, 김준래, 최유진, 임하진, 김형준, "변형된 플라즈마 원자층증착법을 통한 저온 SiN 박막증착" 한국 반도체 디스플레이 기술학회 2013년 추계 학술대회 및 제4회 반도체 공정 포럼 반도체 차세대 공정장비 기술 심포지엄 23 October, 2013, 한국반도체산업협회, 분당

11. 최유진, 임하진, 이수형, 서성인, 김준래, 박상현, 김형준, "Ge 기판을 이용한 원자층증착법을 통한 La-silicate 막의 전기적특성" 한국 반도체 디스플레이 기술학회 2013년 추계 학술대회 및 제4회 반도체 공정 포럼 반도체 차세대 공정 장비 기술 심포지엄23 October, 2013, 한국 반도체산업협회, 분당

2.2 International

1. Seok-Jun Won, **SunginSuh**, MyungSoo Huh, Yu Jin Choi, and HyeongJoon Kim, “Growth Behaviors and Electrical Properties of Silicon Oxide in Atomic Layer Deposition Using Bis(ethyl-methyl-amino)silane”Society of Vacuum Coaters, April, 2010
2. Seok-Jun Won, Yu Jin Choi, **SunginSuh**, and HyeongJoon Kim, “The Effect of Catalyst Layer Density on Rapid Atomic Layer Deposition Using Tris(tert-pentoxy)silanol”10th International Conderence on Atomic Layer Deposition, June, 2010
3. **SunginSuh**, Seok-Jun Won, and HyeongJoon Kim, “Deposition and Electrical Properties of Aluminum Oxide Thin Films by Space-Divided Atomic Layer Deposition”The 7th AMF-AMEC, June 28- July 1, 2010
4. Sanghyun. Park, JiWoon Park, **SunginSuh**, Yu Jin Choi, SeokJun Won, and HyeongJoon Kim, “A growth of silica nanowires by adding O3 for non-heterolepticris(ethylmethyl-amino)silane precursor”The 7th AMF-AMEC, June 28- July 1, 2010

5. Seok-Jun Won, **SunginSuh**, CheolSeong Hwang, and HyeongJoon Kim, “Substrate Dependency of Thin Film Growth Rate in Plasma-Enhanced Atomic Layer Deposition of Titanium Oxide using N2O as Oxygen Source:”The 7th AMF-AMEC, June 28- July 1, 2010
6. Yu Jin Choi, Seok-Jun Won, Hyung-Suk Jung, **SunginSuh**, HyeongJoon Kim, “Electrical and Chemical Properties of Lanthanum Silicate Films Deposited by Atomic Layer Deposition with Liquid Delivery System”IUMRS-ICEM 2010
7. **SunginSuh**, Seok-Jun Won, Yu Jin Choi, and HyeongJoon Kim, “Characterization of Space-Divided Atomic Laer Deposition by Depositing Aluminum Oxide Thin Films and Simulation”2011 MRS Spring Meeting, 25-29 April 2011, San Francisco, CA USA.
8. **SunginSuh**, Seok-Jun Won, Sanghyun Park, Hajin Lim, Yujin Choi and HyeongJoon Kim, "Deposition of Al_2O_3 Films by Spatially Separated Atomic Layer Deposition with a Large Gap Distance"AVS-ALD & Baltic ALD2012 (ALD 2012), June 17-20, 2012, Dresden, Germany

ABSTRACT (IN KOREAN)

최근 들어 3차원 구조가 다음 세대의 소자로 주목을 받고 있다. 그런데 3차원 구조 소자 제작을 하기 위해서는 amorphous oxide semiconductor (AOS)와 같이 넓은 밴드 갭 및 상대적으로 높은 모빌리티 그리고 무엇보다도 쉽게 증착이 가능한 막이 channel layer로 사용되어야한다. 그런데 Zinc Tin Oxide 등의 AOS는 450℃ 이상에서 여러 형태의 결정상을 가지기 때문에, 그 위의 gate dielectric layer 이나 trap layer는 400℃ 이하에서 증착이 되어야 한다.

Silicon nitride의 경우 주로 600℃ 정도의 높은 공정온도에서 chemical vapor deposition (CVD) 혹은 Plasma Enhanced CVD (PECVD) 방식을 통하여 증착이 되어왔으며, 낮은 온도에서 증착된 PECVD SiN 막의 경우 일반적으로 높은 수소 concentration을 갖고 있어 한계가 있어 왔다. 따라서 Plasma Enhanced Atomic Layer Deposition (PEALD) 방법을 통하여 상대적으로 낮은 온도에서 좋은 step coverage를 갖는 stoichiometric 한 막을 얻을 수 있으므로 이러한 한계를 극복하기 위하여 적용 될 수 있다.

이 연구에서는 저온에서 charge trap layer로서의 silicon nitride 박막 증착을 하기 위하여 SiO_2 박막 증착 시 많이 사용되어온 유기 Ligand를 갖는 Silicon 전구체들을 이용하여 일반적인 PEALD 공정 및 변형된 PEALD 공정으로 350℃ 이하에서 SiN 증착을 시도하였다. 일반적인 PEALD 공정으로는 증착 속도가 너무 낮았기 때문에 실리콘 전구체 흡착 시 플라즈마를 여기시키는 방식의 새로운 공정 (SPNP, SPxNP, SNP)를

개발하여 증착을 하였다. 이에 따라 300 ℃에서 ~1.8의 굴절률을 갖는 박막을 일반적인 PEALD 공정 대비 ~4배의 높은 증착속도로 증착할 수 있었으며, 증착한 박막의 dielectric constant는 ~6.2 정도였다. FT-IR, XPS 및 AES 분석결과 SPxNP 공정으로 증착한 박막이 산소를 많이 포함한 반면, SNP와 SPNP 공정으로 증착한 박막의 경우 탄소와 산소 등의 불순물이 약 10% 정도로 낮았으며 silicon-rich 한 막을 얻을 수 있었다. 또한 TMA/O_3 를 이용한 Al_2O_3 박막을 blocking layer (15nm) 로, PEALD SiO_2를 tunneling oxide (3nm) 로 사용하고 SPNP 및 SNP 공정으로 silicon nitride 를 증착하여 ONO 구조를 만들어 charge trap layer로서의 특성을 확인한 결과, SPNP로 증착한 막의 경우 3.4V, SNP로 증착한 막의 경우 2.8V의 C-V hysterisis를 얻을 수 있었다. 또한 SEM 분석 결과 SPNP로 증착한 막의 step coverage는 90%로 우수하였다.

다음으로 공간분할 방식 원자층증착법 (SALD)의 특성을 확인하고 이를 통하여 Al_2O_3 박막을 증착하였다. SALD 는 물리적인 partition wall로 공간적으로 구분된 가스 영역을 만들어 이러한 공간들을 이동하여 공간상에 체류되는 각기 다른 가스들을 순차적으로 노출시켜 ALD를 구현하는 방식이다. 이로 인하여 SALD는 기존의 ALD 대비 높은 증착 속도, 낮은 증기압을 갖는 물질의 이용 가능성 등의 효과를 기대할 수 있다.

이 연구에서는 SALD의 산업 적용성 및 SALD의 빠른 증착 속도를 이용한 Al_2O_3 박막 증착 을 연구하기 위하여 챔버 내부의 가스 유동에 관한 simulation과 tri-methyl-aluminum (TMA)와 오존을 이용하여 알루미늄 산화막을 증착하였으며,

증착된 박막의 전기적 특성을 평가하였다. Simulation과 증착 특성 평가 결과, 강한 edge pumping이 적용되었을 때 5mm의 간격을 갖는 조건에서도 가스들의 분리가 잘 일어나며 SALD가 성공적으로 진행되었음을 확인하였다. 미터링 밸브로 유입되는 TMA을 조절하여 0.5~2.0%의 범위에서 GPC가 약 0.13 nm/cycle로 saturation됨을 확인하였다. 또한 100°C~300°C의 증착 온도에서 특성을 확인할 수 있었으며, cycle 수가 증가함에도 GPC가 일정함을 확인할 수 있었다. 일반적인 ALD보다 빠른 공정 속도를 갖는 SALD로 증착된 Al_2O_3 박막들의 유전율은 8.04였으며, CET가 3.21nm인 박막의 leakage level은 -1V에서 9.8×10^{-8}A/cm^{2}임이 확인되었다.

주요어: 소스 플라즈마를 이용한 플라즈마 방식 원자층 증착법, Silicon nitride, 공간분할 방식 원자층 증착법, Al_2O_3 Si 전구체, TMA
학 번: 2008-22850
서 성 인